Vessel motion based assessment of pipeline integrity during installation

H.H. Knoppe

Delft University of Technology

TU Delft Delft University of Technology

Allseas

Challenge the future

VESSEL MOTION BASED ASSESSMENT OF PIPELINE INTEGRITY DURING INSTALLATION

By

H.H. Knoppe

in partial fulfilment of the requirements for the degree of

Master of Science
in
Offshore and Dredging Engineering

at the Delft University of Technology,
to be defended publicly on Thursday January 24th, 2019 at 14:30 PM.

Thesis committee:	Prof. dr. A.V. Metrikine	TU Delft
	Dr. ir. H. Hendrikse	TU Delft
	Dr. ir. K. N. van Dalen	TU Delft
	Dr. ir. F. Gerspach	Allseas Engineering

This thesis is confidential and cannot be made public.

Thesis author:

Hugo Hendrik Knoppe

In cooperation with:

Allseas Engineering B.V.
Poortweg 12
2612 PA Delft, the Netherlands
www.allseas.com

Delft University of Technology
Faculty of Mechanical, Maritime and Material Engineering
Mekelweg 2
2628 CM Delft, the Netherlands
www.3me.tudelft.nl

PREFACE

This research thesis is the end-product of my seven-year journey studying at the Delft University of Technology.

Starting out with a bachelor's degree in Mechanical Engineering, I was drawn to continue my academic path with the master program Offshore and Dredging Engineering. This master combined two of my passions: to broaden my understanding of the ocean and further my knowledge of technology.

The final steps of my academic road were taken as an intern at Allseas´ Pipeline Engineering Department located in Delft. I was fortunate enough to take these steps within a project which subject has always intrigued me; optimisation of existing technologies.
I would like to express my utmost gratitude to; Andrei Metrikine and Hayo Hendrikse for their supervision and efforts in supporting my thesis. From Allseas, I would like to thank François Gerspach, for his continued support, time, patience and guidance during this project. I would also like to thank Paula van Lieshout and Keran Rong, whom I am grateful to for letting me use parts of their projects within Allseas, which have supported my research.

These past months have been a challenge, but the experience and lessons learnt during the entire graduation research were certainly worth it. This could not have been achieved without the support and feedback from all involved, including my friends and family.

H.H. Knoppe
Delft, January 2019

ABSTRACT

If weather conditions become rough, vessel motions with an increased amplitude are excited due to the presence of waves. The sagbend region of a suspended pipeline catenary may experience high loads due to these motions. When the loads become too high, the pipeline integrity cannot be guaranteed. In such case, the pipeline is lowered to the seabed to prevent buckling and excessive damages to the pipeline. The pipelay operation is to be resumed later on when pipelay conditions have been improved. This process is called *Abandonment & Recovery* (A&R). It is essential to lay pipe as efficiently as possible to reduce the time spent offshore.

This study investigates the influence of the vessel motions with regard to pipeline integrity. This results in two objectives that are intertwined with one another. The first objective is to investigate the influence of vessel motions on the dynamic pipeline behaviour and integrity during installation operations. The second objective is to develop a method that will define a vessel motion based criteria for pipeline *Abandonment & Recovery* operations with respect to pipeline integrity.

Two methods are proposed to create ´statistical prediction´ curves to quickly assess the pipeline integrity. This requires the generation of multiple pipeline installation models during project preparation.

These methods are applied to various combinations of water depths and pipe properties. The dynamic behaviour of the pipeline is very sensitive to changes of these parameters. A shallow water and a deep water case are used for the analyses of the results and for the validation of the methods.

The pipeline integrity is assessed by predicting the maximum strain, the DNV buckling check and fatigue damage for a pipeline during installation based on stinger tip motions.

.

TABLE OF CONTENTS

1. INTRODUCTION

This chapter gives an introduction of Allseas Engineering and an introduction of the pipelay installation process. Subsequently, the problem background, the objective and the structure of the thesis are presented.

1.1. Allseas Engineering B.V.

Allseas Engineering B.V. is a part of Allseas Group S.A. which is one of the world leading contractors in offshore pipeline installation, heavy lift and subsea construction. Allseas was founded in January 1985 by Edward Heerema. Back then, Allseas had one vessel capable of laying pipe with a dynamic positioning system, which was revolutionary for its time. Since then, Allseas has grown significantly and at the moment, owns a fleet of seven vessels and a barge that execute a range of different activities.

From offshore pipelaying to installing and removing offshore structures, Allseas excels in the design and execution of large and complex offshore projects for major oil and gas producing companies worldwide. Activities include design, engineering, procurement, fabrication and project management. Their vessels are equipped with cutting-edge technologies and focus on offshore pipelines for oil and gas, as well as installation and removal of offshore platforms in a single lift.

1.2. Pipelay method

Multiple methods exist to install offshore pipelines. The most common methods are J-lay, S-lay and reel-lay. Reel-lay is mostly used for small diameter and flexible pipelines. The pipeline is spooled onto a large reel and installed offshore under tension. J-lay and S-lay are similar installation methods and require the pipeline to be assembled offshore. The clearest difference between these techniques is the orientation of the pipeline assembly and lay position. The installation of pipelines or ‘pipelay operations’ are conducted by Allseas with an S-lay technique.

This technique has the widest field of application in terms of pipe sizes and water depths. The pipeline is constructed at various workstations, which are horizontally along the length of the vessel. Sections of pipe are welded onto the end of the pipeline and moved over roller support to other workstations, which provide the newly welded pipeline section with a coating and a quality check. A stinger is located at the end of the firing line. Its function is to prevent the pipeline from buckling when it is bending from a near horizontal position on the vessel through the first bend of an S-curve towards the seabed. The stinger is a rigid structure, however it is able to rotate to facilitate the option of laying pipe at different depth, which require different departure angles of the pipeline. Once the pipeline leaves the stinger, it hangs in the free span between the vessel and the seabed.

The pipeline attains a certain 'S' shape between the pipeline touchdown point on the seabed to the vessel's firing line and therefore it is called the S-lay method.

The pipeline is held in place by tensioners. Tensioners are the central element of most pipelay systems. Their function is to hold the pipe in suspension between the end of the firing line and the seabed by applying a constant tension to the pipe. The tensioners start paying out and hauling in the pipeline to keep the tension at a certain value and to compensate for the effect of vessel motions.

The part of the pipeline that is bent over the stinger is called the overbend. This bending is governed by the orientation of the supports on the stinger. Since the deflection of the pipeline in this region is governed by the position of the supports, it is said to be a displacement controlled situation.

The part of the pipeline catenary that is suspended between the stinger tip and the seabed is called the sagbend region. Since this part of the pipeline hangs freely from the vessel its configuration is governed by the various static and dynamic loads acting on it. It is therefore said to be a load controlled situation.

1.3. Problem background

During pipeline installation, the vessel moves due to waves. These vessel motions influence the integrity of the suspended pipeline as the vessel motions influence the suspension and the dynamic behaviour of the pipeline that is being installed. Especially, shallow water cases have been known to be susceptible to the influence of vessel motions *(A.C. Palmer & R. A. King, 2009).*

If weather conditions become rough, vessel motions with an increased amplitude are excited due to the presence of waves. The sagbend region of a suspended pipeline catenary may experience high loads due to these motions. When the loads become too high, the pipeline integrity cannot be guaranteed. In such case, the pipeline is lowered to the seabed to prevent buckling and excessive damages to the pipeline. The pipelay operation is to be resumed later on when pipelay conditions have been improved. This process is called *Abandonment & Recovery* (A&R). It is essential to lay pipe as efficiently as possible to reduce the time spent offshore.

It is important to determine the integrity of the pipeline and in which way the pipeline reacts under expected loads. Computer simulations are used to predict the dynamic behaviour of the pipeline. These computer simulations are very time consuming and therefore cannot be used for real-time decision making. Before the start of pipeline installations the point of abandonment has been determined by performing simulations in which numerous possible weather conditions have been simulated.

When pipelay operations are operationally limited by pipeline integrity the operational limit is typically defined by a limiting sea state. Such a limiting sea state is characterized by a significant wave height (H_s), a zero up-crossing wave period (T_z) and the propagation direction of the waves relative to the vessel (θ). In practice these idealised conditions do not exist offshore which might result in unnecessarily conservative abandonment decisions and therefore loss of time and money for the company.

Expected weather and vessel motions predictions are only known a few hours beforehand. This is due to the unpredictability of the weather and waves in general. Therefore a faster method of determining pipeline integrity is desired. This results in the fact that actual weather and wave data can be used and the prediction of pipeline integrity will be less conservative.

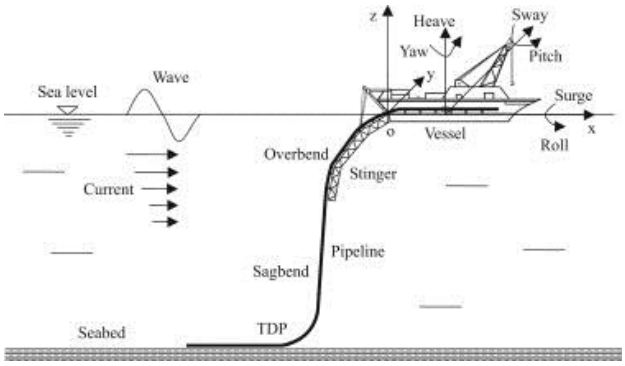

Figure 1-1 Pipelay installation

1.4. Objectives

This thesis consists of two main objectives.

The first objective is to investigate the influence of vessel motions on the dynamic pipeline behaviour and integrity during installation operations.

The second objective is to develop a method that will define a vessel motion based criteria for pipeline *Abandonment & Recovery* operations with respect to pipeline integrity. The aim of developing these criteria is to accurately determine the limiting motion. With the use of these predictions the pipeline integrity can be quickly assessed for the given environment.

1.5. Structure of the document

The thesis is divided into six chapters. The first chapter gives an introduction of the thesis. The second chapter contains the majority of the theoretical information that is used throughout the thesis. In the third chapter the method that is used for completing the objective of the thesis is described. The results and analyses that follow from implementing the described method are presented in the fourth chapter. The fifth chapter consists of a validation and discussion and the sixth and last chapter contains the conclusion and recommendations of the thesis.

2. DYNAMIC PIPELINE BEHAVIOUR

This chapter describes the pipeline installation process along with its most important parameters. Furthermore, the theory of ocean waves and vessel motions is described along with the manner in which pipeline integrity will be assessed during this thesis. The modelling of the pipeline, tensioners and the pipelay vessel is discussed. Finally this chapter includes the method and results of the dynamic isolated motion analysis, which will determine relevant vessel motions with regard to pipeline integrity.

2.1. S-lay configuration

There are a number of factors that determine the configuration and dynamic behaviour of the suspended pipeline during an S-lay installation process. The S-lay configuration including pipelay terms are shown in Figure 2-1.

Tension

The shape of the pipeline in the sagbend is primarily controlled by the interaction between the applied tension and the submerged weight of the pipeline, and to a lesser extent by the stiffness of the pipeline. If the applied tension is increased, the radius of the pipeline is in the sagbend increases and the sagbend becomes longer and flatter. If the applied tension is reduced, the sagbend radius decreases. If the tension is reduced too much, the pipeline may buckle in both the sagbend and the lift-off point of the vessel.

Pipe departure angle

The pipe departure angle or lift-off angle is the angle relative between the pipeline and the horizontal plane at the point where the pipeline is no longer in contact with the rollers on the stinger. The departure angle is governed by the top tension. The tip separation between the stinger tip and the suspended pipeline should be at least 0.3 meters to prevent the pipe from clashing against the stinger tip.

Pipe properties

The dimensions and material properties of the pipeline are chosen to meet the operational requirements of the pipeline. These factors, such as the diameter and the wall thickness of the pipe, determine the submerged weight. The weight of the suspended pipeline determines the top tension and therefore the dynamic pipeline behaviour.

Water depth

The water depth is one of the most important factors that determines the pipeline configuration. The water depth determines the length of the suspended pipeline and the required pipe properties. Therefore, the required top tension and dynamic behaviour is also influenced by the water depth.

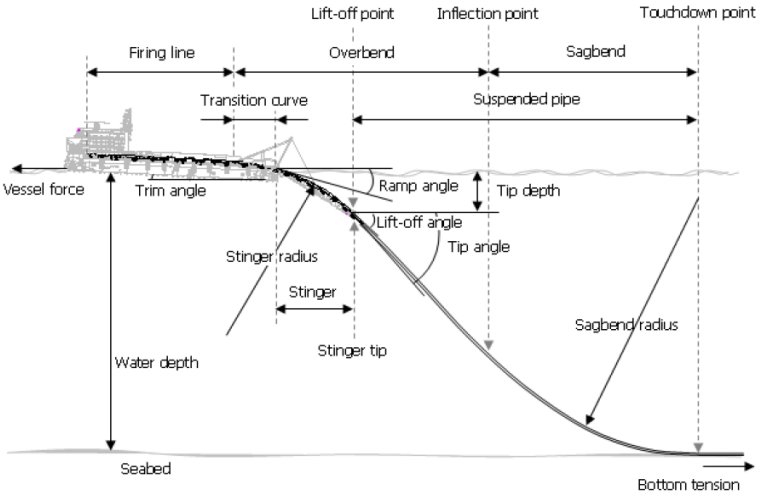

Figure 2-1 Schematic side view of S-lay including pipelay terms (Allseas Introduction File, rev. 4)

2.2. Ocean waves

Waves in oceanic waters are created by the wind that is constantly blowing over the water surface and thereby transferring energy from the wind to the water. This transfer of energy manifests itself in the form of water surfaces moving up and down at a location, otherwise better known as waves. Ocean waves are stochastic and irregular by nature. Despite this complex nature of the waves, these irregular waves can be decomposed into a large number of harmonic wave components, depicted in Figure 2-2 (Leo H. Holthuijsen, 2007).

These regular waves travel across the ocean surface with different periods, directions, amplitudes and phases. The harmonic wave components are often a combination of waves that are very different in origin and behaviour. Swell-waves are for instance long, smooth waves that are generated in a distant storm and wind sea waves are short, irregular, locally generated waves.

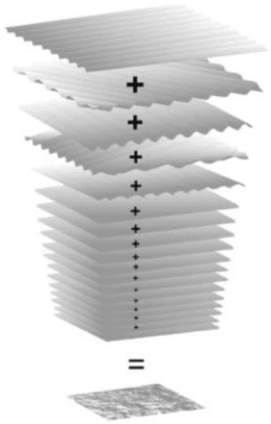

Figure 2-2 Decomposition of irregular waves (Pierson, Neumann & James, 1955)

The decomposition of irregular waves can also be represented as an energy density spectrum. This spectrum shows how the wave energy is distributed over the range of wave frequencies. The overall appearance of the waves can be inferred from the shape of the spectrum: the narrower the

spectrum is, the more regular the waves are. There are various wave spectra developed over the years to represent certain sea state conditions. The most important spectrum, as Holthuijsen describes in *"Waves in Oceanic and Coastal Waters" (2007),* is the Joint North Sea Wave Project. This spectrum is better known as the JONSWAP spectrum. The general outline of a uni-directional JONSWAP spectrum is shown in Figure 2-3.

The JONSWAP spectrum was developed for the limited fetch North-Sea. Other sea spectra include the Torsethaugen spectrum, the Bretschneider spectrum, etc., that represent North-Sea conditions with a double peak (swell & land generated wave) and deep water North Atlantic conditions without swell.

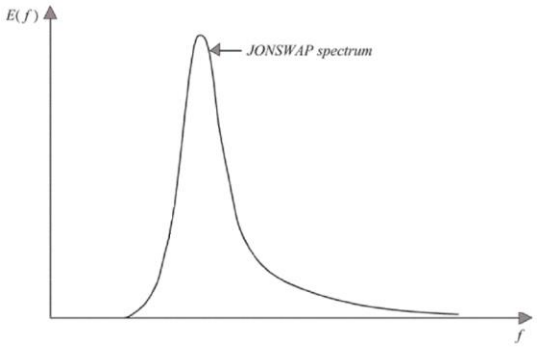

Figure 2-3 JONSWAP spectrum (Holthuijsen , 2007)

Wave characteristics

The simplest wave to describe is a regular, periodic wave and is characterized by its wave height, H, and wave period, T_z. Both are illustrated in Figure 2-4 and 2-5, along with wave length λ.

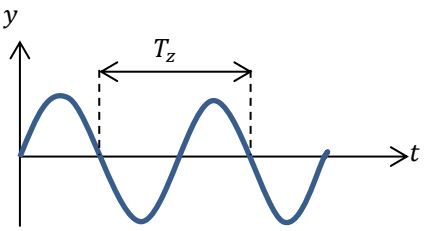

Figure 2-4 Wave profile – Time domain

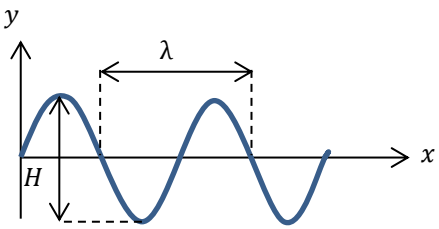

Figure 2-5 Wave profile – Space domain

2.3. Vessel motions

Vessel motions are the response motions of vessels due to the presence of waves. These vessel motions are generally defined in six degrees of freedom as can be observed in Figure 2-6.

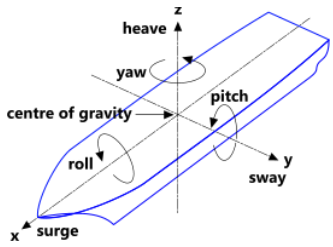

Figure 2-6 Six degrees of Freedom (DoF) of vessel motions

The six vessel motions in the steadily translating system are defined by:

- 3 translations of the ship's centre of gravity (CoG) in the direction of the *x*-, *y*- and *z*- axes.
  - surge in the longitudinal *x*-direction, positive forwards,
  - sway in the lateral *y*-direction, positive to port side, and
  - heave in the vertical *z*-direction, positive upwards,

- 3 rotations about these axes:
  - roll about the *x*-axis, positive right turning
  - pitch about the *y*-axis, positive right turning, and
  - yaw about the *z*-axis, positive right turning

All vessel motions are built up from these basic motions. These vessel motions are largely excited by waves transferring energy in the form of kinetic energy. The motions response due to this transfer of energy is defined by displacement response amplitude operators (RAOs).

The principle of the transformation of wave energy to response energy is shown in Figure 2-7. The irregular wave history, below on the left side of the figure, is the sum of a large number of wave components. The wave spectrum is discretized into individual components with a certain amplitude, frequency and a random phase shift, these are represented as orange boxes in Figure 2-7. Each regular wave component can be transferred to a regular vessel motion component by a multiplication of the RAO. The result is given in the right hand side of this figure (J.M.J. Journee & W.W. Massie, 2008).

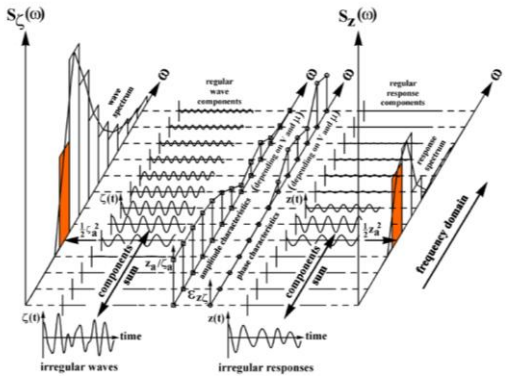

Figure 2-7 Converting wave spectra into vessel motions (J.M.J. Journee & W.W. Massie, 2008)

2.4. Pipeline Integrity

The integrity of the pipeline during installation is assessed. The integrity of the pipeline is crucial at the sagbend area of the pipeline as the loads acting on that area of the pipeline are partially uncontrolled.

To ensure the integrity of the pipeline, the buckling limit and the fatigue installation damage is determined.

The buckling check is governed by the loads acting on the pipeline and therefore governed by the axial tension acting on the pipeline. The fatigue damage is determined, as is common practice at Allseas, using the strain acting on the pipeline. The equivalent tensile strain on the pipeline, further referenced as the Von Mises strain, is assessed, as both the buckling check and the fatigue damage are related to the strain occurring in the pipeline.

2.4.1. Von Mises strain

The von Mises Strain is a simplified equivalent strain, commonly used in pipelay analysis. The Von Mises Strain is given by the following formula:

$$\epsilon_{VM} = \sqrt{\epsilon_{zz}{}^2 + \epsilon_{cc}{}^2 - \epsilon_{zz} * \epsilon_{cc}} \tag{2.1}$$

Where:

ϵ_{zz} is the axial strain due to direct tensile strain and bending strain
ϵ_{cc} is the Hoop strain, see Equation 2.2

$$\epsilon_{cc} = \frac{\sigma_{cc}}{E} \tag{2.2}$$

Where:

σ_{cc} is the Hoop stress
E is the Young's modulus, or stiffness property of a specific material

2.4.2. DNV buckling check

To ensure the integrity of the pipeline, the buckling limit state is determined with the DNV-OS-F101 code check (DNV, 2013). This standard provides an internationally acceptable standard of safety for submarine pipeline systems by defining minimum requirements for concept development, design, construction, operation and abandonment. Note that the passages with the heading: "*Load controlled condition*", "*Pressure calculation*" and "*Design load combination*" have been directly replicated from DNV-OS-F101 (2013).

Within the pipelay industry it is generally accepted that the sagbend region of a pipeline is load controlled and therefore the formula of the load controlled buckling check is chosen.

In rare cases, for instance when a very stiff pipe is being laid in very shallow water, the situation can be considered as displacement controlled. However, since load controlled is always more conservative than displacement controlled, a load controlled analysis will still be required. In the

rare case meant above, this might be over-conservative. It is less relevant for this study to spend a lot of effort to determine to what extent the situation has to be considered displacement controlled.

Load controlled condition

Pipe members subjected to bending moment, effective axial force and external overpressure shall be designed to satisfy the following criterion at all cross sections:

$$\left\{\gamma_m * \gamma_{SC} * \frac{|M_{Sd}|}{\alpha_c * M_p(t)} + \left\{\frac{\gamma_m * \gamma_{SC} * S_{Sd}(p_i)}{\alpha_c * S_p(t)}\right\}^2\right\}^2 + \left(\gamma_m * \gamma_{SC} * \frac{p_e - p_{min}}{\alpha_c * p_c(t)}\right)^2 \leq 1 \quad (2.3)$$

Applies for

$$15 \leq D/t \leq 45, \qquad P_i > P_e, \qquad S_{Sd}/S_p < 0.4$$

Where:

γ_m	is the material resistance factor
γ_{SC}	is the safety class resistance factor
M_{Sd}	is the design moment, see Equation 2.15
S_{Sd}	is the design effective axial force, see Equation 2.16
p_e	is the external pressure
p_{min}	is the minimum internal pressure that can be sustained. This is normally taken as zero for installation except for cases where the pipeline is installed water filled.
p_c	is characteristic collapse pressure, see Equation 2.11
S_p *and* M_p	denote the plastic capacities for a pipe defined by:

$$S_p(t) = f_y * \pi * (D - t) * t \quad (2.4)$$

$$M_p(t) = f_y * \pi * (D - t)^2 * t \quad (2.5)$$

$$\alpha_c = (1 - \beta) + \beta * \frac{f_u}{f_y} \quad (2.6)$$

$$\beta = \frac{60 - {}^{D}/_{t^2}}{90} \quad (2.7)$$

$$f_y = (SMYS - f_{y,temp}) * \alpha_U \quad (2.8)$$

$$f_u = (SMTS - f_{u,temp}) * \alpha_U \quad (2.9)$$

Where:

SMYS	Specified Minimum Yield Stress
SMTS	Specified Minimum Tensile Stress
$f_{y,temp}$	Derating of yield stress based on temperature
$f_{u,temp}$	Derating on tensile stress based on temperature
α_U	Material strength factor
D	Pipeline nominal outside diameter
t	Pipeline wall thickness

Pressure calculation

The characteristic resistance for external pressure (p_c) (collapse) shall be calculated as:

$$\left(p_c(t) - p_{el}(t)\right) * \left(p_c(t)^2 - p_p(t)^2\right) = p_c(t) * p_{el}(t) * p_p(t) * f_0 * \frac{D}{t} \quad (2.11)$$

Where:

$$p_{el}(t) = \frac{2*E*\left(\frac{t}{D}\right)^3}{1-\nu^2} \quad (2.12)$$

$$p_p(t) = f_y * \alpha_{fab} \frac{2*t}{D} \quad (2.13)$$

$$f_0 = \frac{D_{max}-D_{min}}{D} \quad (2.14)$$

α_{fab}	Fabrication factor
E	Young's modulus
v	Poisson's ratio

Design load combination

The design load effect can generally be expressed in the following formulas:

$$M_{Sd} = M_F * \gamma_F * \gamma_c + M_E * \gamma_E + M_I * \gamma_F * \gamma_c + M_A * \gamma_A * \gamma_c \quad (2.15)$$

$$S_{Sd} = S_F * \gamma_F * \gamma_c + S_E * \gamma_E + S_I * \gamma_F * \gamma_c + S_A * \gamma_A * \gamma_c \quad (2.16)$$

Limit state/load combination	Load effect combination		Functional loads[1]	Environmental loads	Interference loads	Accidental loads	Condition load effect
			γ_F	γ_E	γ_F	γ_A	γ_C
ULS	a	System check[2]	1.2	0.7			0.8
	b	Local check	1.1	1.3	1.1		
1) If the functional load effect reduces the combined load effects, γ_F shall be taken as 1/1.1.							
2) This load effect factor combination shall only be checked when system effects are present, i.e. when the major part of the pipeline is exposed to the same functional load. This will typically only apply to pipeline installation.							

Table 2-1 DNV ultimate limit state load combinations

The partial safety factors in DNV-OS-F101 have been determined by structural reliability methods to a pre-defined failure probability. Structural reliability calculations differentiate between single joint failures (local checks) and series system failures (system effects)
These two kinds of scenarios are expressed as two different load effect combinations in DNV-OS-F101 as is illustrated in Table 2-1:

a) shall only be considered for scenarios where system effects are present.
b) for local scenarios and shall always be considered.

When system effects are present, the pipeline will fail at its weakest point. Hence, the likely load shall be combined with the extreme low resistance.
Applied to pipelines, system effects are present for:

- pressure containment
- collapse, in as installed configuration
- installation

Regarding installation, an extreme environmental load is not likely to occur when the weakest pipe section is at the most exposed location, indicating that system effects are not present. However, combined with a more representative environmental load (in extreme cases, "flat sea"), the whole pipeline will undergo the same deformation over time, hence, having a system effect present.

In summation, load combination b) shall always be checked while load combination a) normally is checked for installation only.

2.4.3. Fatigue

Fatigue failures in metallic structures such as pipelines are a well-known technical problem. According to Schijve (2009), fatigue damage is defined as follows:

> *"A single load, far below the static strength of a structure, will not do any damage to the structure. But if the same load is repeated many times it could induce a complete failure. This type of structural damage is referred to as 'fatigue'."*

In the pipe laying process fatigue limits the time that the installation process can be halted. When the installation process is at a standstill, the stresses at the stinger tip tend to show great variations due to wave induced vessel motions. Repeated stress on the pipe create fatigue damage to the material, thus making the pipe weaker and easier to buckle.

Fatigue properties are generally supposed to be material properties. In order to determine the amount of fatigue damage to a certain material S-N curves can be used. In an S-N curve the allowable number of cycles (N) is plotted against the cyclic stress range (S). This information is derived from fatigue tests on a large number of material specimens, carried out until failure occurred. An S-N curve is obtained as a result of multiple fatigue tests at different stress levels. An example of an S-N curve is shown in Figure 2-8. It has to be noted that the horizontal axis on which the number of cycles is shown has a logarithmic scale. The mean S-N curve represents a fifty percent probability of survival. The S-N curves typically used for designing are the curves of two standard deviations below the mean curve, with a probability of survival of 97.7 percent.

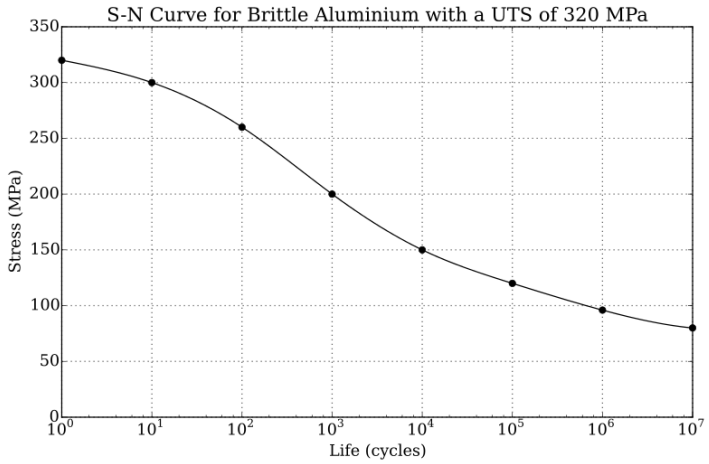

Figure 2-8 S-N curve example of brittle aluminium

In the majority of fatigue problems the applied load cycle will not be constant. In that case, the different load amplitudes will have to be converted in order to assess the fatigue. This conversion is done using the Palmgren-Miner sum calculation method.

Von Mises stress

The Von Mises stress range is used for the fatigue calculations. This is linearly derived from the occurring Von Mises strain, which is common practice within Allseas. When the pipeline does not deform plastically the relationship is linear between stress and strain. In this case Hooke's law is applicable. It is assumed that the relationship between stress and strain is linear in the sagbend region of the suspended pipeline. Hooke's law is a law of physics that states that the force acting on a linear-elastic material is dependent on the stiffness and the distance of elongation:

$$F = kx, \tag{2.17}$$

$$in\ which\ F = force\ [N], \qquad k = stiffness\ \left[\frac{N}{m}\right], \qquad x = distance\ of\ elongation\ [m]$$

The way in which the Von Mises stress is derived is illustrated in Figure 2-9.

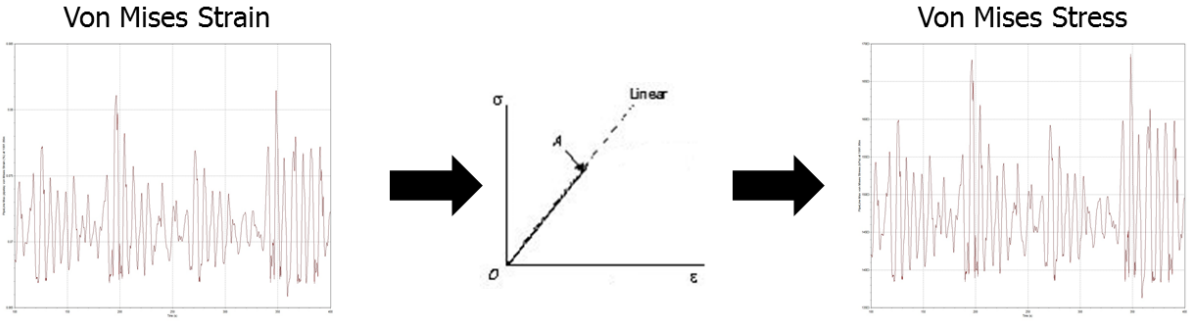

Figure 2-9 Von Mises stress derived from linear relationship between strain and stress

Palmgren-Miner Rule

The Palmgren-Miner formula (2.18) states that the total accumulated fatigue damage for a number of load cycles with various load ranges can be calculated by summation of the fatigue damage calculated for each individual cycle. The fatigue life is calculated based on the S-N fatigue approach under the assumption of linear cumulative damage.

$$D = \sum_{i=1}^{k} \frac{n_i}{N_i} = \frac{1}{\bar{a}} \sum_{i=1}^{k} n_i * (\Delta\sigma_i)^m \leq \eta \tag{2.18}$$

Where:

D	is the accumulated fatigue damage
ā	is the intercept of the design S-N curve with the log(N) axis, see Table 2-2
m	is the negative inverse slope of the S-N curve, see Table 2-2
k	is the number of stress blocks
n_i	is the number of stress cycles in block i
N_i	is the number of cycles to failure at constant stress range $\Delta\sigma_i$
η	is the usage factor, 1/(design fatigue factor) from DNVGL-OS-C101

When applying a histogram to express the stress distribution, the number of stress blocks should be large enough to ensure reasonable numerical accuracy. This number should be no less than twenty as stated by DNVGL-RP-C203.

Within the pipeline industry, it is generally accepted that such calculation should be carried out using the S-N curve properties of the class F weld, as are stated in DNVGL-RP-C203 and Table 2-2.

S-N curve	$N \leq 10^7$ cycles		$N > 10^7$ cycles	Fatigue limit at 10^7 cycles (MPa) *)	Thickness exponent k
	m_1	$\log \bar{a}_1$	$\log \bar{a}_2$ $m_2 = 5.0$		
B1	4.0	15.117	17.146	106.97	0
B2	4.0	14.885	16.856	93.59	0
C	3.0	12.592	16.320	73.10	0.05
C1	3.0	12.449	16.081	65.50	0.10
C2	3.0	12.301	15.835	58.48	0.15
D	3.0	12.164	15.606	52.63	0.20
E	3.0	12.010	15.350	46.78	0.20
F	3.0	11.855	15.091	41.52	0.25
F1	3.0	11.699	14.832	36.84	0.25
F3	3.0	11.546	14.576	32.75	0.25
G	3.0	11.398	14.330	29.24	0.25
W1	3.0	11.261	14.101	26.32	0.25
W2	3.0	11.107	13.845	23.39	0.25
W3	3.0	10.970	13.617	21.05	0.25

Table 2-2 S-N curve properties as presented in DNVGL-RP-C203

Rainflow counting

Stress range counting includes the counting of all successive stress ranges. This includes small load variations occurring between adjacent larger ranges. The rainflow counting algorithm is used in the analysis of these stress ranges. This method counts the number of successive load ranges. As fatigue is dependent on stress ranges; a larger stress range per cycle will result in a higher fatigue damage. This has led to the so-called rainflow counting method, which is illustrated in Figure 2-10. The intermediate small load reversal is counted as a separate cycle and then removed from the major load range. This larger range is counted as a separate load range.

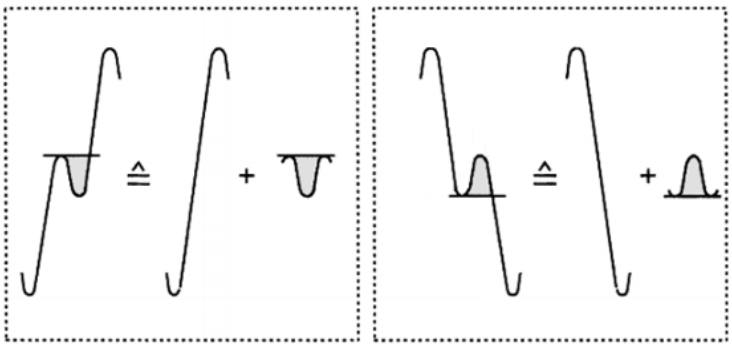

Figure 2-10 Rainflow counting method (Schijve, 2009)

Accumulated fatigue damage of pipe joints

As the pipeline is paid out during each pull, a pipe joint is subjected to different loads every duration of a pull. Pipeline welds are accumulating fatigue damage from the moment they pass the tensioners until they reach the seabed. The total accumulated fatigue damage experienced by a pipeline joint in the installation phase is calculated as the sum of the accumulated damage at each position step, starting from the tensioners to the seabed. This will be used to analyse and predict the fatigue damage. An example of the fatigue damage rate over the pipeline catenary is shown in Figure 2-11. This example shows the damage rate of a 280m water depth case. This figure clearly displays that the highest damage rate is located at the lift-off point of the stinger. This is due to the fact that the Von Mises stress range, occurring at the lift-off point, is the largest in the entire pipeline catenary. This is because the lift-off point is the location where the pipe leaves the support of the rigid stinger, which forces the suspended pipeline to move.

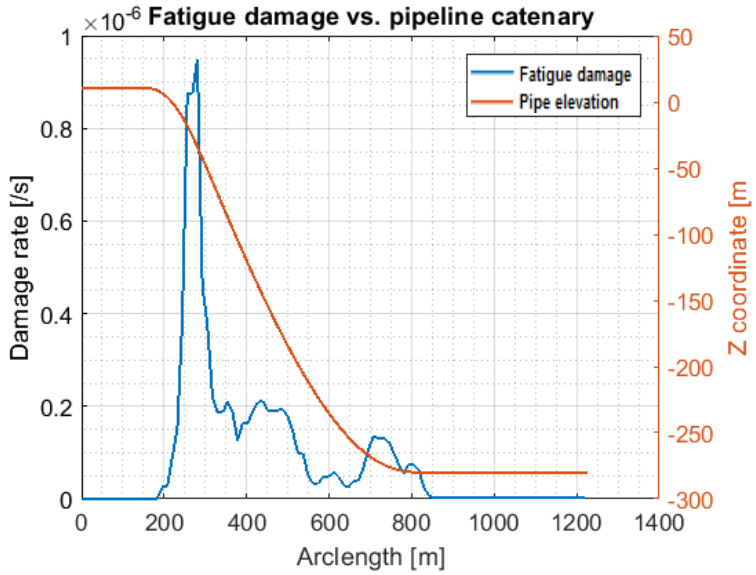

Figure 2-11 Example of fatigue damage in pipeline (Hs=3.5m, Tz=7s, θ=70deg)

2.5. Orcaflex

Simulations to analyse the vessel motions and the influence the vessel motions have on the pipeline integrity are conducted in a software package called Orcaflex. Orcaflex is designed to analyse the dynamic behaviour of offshore marine systems.

2.5.1. Pipeline model

The pipeline is represented within Orcaflex as a series of flexible massless linear springs with nodes at the end of these elements as is shown in Figure 2-12a. Each node consists of two very short rods that represent two half segments on either side of the node. Each segment represents axial and torsional properties of the line. Other pipe properties such as mass, weight, buoyancy, etc. are all concentrated on the nodes.
Figure 2-12b shows the structural model of a single node and its adjoining line segments. The structural properties are modelled with various springs and dampers.

- The axial stiffness and the damping of the pipeline are modelled by an axial spring and a damper located at the centre of a line segment.
- The torsional properties of the pipeline are represented by rotational springs and dampers located at the centre of a line segment.
- The bending properties are modelled with rotational springs and dampers located on either side of the nodes.

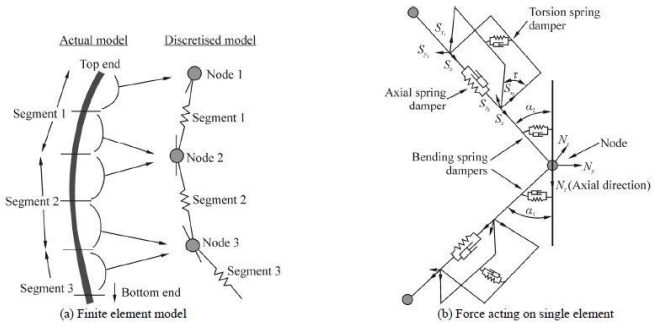

Figure 2-12 a-b Pipeline model Orcaflex

2.5.2. Vessel model

A pipelay vessel is comprised of several types of equipment, such as a stinger, roller boxes and tensioners which are influential to the suspended pipeline dynamics. The model of the vessel is based on the vessel dimension data of the Solitaire vessel, which is one of the largest pipelay vessels in the world. The Solitaire pipelay vessel measures 397 meters in length and 41 meters in width. The stinger is rigidly fixed onto the vessel and is therefore considered to be a part of the vessel, although the orientation of the stinger may change for different installation projects.

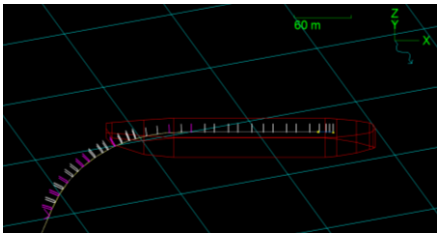

Figure 2-13 Solitaire vessel modelled in Orcaflex

2.5.3.Tensioner models

The tensioner is a crucial part of the modelling process of pipelay as it governs the tension acting on the pipeline catenary and therefore influences the dynamic motion behaviour of the pipeline catenary. The tensioners on the Solitaire vessel make use of a user-programmable control system

Orcaflex modelling

To simulate the behaviour of the tensioners, one end of the pipeline, which is located on the vessel is connected to a winch element, illustrated in Figure 2-14. Winches provide a way of modelling the tension compensating mechanism by hauling in or paying out pipeline. A winch element is a wire element with certain stiffness and damping properties. These winches connect two or more points in the model by a winch wire, fed from a winch inertia (typically representing a winch drum) which is driven by a winch drive (typically representing the hydraulics that drive the drum).

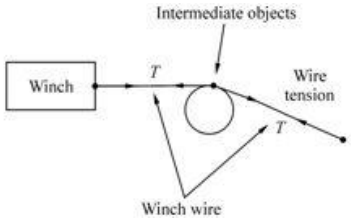

Figure 2-14 Tensioner winch model

Deadband model

Allseas models the tensioners with a so called dead-band model. This is a fully compensating model with a dead-band which corresponds to 20% of the set tension, to account for all inertial effects and delays in the real-time compensating effect of the tensioner. A dead-band of 20% allows the tension to shift within the specified limits. Any tension that exceeds this limits are fully compensated by paying out and hauling in of the pipeline. The percentage is based on historical data. The value is derived from tension shifts that have occurred with previous projects.

PI Controller model

One of the objectives of a previous graduation thesis, conducted by T.A. Simanjuntak, was to model a tensioner more realistically than the dead-band model, which is currently being used by Allseas. Within this thesis, a PI-controller is introduced to mimic the response the tensioners. The comparison of behaviour of this tensioner model is presented in Figure 2-15 and Table 2-3 for seven cases considered within the aforementioned thesis. An illustration of the pipeline catenary of these cases is shown in Figure 2-16. For more information on the different tensioner models or installation cases used, during the aforementioned thesis, please refer to the graduation thesis of T.A. Simanjuntak (2017).

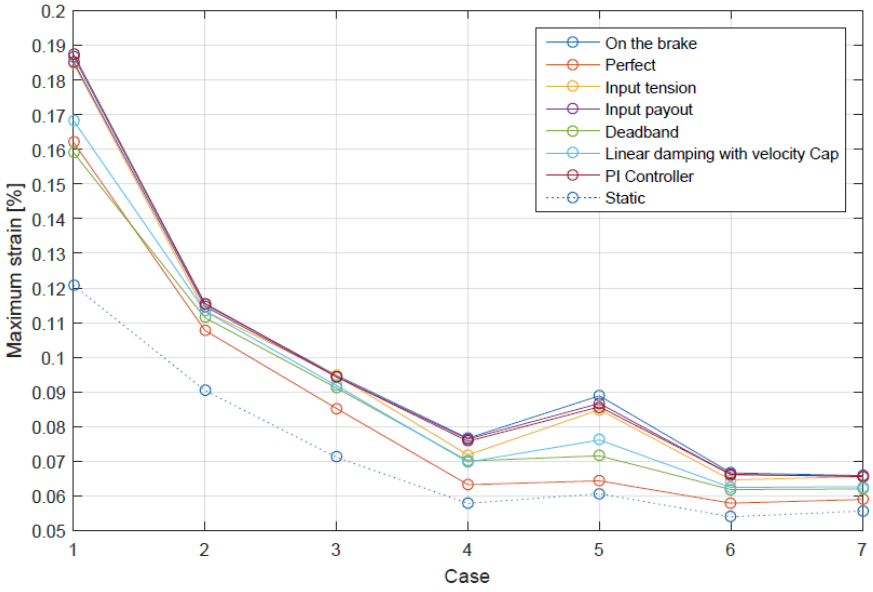

Figure 2-15 Maximum strain comparison for different tensioner models (T.A. Simanjuntak, 2017)

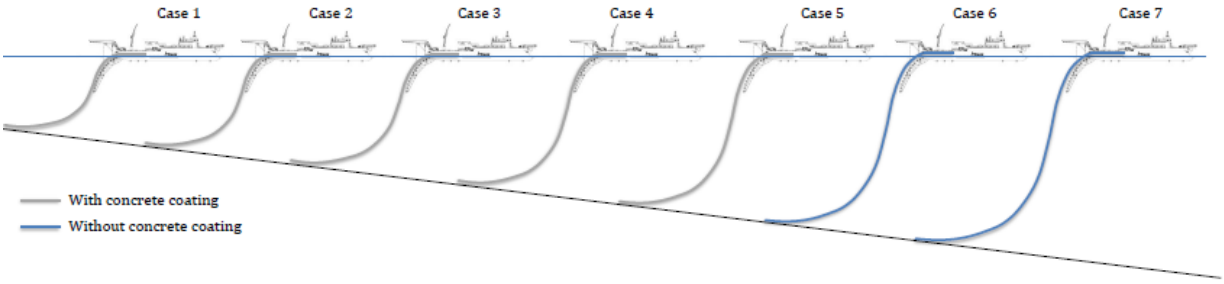

Figure 2-16 Overview of different cases (T.A. Simanjuntak, 2017)

Case number	Maximum von Mises strain for each tensioner mode [%]						
	On the brake	Perfect	Input tension	Input payout	Deadband	Linear damping with velocity cap	PI Controller
1	0.187	0.162	0.185	0.185	0.159	0.168	0.188
2	0.115	0.108	0.113	0.115	0.111	0.113	0.116
3	0.095	0.085	0.095	0.094	0.091	0.092	0.094
4	0.077	0.063	0.072	0.076	0.070	0.070	0.076
5	0.089	0.064	0.085	0.087	0.072	0.076	0.086
6	0.067	0.058	0.065	0.066	0.062	0.062	0.066
7	0.066	0.059	0.066	0.066	0.062	0.063	0.066

Table 2-3 Strain comparison for different tensioner models (T.A. Simanjuntak, 2017)

‘On brake’ model

The behaviour of the aforementioned PI-controller is shown in red in Figure 2-15. The response of the tensioner model is very comparable to a tensioner model that does not haul in of pay out pipe. In other words, a ‘tensioner on the brake’ illustrated with a blue colour in Figure 2-15.

When a tensioner does not haul in or pay out pipeline, the compensating effect of the tensioner is cancelled. Due to the loss of tension compensation, the pipeline behaviour will be less realistic. In return, the influence of vessel motion on the tension of the pipeline and dynamic behaviour of the pipeline becomes more apparent.

Due to the comparable behaviour of the designed PI-controller tensioner model and a tensioner on the brake the tensioner is modelled as a tensioner ‘on the brakes’. Another reason for modelling the tensioner on the brakes is the fact that the main interest of this thesis consist of investigating the dynamic behaviour of the pipeline due to vessel motions. By modelling the tensioner on the brakes there is no motion compensating effect created by the tensioner.

To determine how this ‘on brake’ model relates to a real life tensioner, one should observe the “input pay-out” and the “input tension” line of Figure 2-15. These lines represent the simulated strain when the real life measured tension or measured pay-out of the pipeline is used as an input of the Orcaflex tensioner. Since these lines represent the strain simulated with real life tension and pay-out of the pipeline, the dynamic pipeline behaviour in these models should be the same as in reality. These lines (yellow and purple) are consistently close to the maximum strain values with a tensioner model on the brakes. It is therefore safe to assume that this Orcaflex and tensioner model is representative of the ‘real life’ dynamic pipeline behaviour.

2.6. Isolated vessel motion analysis

One of the objectives of this thesis is to investigate the influence of the pipeline integrity due to vessel motions. Therefore, an analysis is conducted that determines which vessel motions are relevant as input parameters for a statistical strain prediction model and a statistical fatigue prediction model. As a result, the dynamic behaviour of the pipeline due to isolated vessel motions is analysed.

2.6.1. Method

Using the simulation software Orcaflex, the influence of vessel motions on the maximum strain and fatigue damage in the sagbend region is analysed. Isolated vessel motions are analysed with certain user-specified displacement amplitudes and periods. The amplitude and the period of these motions are altered for the analysis of the vessel motions on the strain.

2.6.2. Vessel motion amplitude

The amplitudes that are chosen for the vessel motions are based on the measured vessel motions during the Rota 3 project. The selection of these recorded motions is presented in Appendix A. For every vessel motion, the maximum displacement amplitude is determined. The values of the maximum displacement amplitudes for the 6DoF are shown in Table 2-4.

Amplitudes	Maximum displacement amplitude
Surge	0.595 m
Sway	1.125 m
Heave	2.160 m
Roll	1.23 deg
Pitch	1.60 deg
Yaw	0.35 deg

Table 2-4 Measured vessel motion ranges during ROTA3 project

2.6.3. Vessel motion frequency

To determine which vessel motion frequency or period is relevant for both analyses, the amplitude spectrum of the measured translational and rotational motions is shown in Figure 2-17.

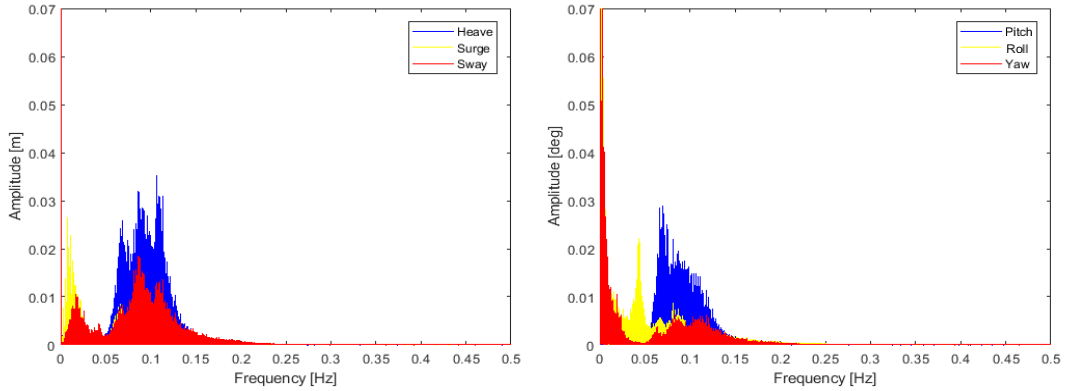

Figure 2-17 Amplitude spectrum of measured translational and rotational motions

The wave induced vessel motions can be split into two groups:

- Vessel motions excited by first order waves
- Vessel motions excited by second order waves

The 'first order vessel motions' are located around 0.1 Hz. The vessel motions that result from second order vessel motions are located at a lower frequency. This frequency is approximately 0.05 Hz for the roll motion and even lower for other motions. At an approximate frequency of 0.17Hz the amplitudes become relatively small. It is unlikely that amplitudes exceeding this frequency are related to wave-induced motions because the Solitaire is a large vessel with a rigid hull and with a large inertia. These amplitudes are likely created by noise in the MRU data or other factors, such as vibrations caused by work on deck or by the engine of the vessel.
The vessel motion amplitudes that are the most relevant for analysis lie within the frequency range of 0.05-0.17 Hz. This means vessel motions with a T_z range of six up to twenty seconds are relevant for analysis.

2.6.4. Simulations

Simulations of 400s are conducted in Orcaflex to acquire the strain and fatigue damage for every vessel motion with a T_z ranging from four up to twenty seconds with a step size of 0.2 seconds. The simulation time of 400 seconds is chosen because most strain signals resulting from this method have a settling down time of 100-150 seconds. This leaves approximately 250-300 seconds of usable simulation time. The resulting strain is chosen as the maximum strain that occurs during the last five periods of the simulated strain signal. For example, if the vessel motion period is twenty seconds, then the last 100 seconds of the simulation will be analysed.

As stated before in Section 2.5.3, the simulations will be conducted with the tensioners on brakes.

It may occur that the settling time spans a large period of time and an overshoot of the output signal is registered as the maximum, which will be an overestimation. This is prevented by analysing consecutive data points of the resulting graphs. If consecutive data points have large differences and therefore sudden peaks, simulations are repeated for 600 seconds instead of 400 seconds.

To conduct the dynamic isolated vessel motion analysis, approximately 1300 simulations are conducted in Orcaflex for every case. This number results from every combination of amplitude and period for the six DoF of vessel motions.

2.6.5. Maximum strain results

The dynamic behaviour of the strain acting on the pipeline due to isolated vessel motions is analysed for a shallow water case of 150m water depth and a deep water case of 1496m water depth and the results are shown in Figure 2-18(a-f) and Figure 2-19(a-f).

Shallow water

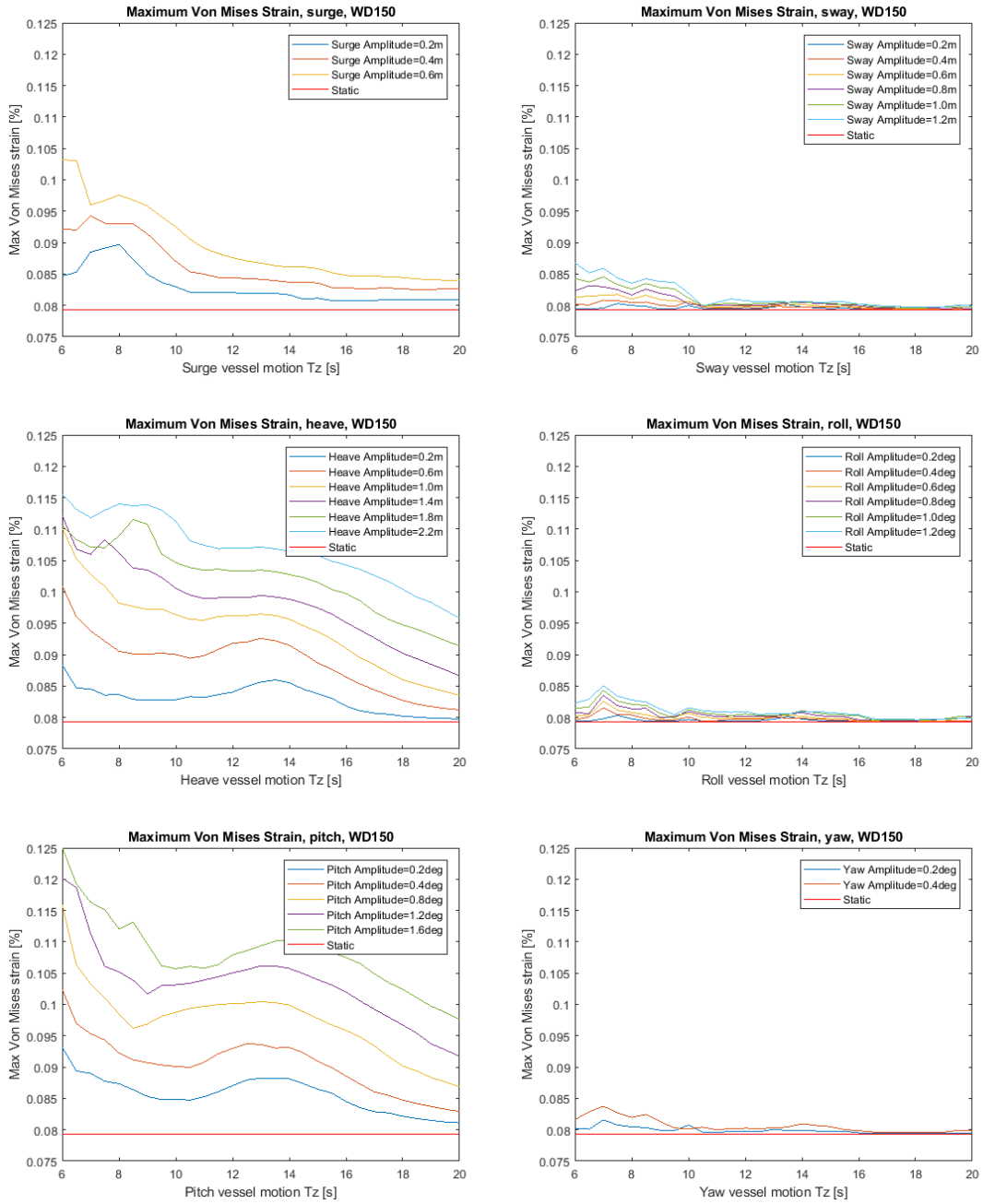

Figure 2-18 a–f Shallow water isolated vessel motion strain analyses

Deep water

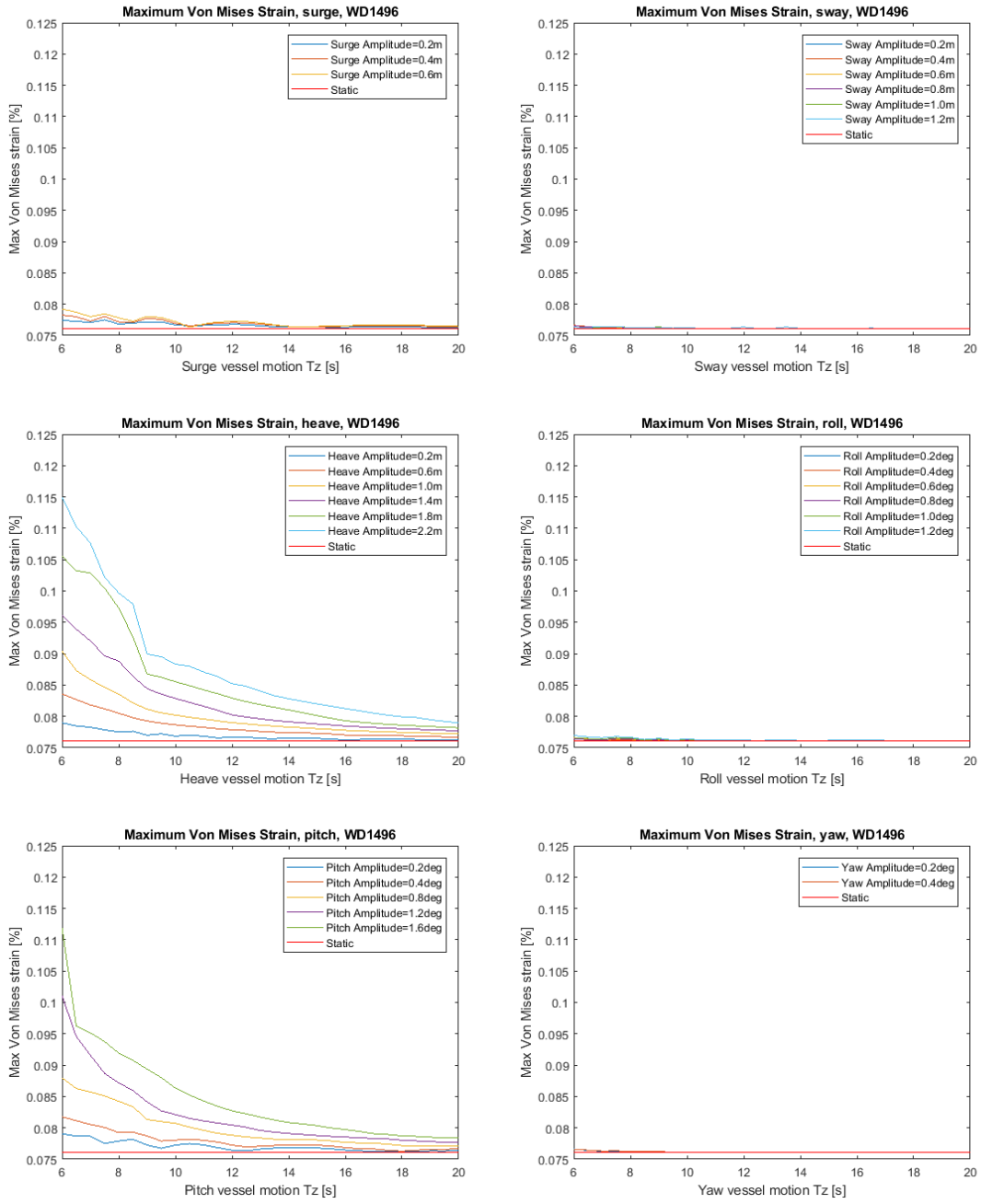

Figure 2-19 a–f Deep water isolated vessel motion strain analyses

A trend that becomes apparent with every case is the fact that the strain due to the isolated vessel motions decreases as the period (T_z) increases (or frequency decreases). This means that if the dynamic motion of the vessel increases, so does the strain on the pipeline.

The monotonously decreasing trend for the heave and pitch motion in deep water, visible in Figure 2-19c and Figure 2-19e, indicates that the velocity component will be governing in deep water cases. This is because the change in T_z indicates solely a change in the velocity of the vessel motion.

Another observation that stands out is the relative influence of pitch and heave. These two vessel motions are the most influential of all the vessel motions for both shallow and deep water. Surge is influential for shallow water installation. This may be due to the fact that surge is more governing in shallow water as the suspended pipeline section is shorter, and more horizontal.

At certain periods of the vessel motion, there is a local increase in strain. This is especially visible in Figure 2-18(a-f) at a T_z value of approximately seven-eight seconds and again at thirteen-fourteen seconds. This could be explained by a resonance effect of the pipeline. The natural frequency of the system is very case specific. This is due to the fact that the mass and stiffness of the system will change if the length of the suspended pipeline or pipe properties will change.

2.6.6. Fatigue damage results

The dynamic behaviour of the fatigue damage on the pipeline due to isolated vessel motions is analysed for a shallow water case of 150m water depth and a deep water case of 1496m water depth. These cases are analysed for a variety of different amplitudes and motion periods described in Section 2.6.2 and Section 2.6.3. The results are shown in Figure 2-20(a-f) and Figure 2-21(a-f).

Shallow water

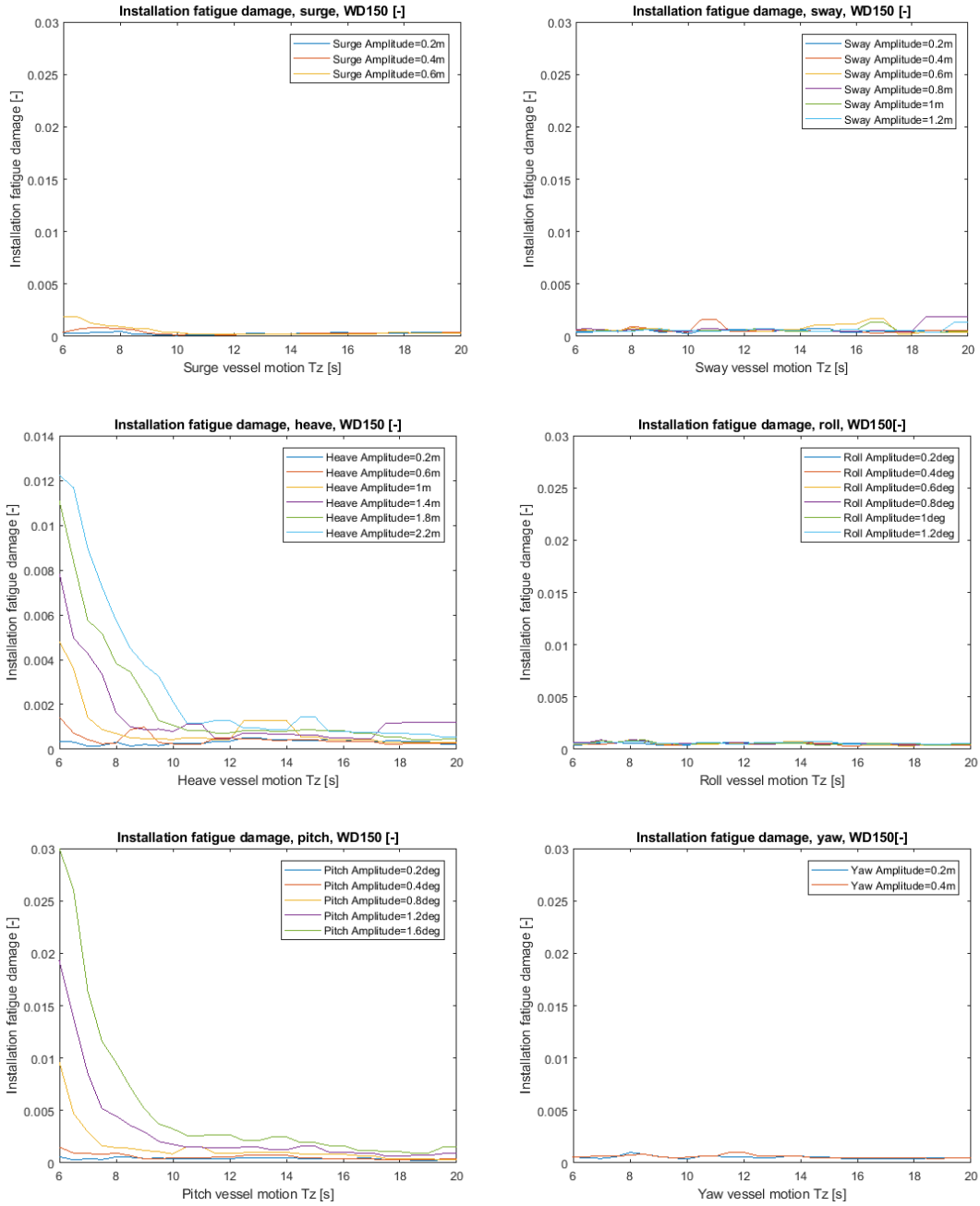

Figure 2-20 a–f Shallow water isolated vessel motion fatigue damage analyses

Deep water

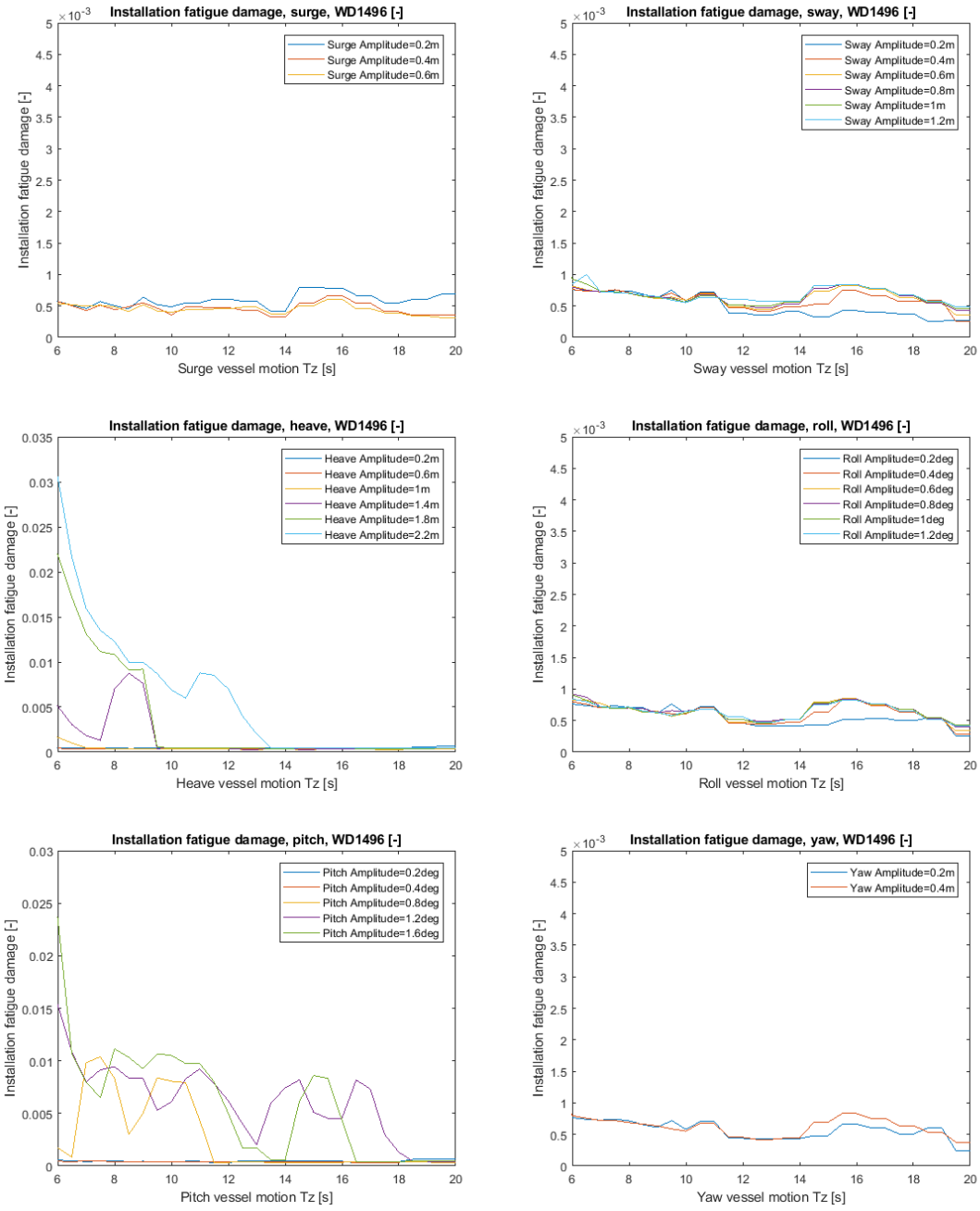

Figure 2-21 a–f Deep water isolated vessel motion fatigue damage analyses

When observing the effect the isolated vessel motions have on the installation fatigue damage, two things become apparent immediately:

- The installation damage due to most vessel motions, except heave and pitch, is relatively constant with an increasing T_z with a damage value that lies approximately at 1*10^{-3}.

  - For the shallow water case the surge motion does result in a larger installation damage at lower T_z values. This is due to the length, orientation and stiffness of the suspended pipeline.

- The heave and pitch vessel motions result in the largest installation damages and are therefore regarded as the most influential motions.

  - For the shallow water case the installation damage decreases relatively linear with an increasing T_z of the pitch and heave vessel motions. This is not the case for deep water. Also, for deep water, the heave motion of the vessel is relatively more influential than for shallow water.

  - For the deep water case, the heave and the pitch motion have some local increases in installation fatigue damage. One might expect that some of these local increases are due to resonance. However if this is the case, the increases should occur at the same frequency or T_z as resonance is dependent on the natural frequency of the system, which is dependent on the stiffness and mass of the system. However, if the displacement amplitude increases, the length of the pipeline catenary increases as well and therefore the mass of the system. This may explain why the local increases do not occur at the same T_z. Figure 2-22 illustrates the relationship between the heave motion and the fatigue damage for shallow and deep water. The installation damage has been normalised for the different amount of cycles occurring with a different T_z. The deep water case shows resonance at a heave amplitude of approximately 1.5m for a T_z of six and nine seconds. This is not the case for the shallow water case. These observations are in accordance with Figure 2-20c and Figure 2-21c.

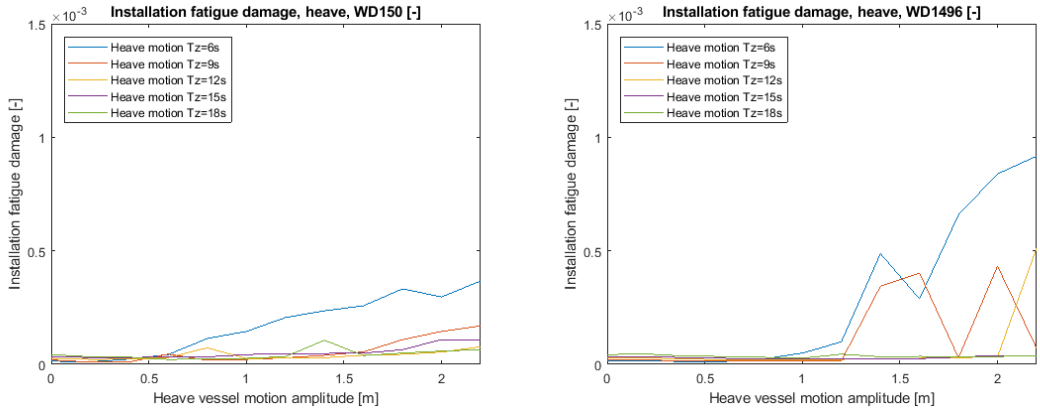

Figure 2-22 Installation fatigue damage for different heave motion amplitudes per cycle

Based on these observations, it can be concluded that the heave and pitch motion at the CoG are the most influential vessel motion with regards to maximum strain and fatigue damage. Vessel motions at the stinger tip are chosen to represent the vessel motion which means the vertical motion at the stinger tip is the most influential motion. At the stinger tip, the rotational motions at the CoG of the vessel are translated into translational motions. This means that pitch and heave at the CoG are represented by the surge and heave motion at the stinger tip.

3. METHODOLOGY

This chapter describes the methods which are used to construct statistical predictions to quickly assess the maximum strain, the DNV buckling check and the fatigue damage based on expected vessel motions. First the multiple input and the multiple input piecewise regression methods are presented and subsequently the inputs are described. Lastly, the cases which are considered during the thesis are described.

3.1. Multiple Input Regression (MIR)

A multiple input, second order polynomial regression model is used to predict the maximum output values, using more than one input variable. A polynomial function has the general form of:

$$y = a_n x^n + a_{n-1} x^{n-1} + \cdots + a_0 \tag{3.1}$$

$$with\ n = order\ of\ polynomial, a = regression\ coefficients, a_0 = constant$$

The second order polynomial function is used during this thesis for the statistical predictions. For a polynomial function with multiple inputs all possible terms are combined. For example; with two inputs: x_1 and x_2, the polynomial functions becomes:

$$y = a_5 {x_1}^2 + a_4 {x_2}^2 + a_3 x_1 x_2 + a_2 x_1 + a_1 x_2 + a_0 \tag{3.2}$$

$$with\ n = order\ of\ polynomial, a = regression\ coefficients, a_0 = constant$$

The regression coefficients are derived by performing a regression analysis on the database. The error in predictions can be visualized by scattering the predicted values against the 'actual output' derived from the simulations. Figure 3-1 shows the possible kind of error scatters.

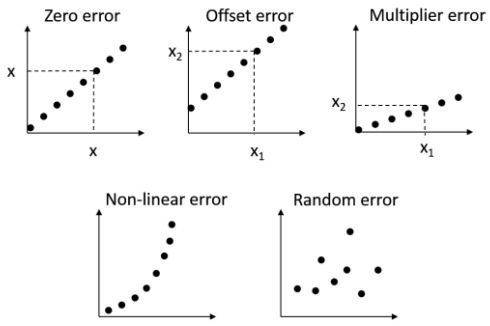

Figure 3-1 Types of error (Sri Paravastu, 2016)

The Von Mises strain and the DNV buckling check outputs are extracted from Orcaflex as a signal in the time domain. Both regressions are conducted using the same method.

The highest 5% of strain and buckling check peaks are considered per simulation. This percentage is chosen to include the values which are the most critical in terms of pipeline integrity and to reduce the amount of 'irrelevant' peaks. The distribution of strain peaks is shown in Figure 3-2(a-d) for a shallow water case of 150m water depth and a deep water case of 1496m. These distributions show that by analysing the highest 5% of strain peaks, almost the entire range of strain peaks is captured. The selection of the strain peaks shifts the probability of occurrence, especially for the higher strains. This is desirable because it means that the lowest 95% of strain peaks that are filtered out, contain a lot of similar lower strains. The filtering of the lower strain peaks increases the efficiency of the analysis and reducing noise whilst still almost capturing the entire range of strain peaks.

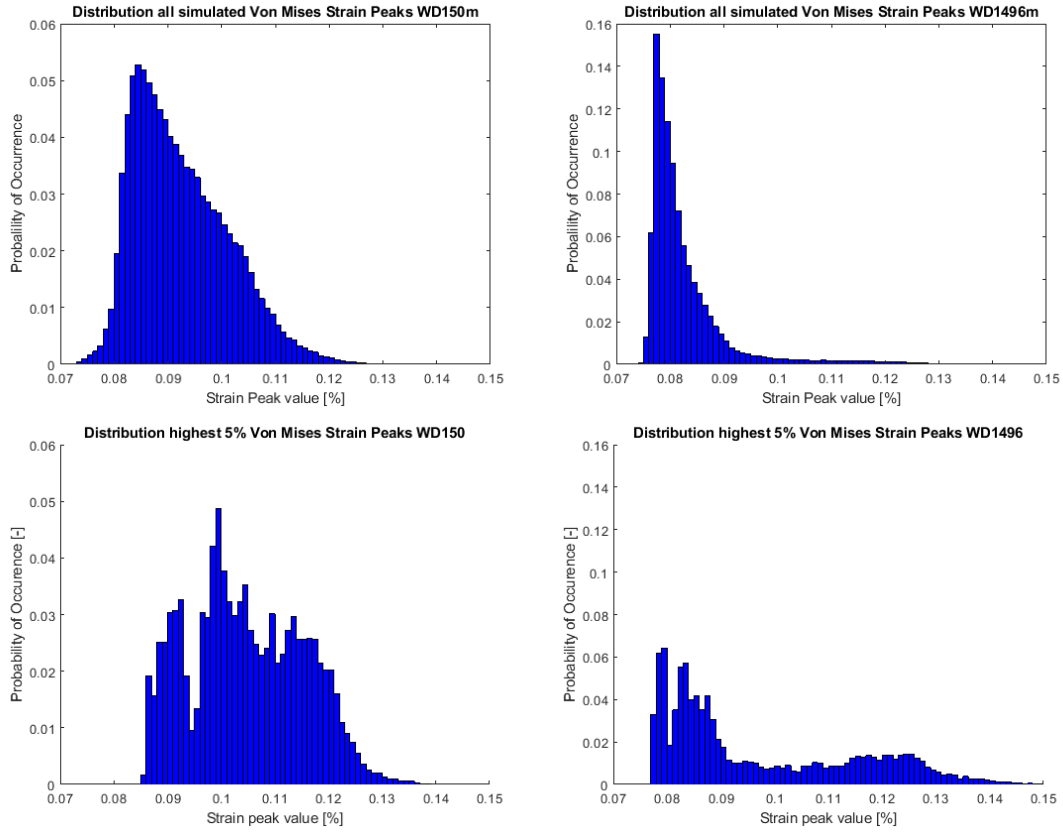

Figure 3-2 a–d Distribution of the highest 5% of strain peaks

The highest peaks are assumed to occur in the sagbend region of the pipeline catenary. The output peaks are very irregular and for this, a filter has been implemented to determine the peaks of the strain output so that peaks are not counted twice or thrice. These irregularities exist due to the fact that the output is measured for different nodes in the sagbend region of the pipeline catenary and the maximum value is chosen. If the output was measured for the same node, the signal would be smoother. The maximum strain values occurring in the pipeline are the most critical in terms of

pipeline integrity, no matter where they occur in the sagbend region of the pipeline. The filter that is in place chooses the highest output value of every peak as shown in Figure 3-3.

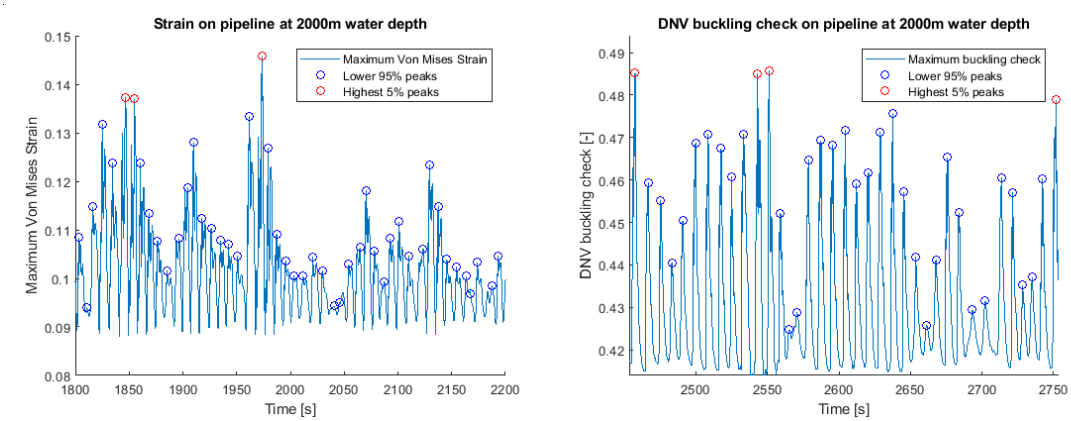

Figure 3-3 Example Von Mises strain and buckling check peaks for 2000m water depth

This method is based on a method that was developed during a previous study conducted by Sri Paravastu (2016). Within this study a multiple input linear regression has been introduced. One of the main differences between these methods is that the method used during this thesis does not use a linear regression but a second order polynomial regression. The other main difference is the fact that during this thesis, the highest 5% of output values are chosen. Previously this was just one value; the most extreme output per simulation.

3.2. Multiple Input Piecewise Regression (MIPR)

A Multiple Input Piecewise Regression is used to increase the accuracy of the strain and buckling check prediction by dividing the corresponding in- and outputs into groups with comparable dynamic behaviour. This method follows the same procedure as the MIR in Section 3.1. However, the corresponding in- and outputs are divided into different groups. By splitting the in- and outputs in different groups that generally have more comparable behaviour, the prediction of the whole system can be improved (A. Miller, 2002). During the study of Sri Paravastu (2016), a method is presented in which corresponding in- and outputs are divided into groups. However, the division of data is not based on comparable behaviour during this aforementioned study, which the author does recommend.

The MIPR method is used to predict the Von Mises strain and the DNV buckling check. The fatigue damage prediction will be constructed using the MIR method due to the fact that the fatigue damage is averaged over time. This means the pipeline behaviour is averaged as well, reducing the need to split the data into groups of similar behaviour to improve the prediction.

The group of corresponding in- and outputs is split into four smaller groups, further referenced as datasets, based on the value of the heave motion of the vessel, which is the most influential motion according to the isolated motion analysis (Section 2.6). Since this variable has the most dominating influence on the output extrema, any increase in its extreme value is considered to increase the output maxima. The absolute values for the acceleration of the heave will be analysed for the split as it showed the overall best results with regards to the correlation to the output value.

The stinger tip motions that caused the top five percent of strain peaks are analysed. The heave acceleration distribution is displayed for 150m water depth and for 1496m water depth in Figure 3-4. The heave acceleration distribution is almost identical for both water depths despite the fact that the stinger tip motions are not excited by the same sea states. The relevant range of sea states is further discussed in Section 3.3.1.

Dataset 1: All data below the mean acceleration of the entire group of corresponding in- and outputs, this will account for approximately 55% of the analysed strain peaks.

Dataset 2: All corresponding in- and outputs with a heave acceleration value between the mean and the first positive standard deviation, this will account for approximately 27% of the analysed strain peaks.

Dataset 3: All corresponding in- and outputs with a heave acceleration value between the first and second positive standard deviation, this will account for approximately 16% of the analysed strain peaks.

Dataset 4: All corresponding in- and outputs with a heave acceleration value that exceeds the second standard deviation, this will account for approximately 3% of the analysed strain peaks.

Each of the four datasets is sub-sequentially split in different sub-datasets according to the direction of the motion.

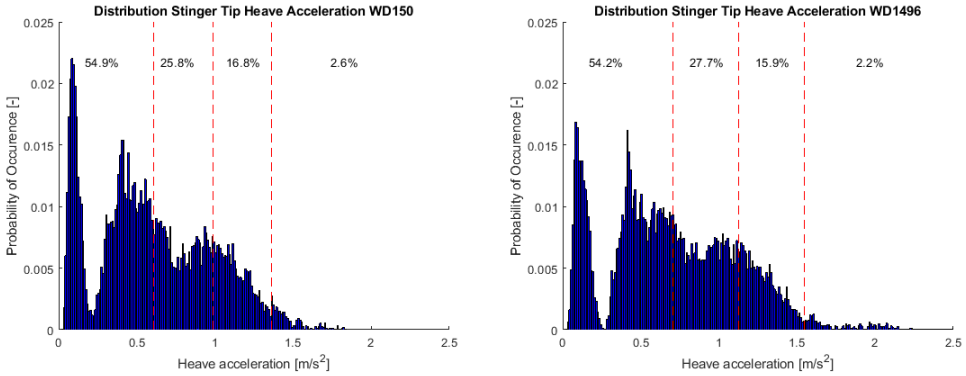

Figure 3-4 PDF heave acceleration shallow and deep water

Motions in different directions might result in a different dynamic motion behaviour of the pipeline. Figure 3-5 and Figure 3-6 show the distribution of highest 5% of the Von Mises strain peaks and their corresponding heave motion acceleration and velocity peaks. These are clearly not symmetrical for the positive or negative direction values. This indicates that the direction of motion does influence the pipeline behaviour. So grouping positive and negative maximum motions should result in multiple sub-sets with similar behaviour. A positive heave motion will correlate differently with the Von Mises strain than a negative heave motion. This is because of the tension in the pipeline: a heave motion in the positive direction will increase the tension on the pipeline catenary and a negative heave motion will decrease the tension in the pipeline catenary which will cause the pipeline to become more prone to buckling.

Figure 3-5 and Figure 3-6 also indicate that the highest strain peaks are corresponding to a negative (downward) heave velocity. This is due to the fact that with a downward motion, the tension acting on the pipeline would decrease which will increase the bending of the pipe and therefore increase the Von Mises strain. These figures also indicate that the difference in behaviour is less extreme for the shallow water case. This is due to the difference of pipe properties, the length and weight of the suspended pipeline. The deep water case has a suspended pipeline that is less stiff, and weighs more. This causes the pipe of the deep water case to bend more than that of the shallow water case which explains the difference in dynamic behaviour of the pipeline.

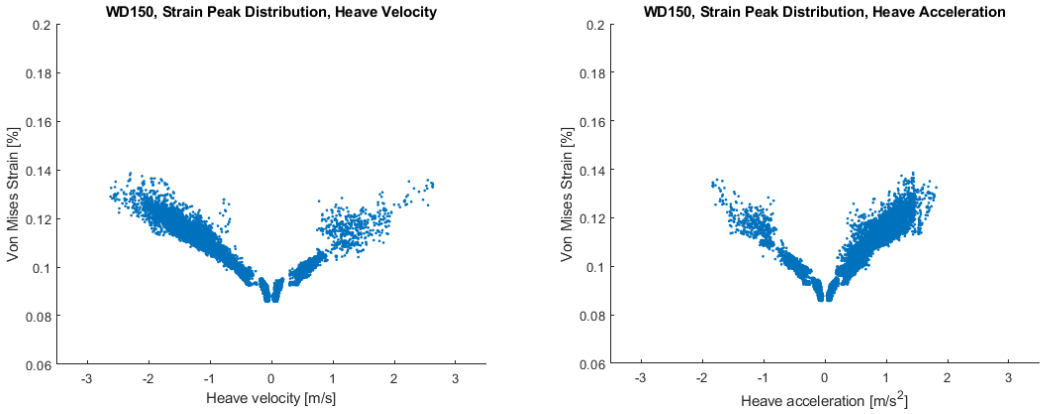

Figure 3-5 Distribution of Von Mises strain peaks with corresponding heave motion peak/valley values, shallow water

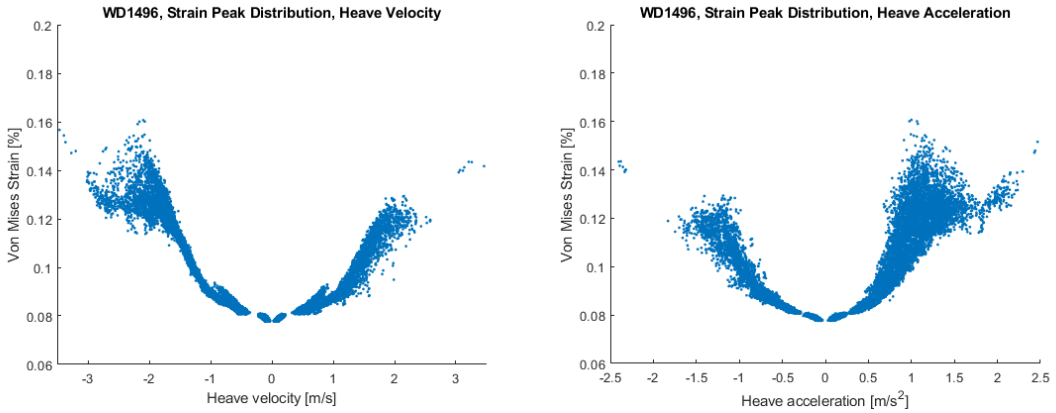

Figure 3-6 Distribution of Von Mises strain peaks with corresponding heave motion peak/valley values, deep water

- Each dataset is divided into 2 sub-datasets [Table 3-1].

    i. Sub-dataset containing motions with a negative direction
    ii. Sub-dataset containing motions with a positive direction

The procedure of constructing a statistical prediction with the different sub-datasets is almost the same as for the multiple input regression method. The only difference is that it is repeated for every sub-dataset.

- This method results in eight different sub-datasets with a different prediction curve for each set.

Parameter	**Heave acceleration range**	**Heave Velocity**
Sub-dataset 1	$< \mu$	Negative
Sub-dataset 2		Positive
Sub-dataset 3	$\mu - (\mu + \sigma)$	Negative
Sub-dataset 4		Positive
Sub-dataset 5	$(\mu + \sigma) - (\mu + 2\sigma)$	Negative
Sub-dataset 6		Positive
Sub-dataset 7	$> (\mu + 2\sigma)$	Negative
Sub-dataset 8		Positive

Table 3-1 Direction of the heave motion divided in sub-datasets

The total RMSE of every sub-dataset is determined, the following formula is then used to get the RMSE of all the subsets combined per case:

$$RMSE_{total} = \sqrt{\frac{\sum_{n=1}^{n_0} (RMSE_{sub-datasets})^2}{n_0}},\ with\ n_0 = number\ of\ subdatasets \tag{3.3}$$

3.3. Input

3.3.1. Data Generation

To acquire a database of outputs and corresponding stinger motion inputs, a range of sea states is simulated in Orcaflex. The database further referred to in this thesis consist of a certain amount of corresponding in- and outputs that is acquired from every simulated sea state. For the strain and buckling check prediction, this number will correspond to the highest 5% of stain peaks of each sea state simulation. For the fatigue damage, the number of corresponding in- and outputs will be same number as the number of sea-state simulations conducted since only one output is extracted per simulation. This database will be used for the regressions conducted during this thesis. The simulated sea states consists of uni-directional JONSWAP wave spectra. The range of sea states that are simulated are as follows:

- H_s: 1,1.5,2,…3.5 meters
- T_z: 4,5,6,…10 seconds
- θ: 0,10,20,…180 degrees

The sea states described above are assumed to excite all ranges of stinger tip motions that would occur during installation. The range of the significant wave height (H_s) is based on the design limit of the Solitaire vessel during pipeline installation. The time period of the waves (T_z) is simulated from four up to ten seconds because this is the range of the response amplitude operator (RAO) of the Solitaire vessel defined by Allseas. All incoming wave angles up to 180 degrees are simulated. This is because the hull of a vessel is symmetrical along the longitudinal section from bow to stern. The vessel motion response should also be symmetrical due to the fact that the waves simulated are uni-directional.

The 150m water depth case, is only simulated up to a significant wave height of 3 meters. Increasing the sea state beyond 3 meters causes the pipeline to ‘bounce’ on the stinger, deteriorating the quality of the data. The parameters from Table 3-2 represent all stinger tip motions that result from the sea state simulations.

Parameter	Description
X_1	Surge displacement
X_2	Surge velocity
X_3	Surge acceleration
X_4	Sway displacement
X_5	Sway velocity
X_6	Sway acceleration
X_7	Heave displacement
X_8	Heave velocity
X_9	Heave acceleration

Table 3-2 Input parameters

3.3.2. Motion measurements

Extreme motion

Extreme values of strain are likely to be caused by extreme motions occurring moments before the strain peak. The extreme motion measurement determines the most extreme motion value within a time window. This measurement will be used for the Von Mises strain prediction and the DNV buckling check prediction.

Window

A window is chosen in which the input motions are measured from the conducted simulations. A visual example of the window is shown in Figure 3-7. The general concept of the window is discussed in this section and the determination of the width of the window is further discussed in Section 4.1.1.

This window is located before the occurrence of an output peak. The length of the window is based on the length of the peak periods of the motions. The largest overall peak period is determined (valley to valley) and all relevant motions that cause the peak strain should occur within this time period.

This results in a certain range of window length options. These windows are all considered and the window that results in the prediction with the lowest root mean square error is chosen. Choosing an appropriate window is essential for the accuracy of the prediction model. Peaks of different motions occur at different moments in time so it is essential that the length of the window includes these peaks.

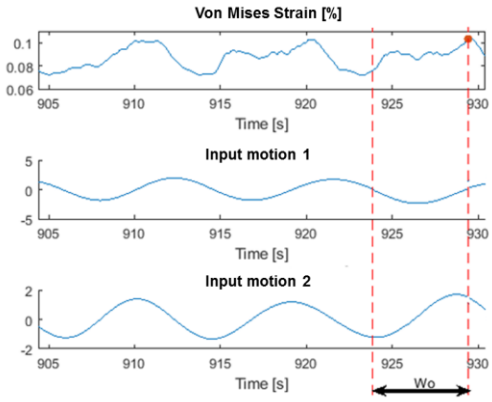

Figure 3-7 Measurement window example

Input motions

From the isolated motion analysis it was concluded that the strain peaks are influenced by the dynamic vessel motions. Based on this analysis the following stinger tip motions are considered as an input for the regression:

Shallow water
- Surge & Heave

Deep water
- Heave

It could not be concluded from the results of the dynamic isolated vessel motion analysis which motion component is more relevant to use as an input for the regression. Therefore, there are four combinations of input motions under consideration:

- Displacement
- Velocity
- Acceleration
- Acceleration and velocity

All combinations are considered and presented in Section 4.1.1 for a shallow water and a deep water case.

Integrated motion per cycle
The fatigue installation damage is calculated as an accumulation of the installation damage per sea-state simulation. This means that there will be a single fatigue installation damage value per sea state simulation.

The stinger tip motions that are analysed for the prediction of the fatigue installation damage should be an accumulated value as well. The absolute value of the stinger tip motions per sampling step (0.1s) are accumulated for the entire one-hour simulation and divided by the amount of motion cycles. This will result in an integrated motion value per cycle. This value is used as input value for the fatigue installation damage prediction
The motions components that are considered as an input for the regression are:

- Displacement
- Velocity
- Acceleration

All three motions are considered and discussed in Section 4.2.

During the isolated motion analysis it is determined that the stinger tip motion in the vertical direction (heave) is the most influential motion for fatigue installation damage, it is clear that the heave at the stinger tip should be one of the motion inputs for the multiple input regression. The heave motion at the stinger tip will also include the pitch motion as discussed in Section 3.3.2. It is essential to determine further which combination of motions is the most relevant to predict the fatigue installation damage.
There are three combinations under consideration:

- Heave & Surge
- Heave & Sway
- Heave, Surge & Sway

The three possibilities are all considered and discussed as well in Section 4.2.

3.4. Cases

The dynamic behaviour of the pipeline differs for numerous varying pipelay factors like water depth, pipe properties, set tension and stinger orientation. Eight different combination of factors are presented to analyse this dynamic behaviour.

Water depth

Water depth is a governing factor during pipelay operations. The water depth determines the length of suspended pipeline between the stinger and the seabed. Therefore it influences the set tension and stinger orientation as well. The pipe must be able to withstand the pressures at large depths and lie stable on the seabed. That means that the water depth also determines the pipe properties. The different water depths that are being analysed are:

- 150m
- 280m
- 450m
- 650m
- 1000m
- 1496m
- 2000m

Pipe properties

Two different set of pipe properties have been chosen based on the water depth. It is important not to consider too many different sets of pipe properties as results from analyses will be less comparable. The two sets of pipe properties, A and B, used during this thesis are listed below in Table 3-3. The properties in Table 3-3 are defined by Allseas and the axial stiffness is calculated with the following formula:

$$k_{axial} = E * \frac{\pi}{4} * (OD^2 - ID^2), \quad (3.4)$$

$$with\ E = Young's\ Modulus\ OD = Outside\ Diameter\ (without\ coating)\ ID = Internal\ Diameter$$

Pipeline section			**A**	**B**
Overall outside diameter		[mm]	616.6	515.2
Internal diameter		[mm]	560.4	456.2
Wall thickness		[mm]	24.6	25.9
Axial Stiffness		[kN]	$9.359*10^6$	$8.120*10^6$
Material grade		[-]	DNV 450 SFDU	
Fabrication type		[-]	SAWL	
SMYS		[N/mm^2]	450	
SMTS		[N/mm^2]	535	
Young's Modulus		[Pa]	$207*10^9$	
Anti-corrosion coating	Type	[-]	3LPP	
	Density	[kg/m^3]	921	
	Thickness	[mm]	3.6	
Dry weight	Empty	[N/m]	3544.3	3073.1
	Flooded	[N/m]	6024.4	4716.7
Submerged weight	Empty	[N/m]	539.8	976.9
	Flooded	[N/m]	3019.9	2620.5
Pipe section length		[m]	12.2	

Table 3-3 Pipe section properties

Tension

To keep the suspended pipeline in place and to prevent the pipeline from buckling, tensioners are used to keep the pipeline at a constant tension. The tension provided by the tensioners have two distinctions: static tension and dynamic tension.

The static tension for each load case is calculated to provide a stinger tip separation of 0.3m between the stinger tip and the pipeline. The tension is further determined by the weight of the suspended pipeline and the maximum allowable strain on the pipeline. The static tension is, as the name indicates, the required tension the tensioners should apply to the pipeline in a static pipelay configuration. That means without considering dynamic loads acting on the pipeline or vessel. So the dynamic tension is the required tension with the dynamic loads considered.

The number of pipe properties has been reduced to two sets as previously described. This means that some required dynamic tensions need to be recalculated. To recalculate the dynamic tension of the pipe properties, the dynamic amplification factor has to be considered. The dynamic tensions are calculated using the following formula and the values are presented in Table 3-4 as the 'set tension':

$$T_{dyn,new} = \frac{T_{dyn,original\ pipe}}{T_{stat,original\ pipe}} * T_{stat,new} \tag{3.5}$$

Stinger orientation

The stinger can be rotated to attain the most optimal position for the pipelay operation. By rotating the stinger, one can influence the lift-off angle of the pipeline. In shallow water, the pipeline leaves the vessel in a more horizontal position and in deep water the pipeline leaves the stinger in a more vertical orientation. If the rotation of the stinger is positive, the stinger rotates upwards or clockwise. A negative rotation indicates that the stinger rotates downwards or counter-clockwise.

Cases

The eight different cases are summarized in Table 3-4.

	Water depth [m]	Pipeline section [-]	Set tension [t]	Stinger rotation [deg]	Stinger radius [m]
Case 1	150	A	299	+0.8	260
Case 2	280	A	400	0	140
Case 3	450	A	483	0	140
Case 4	650	A	712	0	140
Case 5	650	B	991	0	140
Case 6	1000	B	1499	0	140
Case 7	1496	B	2200	0	140
Case 8	2000	B	2955	0	140

Table 3-4 Summary of different installation cases

4. RESULTS & ANALYSIS

This chapter describes the results for the determination of the prediction method based on multiple input regression for the maximum strain, buckling check and fatigue damage prediction. Subsequently the predicted results for both MIR and MIPR methods are presented and analysed.

4.1. Maximum strain & DNV buckling check

The maximum strain prediction and the buckling check prediction are conducted in an identical manner and are therefore presented together.

4.1.1. Results method

To determine which method predicts the strain the most accurately, two cases are compared to one another: a shallow water and a deep water case. Case 1; 150m water depth, is chosen to represent the shallow water case and Case 7 is chosen to represent the deep water case. General parameters of these cases and simulations are listed in Table 4-1.

Parameter		Shallow water	Deep water
Water Depth	[m]	150	1496
Vessel		Solitaire	
Dynamic integration parameters			
Integration time step	[s]	0.1	
Sampling interval	[s]	0.1	
Simulation time	[s]	3600	
Ramp up time	[s]	60	
Number of simulations	[-]	665	798
Data Points	[-]	66,131	79,632

Table 4-1 Orcaflex simulation parameters

Window

To determine a window which indicates the length of the time period in which the input signals are analysed, the delay of the motion signal peaks must be analysed for each motion and each case. The highest recorded peak period of the strain signal is 8.6s (valley to valley). The peaks of different motion components should be present within this time period. The delay between the strain peak and the largest velocity and acceleration extrema is therefore measured for a window width of ten seconds (8.6s rounded up). An overview of this delay is shown in Table 4-2. The distributions are also illustrated as probability density functions in Appendix B.

Table 4-2 shows the most probable period in which the extreme motion peak is measured. This value varies between approximately 0 – 4.5 seconds. The most probable delay between the occurrence of the strain peak and the heave velocity extremes increases as the water depth increases. This is the result of the increase of pipeline catenary length with increasing water depth, which increases the distance between the stinger tip and the location the maximum strain occurs.

What is interesting to observe, is that the most probable delay between the heave and surge acceleration peaks and the corresponding strain peaks of the cases with a relative shallow water depth is zero seconds. This can be explained by the fact that the displacement of these motions cause the pipeline to move and therefore also causes the strain in the pipeline. The acceleration of any motion is in anti-phase with the displacement of that motion and therefore the acceleration peak occurs at more or less the same time as the strain peak for shallow water cases. Cases with a deeper water depth show an increased delay between the occurrence of the strain peaks and the acceleration peaks due to the increased length of the pipeline catenary. The motions take a longer time to travel from the stinger tip to the lower sagbend area of the pipeline

	Vessel Motion		Most probable delay [s]
Case 1: 150m	Surge	Velocity	2.5
		Acceleration	0.0
	Heave	Velocity	2.3
		Acceleration	0.0
Case 2: 280m	Surge	Velocity	2.0
		Acceleration	0.0
	Heave	Velocity	1.8
		Acceleration	0.0
Case 3: 450m	Heave	Velocity	1.7
		Acceleration	0.0
Case 4: 650m (A)	Heave	Velocity	2.4
		Acceleration	0.4
Case 5: 650m (B)	Heave	Velocity	2.6
		Acceleration	0.8
Case 6: 1000m	Heave	Velocity	3.5
		Acceleration	2.3
Case 7: 1496m	Heave	Velocity	3.7
		Acceleration	2.2
Case 8: 2000m	Heave	Velocity	4.2
		Acceleration	2.2

Table 4-2 Delay between strain peak and motion peak

Based on these delay values, a window value is needed that exceeds the 4.2 seconds and is within the limit of the largest measured peak period, which is 8.6 seconds. These values are both rounded up to account for a margin of measurement error and result in a window width that lies between five and ten seconds. One thing to keep in mind is that the delay statistics that are presented in Table 4-2, are based on the time between the largest motion peaks and the strain peaks, this does not mean that is the most relevant motion peak.
The predictions presented in Section 4.1.3 are all simulated with a measurement window that lies between five and ten seconds. The window that resulted in the smallest overall RMSE is the six second window. All predictions in Chapter 4 are therefore conducted with a measurement window of six seconds.

Motion Input
The isolated motion analysis concluded that the strain peaks are mostly influenced by the vertical stinger tip motion for both shallow and deep water. For shallow water, the surge at the stinger tip is influential as well. However, it is not yet clear which motion components are the most relevant. Therefore, there are four combinations of input motions under consideration as discussed in Section 3.3.3:

- Displacement
- Velocity
- Acceleration
- Velocity and acceleration

Results of the multiple input regressions for each motion component are shown in Figures 4-1(a-d) for shallow water and Figures 4-2(a-d) for deep water.

Shallow water

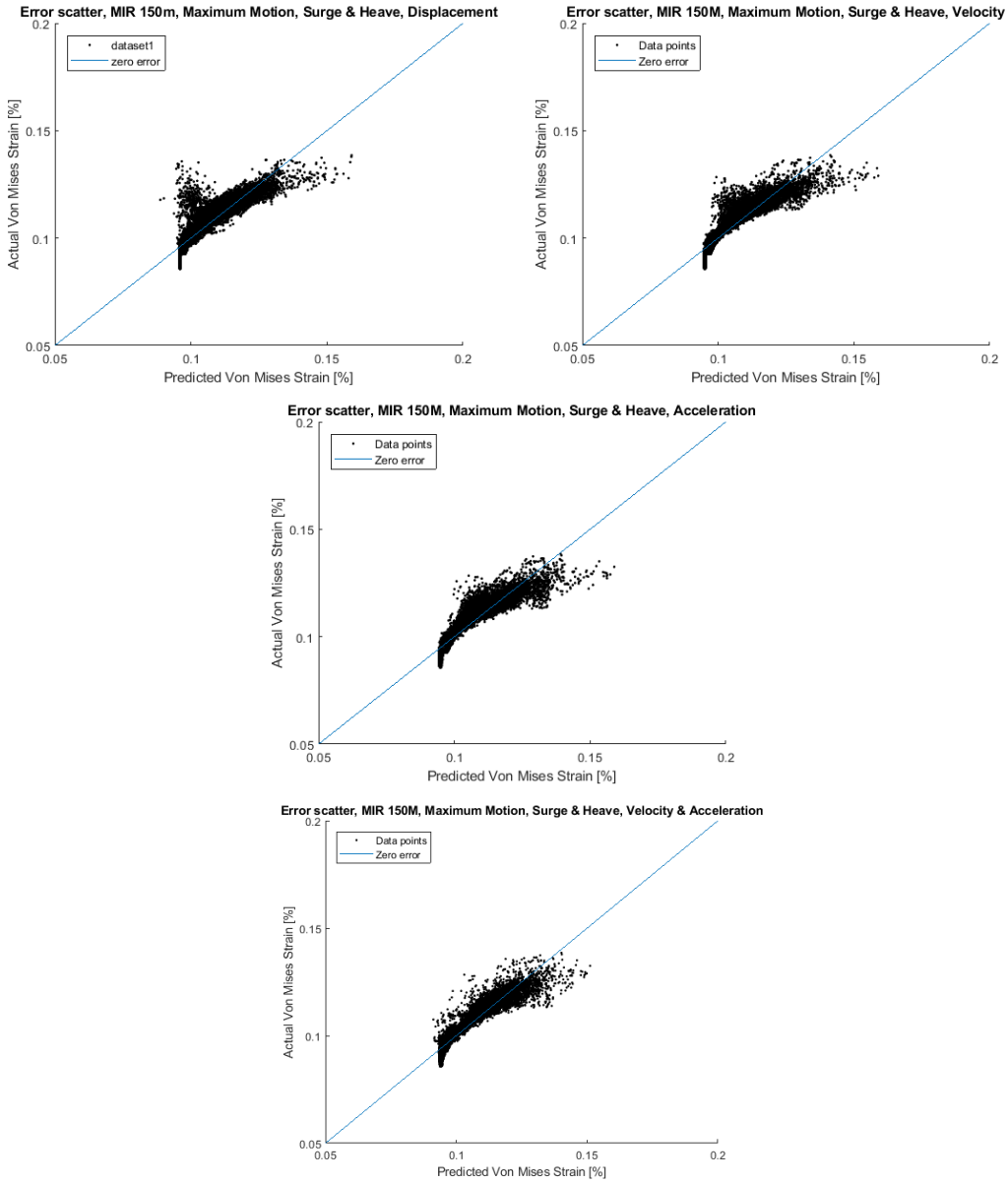

Figure 4-1 a–d Error scatters MIR shallow water motion components

	Stinger tip motions 150m	Stinger tip motions 150m	Stinger tip motions 150m	Stinger tip motions 150m
Input Variables	Surge displacement X_1 Heave displacement X_7	Surge velocity X_2 Heave velocity X_8	Surge acceleration X_3 Heave acceleration X_9	Surge velocity X_2, Surge acceleration X_3 Heave velocity X_8, Heave acceleration X_9
Regression curve formula	$Y_{predict} = -0.0176{X_1}^2 + 0.0039{X_7}^2 + 3.9678 * 10^{-4}X_1X_7 - 0.0138X_1 - 3.3346 * 10^{-4}X_7 + 0.0960$	$Y_{predict} = -0.0220{X_2}^2 + 0.0092{X_8}^2 + 0.0062X_2X_8 + 0.0138X_2 - 0.0011X_8 + 0.0951$	$Y_{predict} = 0.1911{X_3}^2 + 0.0127{X_9}^2 + 0.0136X_3X_9 - 0.0219X_3 + 0.0016X_9 + 0.0948$	$Y_{predict} = 0.3857{X_2}^2 + 0.6323{X_3}^2 + 0.0204{X_8}^2 + 0.0656{X_9}^2 + 0.9497X_2X_3 - 0.0393X_2X_8 - 0.0676X_2X_9 - 0.0496X_3X_8 - 0.0782X_3X_9 + 0.0662X_8X_9 + 0.0078X_2 - 0.0020X_3 - 0.0185X_8 - 0.0206X_9 + 0.0940$
Measurement	Extreme motion	Extreme motion	Extreme motion	Extreme motion
RMSE	0.0051	0.0043	0.0042	0.0038

Table 4-3 Parameters MIR regressions shallow water

Deep water

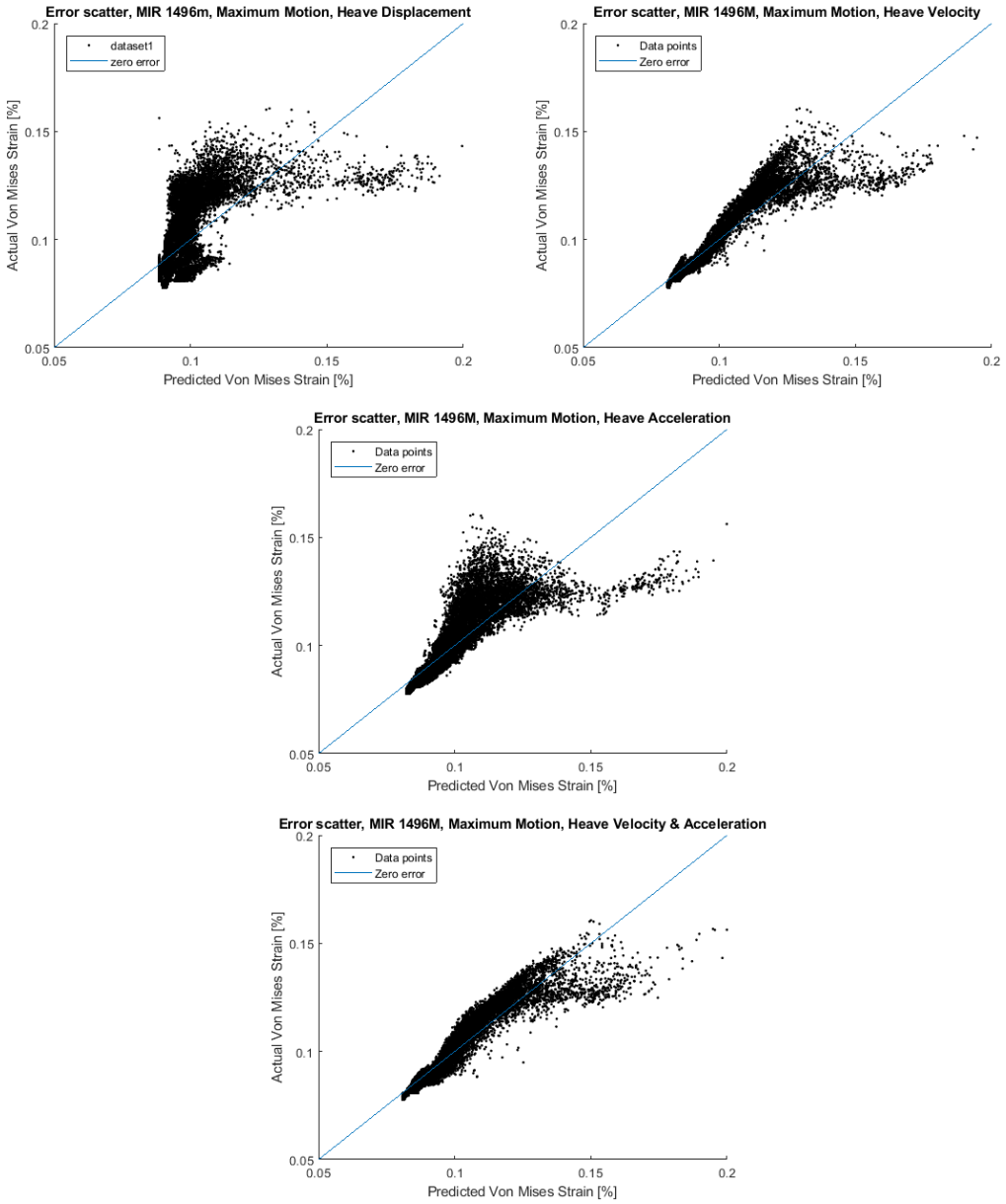

Figure 4-2 a–d Error scatters MIR deep water

	Stinger tip motions 1496m	Stinger tip motions 1496m	Stinger tip motions 1496m	Stinger tip motions 1496m
Input Variables	Heave displacement X_7	Heave velocity X_8	Heave acceleration X_9	Heave velocity X_8, Heave acceleration X_9
Regression curve formula	$Y_{predict} = 0.0038{X_7}^2 - 0.0056X_7 + 0.0905$	$Y_{predict} = 0.01{X_8}^2 - 0.0021X_8 + 0.0813$	$Y_{predict} = 0.0193{X_9}^2 + 0.0047X_9 + 0.0828$	$Y_{predict} = 0.0472{X_8}^2 + 0.0693{X_9}^2 + 0.1026X_8X_9 - 0.0082X_8 - 0.0095X_9 + 0.0810$
Measurement	Extreme motion	Extreme motion	Extreme motion	Extreme motion
RMSE	0.0135	0.0063	0.0093	0.0057

Table 4-4 Parameters MIR regressions deep water

Based on the error scatters in Figure 4-1(a-d) and Figure 4-2(a-d) and Table 4-3 and Table 4-4, observations can be made with regard to the relevance of the components:

Single motion component used as input with the least amount of error:

Shallow water	Deep water
• Acceleration	• Velocity

Single motion component used as input with the highest amount of error:

Shallow water	Deep water
• Displacement	• Displacement

These observations are in accordance with the observation made by Sri Paravastu (2016) when comparing the correlation of different motion components on the maximum strain value.

For both shallow and deep water, the prediction is the most accurate when using both the heave velocity and the heave acceleration as inputs for the regression. This is especially visible for the higher actual strain peaks (located at approximately 0.15%) for deep water. If inputs are measured with the extreme motion measurement (Section 3.3.2), only the motion peak values are measured. If only one of the aforementioned motion components is used as an input, information would get lost regarding the rate of change of the motion. This information is included if both the acceleration and velocity are used as an input. Since the rate of change of the motions is relevant to the strains occurring in the pipeline, using both the velocity and acceleration components as an input for the regression results in the best correlation for both deep and shallow water as can be observed in Table 4-3 and Table 4-4.

Due to the fact that the acceleration is a time derivative of the velocity, a phase difference occurs between these motion components. The acceleration is in anti-phase with the displacement component. The displacement of the pipeline causes the strain on the pipeline. This is the reason for the acceleration peak to occur at the same moment as the displacement peak or valley. The strain peak occurs moments after the stinger tip displacement due to the travel time of the motion through the pipeline catenary. It is important that the same combination of motion component peaks and valleys is measured for every strain peak. Therefore, whenever the measured motion velocity peak is negative, the acceleration peak will be measured as the positive peak a few moments after the occurrence of the velocity peak and vice versa. This measurement of motion components is illustrated in Figure 4-3. These are two measurements within the same time history.

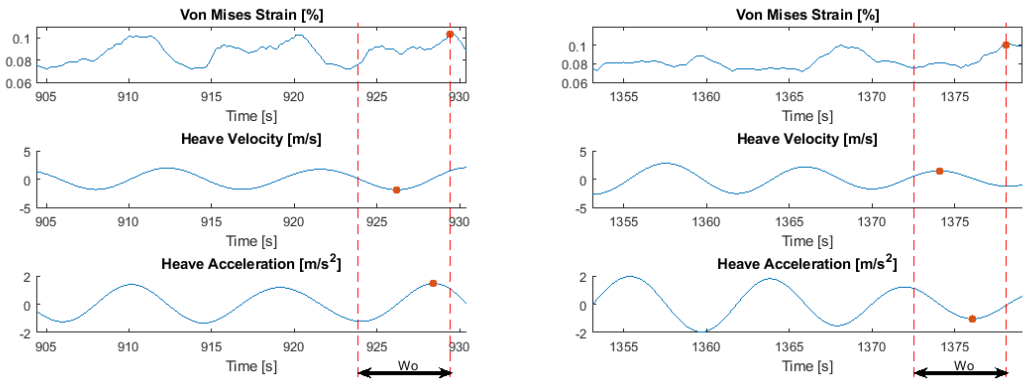

Figure 4-3 Corresponding motion peaks within window

4.1.2. Results MIR

The results for the MIR method for the strain prediction are presented for a shallow water and a deep water case of 150m and 1496m respectively in Figure 4-4 and Table 4-5.

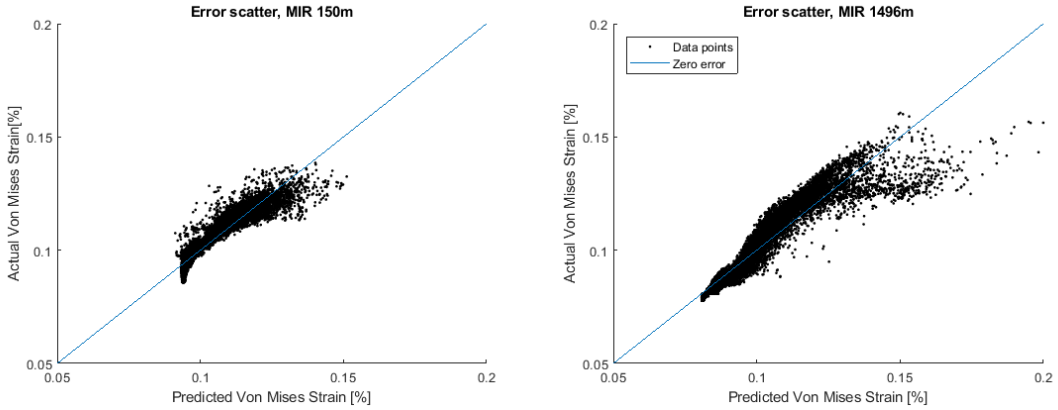

Figure 4-4 Error scatters MIR shallow and deep water

	Stinger tip motions 150m	Stinger tip motions 1496m
Input Variables	Surge velocity X_2, Surge acceleration X_3 Heave velocity X_8, Heave acceleration X_9	Heave velocity X_8, Heave acceleration X_9
Regression curve formula	$Y_{predict} = 0.3857{X_2}^2 + 0.6323{X_3}^2 + 0.0204{X_8}^2 + 0.0656{X_9}^2 + 0.9497X_2X_3 - 0.0393X_2X_8 - 0.0676X_2X_9 - 0.0496X_3X_8 - 0.0782X_3X_9 + 0.0662X_8X_9 + 0.0078X_2 - 0.0020X_3 - 0.0185X_8 - 0.0206X_9 + 0.0940$	$Y_{predict} = 0.0472{X_8}^2 + 0.0693{X_9}^2 + 0.1026X_8X_9 - 0.0082X_8 - 0.0095X_9 + 0.0810$
Measurement	Extreme motion	Extreme motion
RMSE	0.0038	0.0057

Table 4-5 Parameters MIR regressions shallow & deep water

The deep water case shows a larger error for higher strain peaks than for lower strain peaks as can be observed in Figure 4-4. This is visible within the predicted strain range of 0.15% and 0.2%. These higher strains are critical to operational limit and therefore it is crucial that these higher strains are predicted accurately. This is why it is proposed to divide the corresponding in- and outputs into groups with comparable dynamic behaviour. To increase the accuracy of the statistical predictions, the MIPR method is implemented, which is described in Section 3.2.

4.1.3. Results MIPR Von Mises Strain

The results for the MIR method for the strain prediction can be improved and therefore the MIPR method is implemented to construct a prediction for each case considered in this thesis. An overview of the results of the MIPR method are shown in Table 4-6, Figures 4-5(a-c) and Figures 4-6(a-e). The mean and standard deviation heave acceleration at the stinger tip are presented as these are used for dividing the corresponding in- and outputs, as is described in Section 3.2. The resulting prediction formulas are presented in Appendix C.

General parameters		**Case 1**	**Case 2**	**Case 3**	**Case 4**	**Case 5**	**Case 6**	**Case 7**	**Case 8**
Water Depth	[m]	150	280	450	650	650	1000	1496	2000
Pipeline section	[-]	A				B			
Static case parameters									
Top Tension	[kN]	299	400	483	712	991	1499	2200	2955
Von Mises Strain	[%]	0.0793	0.0776	0.0756	0.0591	0.0769	0.0659	0.0761	0.0935
Regression parameters									
Input Variables		Surge velocity X_2, Surge acceleration X_3 Heave velocity X_8 Heave acceleration X_9		Heave velocity X_8 Heave acceleration X_9					
μ heave acceleration	[m/s^2]	0.6083	0.7407	0.6616	0.7458	0.7008	0.6929	0.7064	0.7340
σ heave acceleration	[m/s^2]	0.3774	0.4084	0.4493	0.4542	0.4381	0.4257	0.4203	0.4429
RMSE MIPR	[-]	0.0018	0.0020	0.0021	0.0016	0.0020	0.0018	0.0019	0.0016

Table 4-6 Results MIR & MIPR strain error scatters

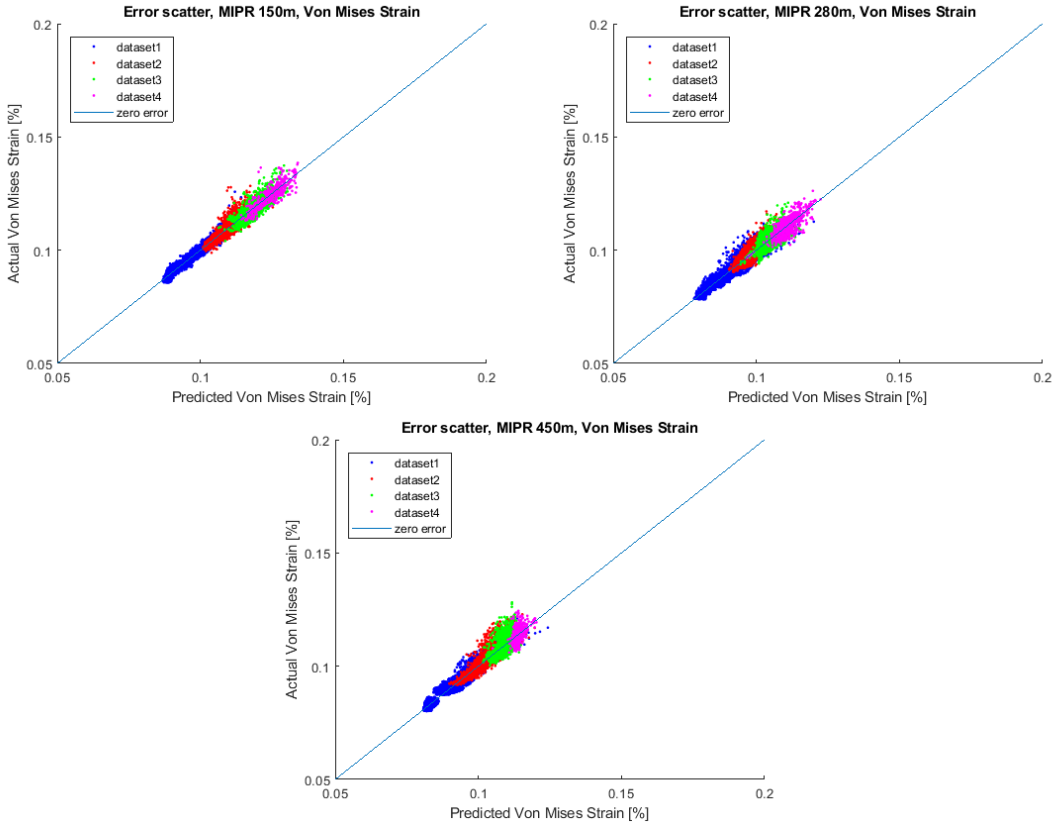

Figure 4-5 a–c Error Scatter MIPR for case 1-3

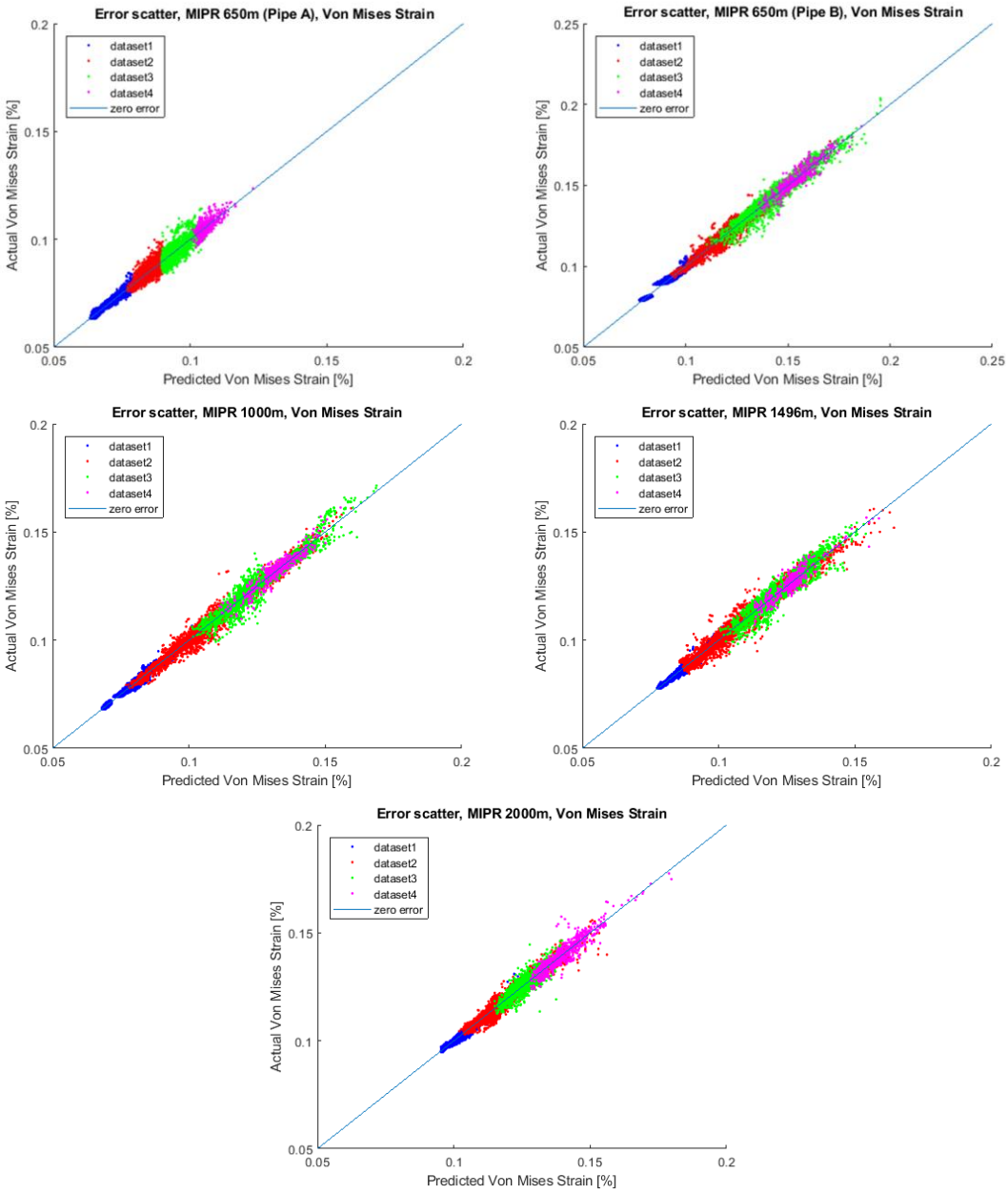

Figure 4-6 a–e Error Scatter MIPR for case 4-8

As can be observed from the comparison of the RMSE and the shape of the error scatters from the MIPR results and the MIR results (Section 4.1.2), the piecewise method significantly improves the Von Mises strain predictions.

The most valuable effect is that, because the high and low strain peaks are analysed separately, the error for the higher strain peaks is much lower than with the MIR method.

The comparison between Figure 4-6a and Figure 4-6b indicates that different pipe properties have a major influence on the pipeline behaviour. The most apparent difference between the error scatters of these two cases is the peak strain range. Case 5 is simulated with the pipe properties of pipeline B and has a much larger strain range than case 4 which is simulated with the pipe

properties of pipeline A. The largest contributions to this difference in strain range are the difference in axial stiffness and difference in the required set tension of the two pipes. A larger set tension is also required to provide the required tip separation. As a result, the range of strains acting on the pipeline will be higher with the pipe section B properties than with the pipe section A properties.

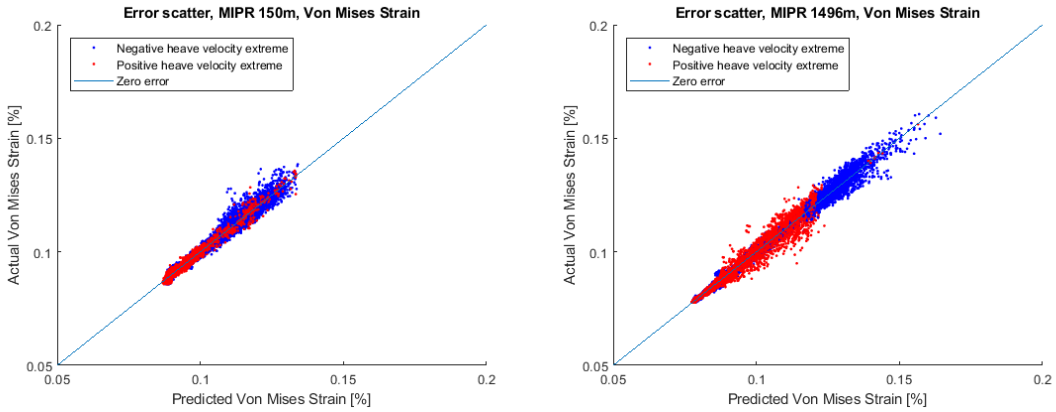

Figure 4-7 Error scatter MIPR categorized in motion direction, shallow and deep water

Another observation can be made by analysing the directional split error scatters with the data points categorized by the direction of the heave velocity [Figure 4-7]. From these error scatters it can be confirmed that the highest strain peaks are corresponding to a negative (downward) heave motion as stated in previously in Section 3.2. These figures also confirm that the difference in behaviour is less extreme for the shallow water case.

4.1.4. *Results MIPR DNV buckling check*

The results for the MIPR method for buckling check prediction are conducted with the same method used for the strain prediction. An overview of the results of the MIPR method are shown in Table 4-7, Figures 4-8(a-c) and Figures 4-9(a-e). The mean and standard deviation heave acceleration at the stinger tip are presented as these are used for dividing the corresponding in- and outputs, as is described in Section 3.2.

General parameters		**Case 1**	**Case 2**	**Case 3**	**Case 4**	**Case 5**	**Case 6**	**Case 7**	**Case 8**
Water Depth	[m]	150	280	450	650	650	1000	1496	2000
Pipeline section	[-]	A				B			
Static case parameters									
Top Tension	[kN]	299	400	483	712	991	1499	2200	2955
Von Mises Strain	[%]	0.0793	0.0776	0.0756	0.0591	0.0769	0.0659	0.0761	0.0935
Regression parameters									
Input Variables		Surge velocity X_2, Surge acceleration X_3 Heave velocity X_8 Heave acceleration X_9		Heave velocity X_8 Heave acceleration X_9					
μ heave acceleration	[m/s^2]	0.5749	0.6610	0.6359	0.7049	0.7222	0.6946	0.6921	0.7344
σ heave acceleration	[m/s^2]	0.3519	0.3754	0.4265	0.4235	0.4344	0.4113	0.3866	0.3898
RMSE MIPR	[-]	0.0038	0.0039	0.0039	0.0027	0.0042	0.0032	0.0031	0.0029

Table 4-7 Results MIPR DNV code check error scatters

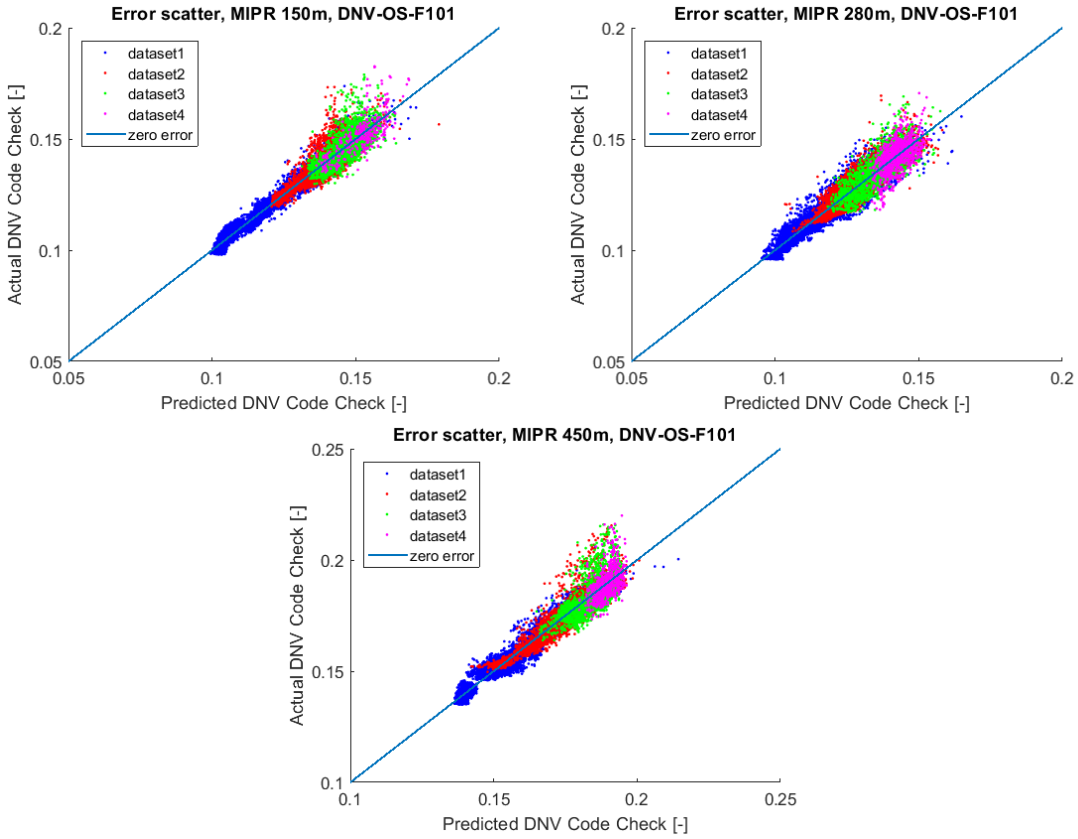

Figure 4-8 a–c Error scatter MIPR for case 1-3

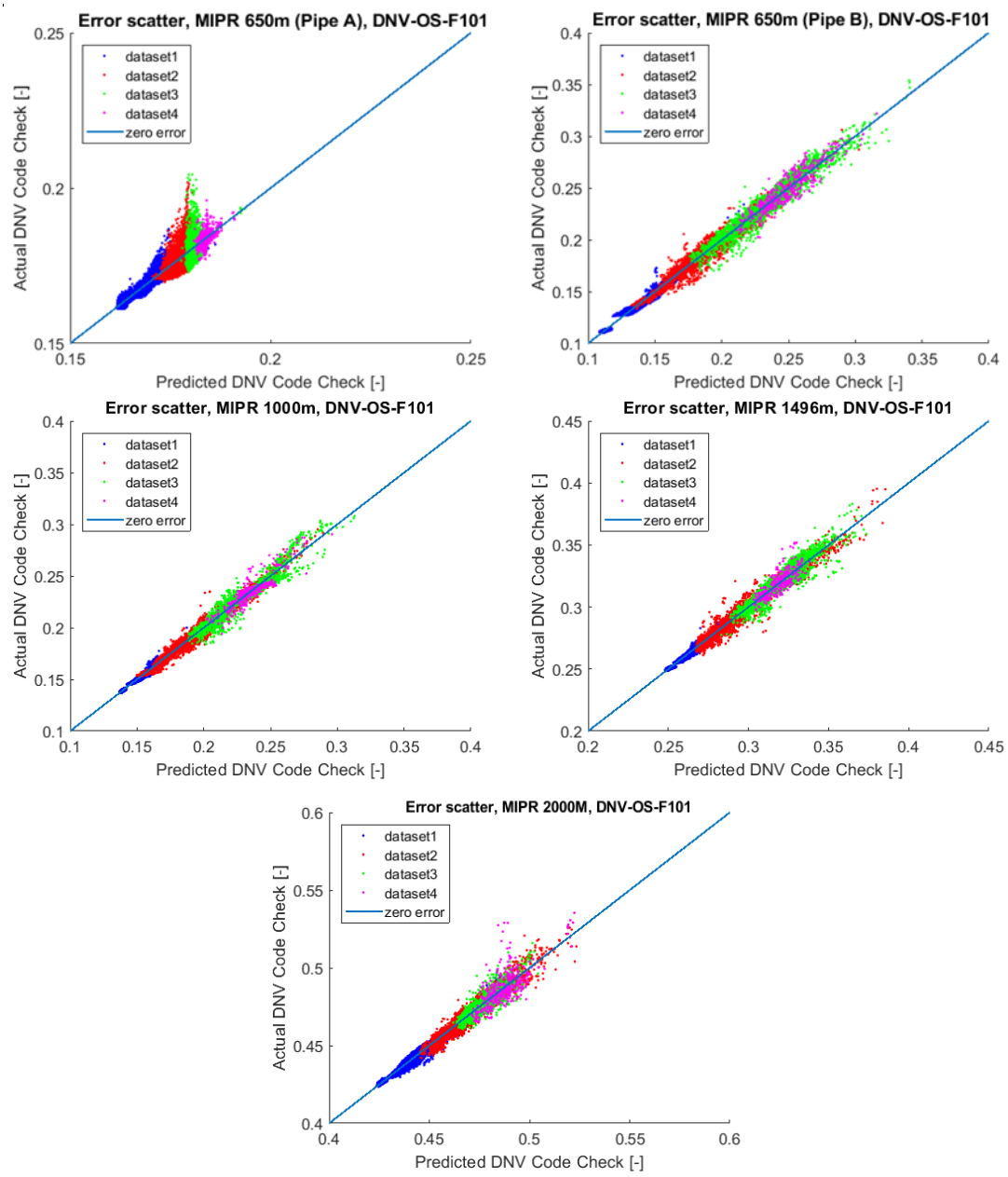

Figure 4-9 a–e Error scatter MIPR for case 4-8

The results of the error scatters of the DNV code check predictions are similar to the results of the Von Mises strain prediction in terms of the overall shape of the error scatters. The buckling check is dependent on the design moment and the axial force acting on the pipeline.

The pipe properties are kept to a minimum to minimize the amount of different variables and to get a better idea the effect vessel motions have on the strain and DNV code check.

The error scatters presented in Figure 4-9a and Figure 4-9b show the difference in pipeline motion behaviour due to the difference in pipeline properties. Just like the strain prediction, the case simulated with the B pipeline has a larger range between values of the buckling check than the case simulated with the A pipeline.

The error scatter of the case of 650m water depth and pipeline A shows an interesting trend: A non-linear error occurs between the predicted code check values of 0.17 and 0.19, like the example in Figure 3-1. It is notable that this is not visible in the error scatter of the strain prediction of the same case which is shown in Figure 4-6a. However, the reason why this error scatter stands out might be the effect of the scaling of the axis. This case has a relative low code check range which is why this error scatter is more enlarged than other cases.

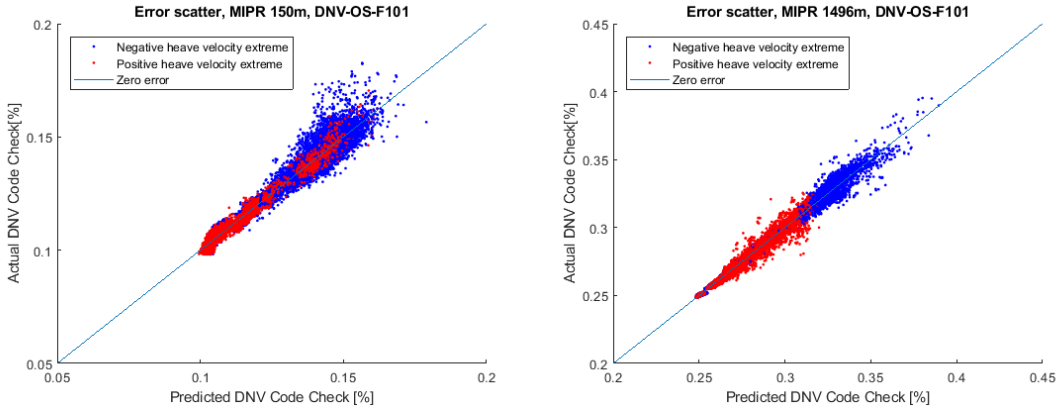

Figure 4-10 Error scatter MIPR categorized in motion direction, shallow & deep water

Figure 4-10 depicts the error scatter of the shallow water and deep water case with the data points categorized by the direction of the heave velocity. From these error scatters it can be concluded that the highest DNV code check peaks are corresponding to a negative (downward) heave motion just like the strain prediction.

4.2. Fatigue Damage

Unlike the statistical predictions for the DNV buckling check and the Von Mises strain, the fatigue damage predictions are analysed for a shallow water and a deep water case of 150m and 1496m water depth. The statistical fatigue damage prediction is constructed using the MIR method described in Section 3.1.

4.2.1. Motion Input

As described in Section 3.3.3, integrated motion values per motion cycle are used as an input to predict the fatigue damage. The three motion components under consideration are:

- Displacement
- Velocity
- Acceleration

These motions are presented for the most influential motion: heave at the stinger tip. The corresponding inputs and outputs scatter plots are presented along with the resulting prediction curves in Figure 4-11(a-f). The left column of the figures presents the shallow water case results and the right column presents the deep water case results. The regression curve is shown in red and the formula for each curve is given in Table 4-8 and Table 4-9.

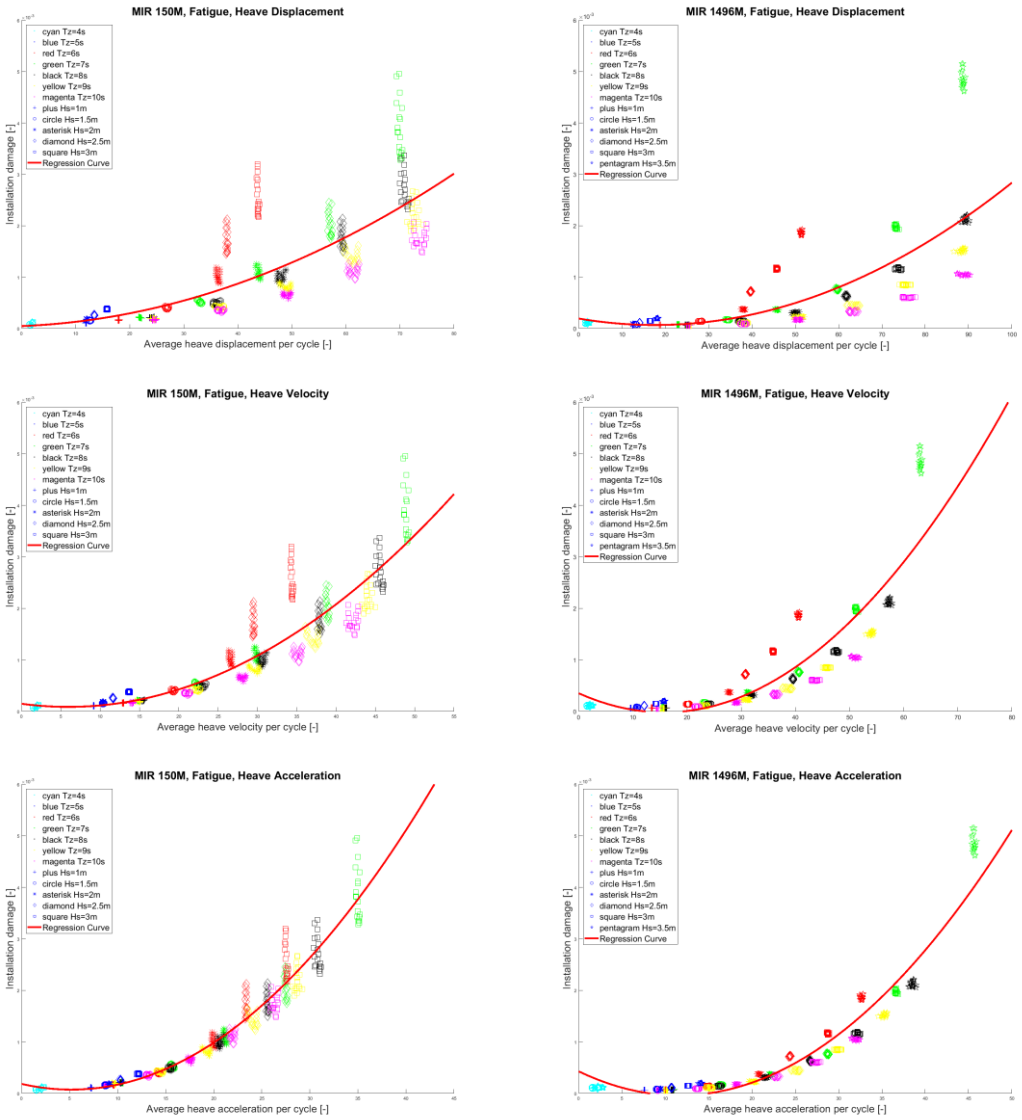

Figure 4-11a-f Input / Output scatter plots with resulting prediction curve heave displacement, velocity and acceleration, shallow & deep water

	Stinger tip motions 150m	Stinger tip motions 150m	Stinger tip motions 150m
Input Variables	Heave displacement X_7	Heave velocity X_8	Heave acceleration X_9
Regression curve formula	$Y_{predict} = 4.113 * 10^{-7} {X_7}^2 + 4.173 * 10^{-6} X_7 + 4.689 * 10^{-5}$	$Y_{predict} = 1.716 * 10^{-6} {X_8}^2 - 2.039 * 10^{-5} X_8 + 1.476 * 10^{-4}$	$Y_{predict} = 4.153 * 10^{-6} {X_9}^2 - 4.303 * 10^{-5} X_9 + 1.481 * 10^{-4}$
Measurement	Integrated motion per cycle	Integrated motion per cycle	Integrated motion per cycle
RMSE	5.185e-04	3.371e-04	1.886e-04

Table 4-8 Results MIR heave motions shallow water

	Stinger tip motions 1496m	Stinger tip motions 1496m	Stinger tip motions 1496m
Input Variables	Heave displacement X_7	Heave velocity X_8	Heave acceleration X_9
Regression curve formula	$Y_{predict} = 4.080 * 10^{-7} {X_7}^2 - 1.436 * 10^{-5} X_7 + 1.939 * 10^{-4}$	$Y_{predict} = 1.492 * 10^{-6} {X_8}^2 - 4.708 * 10^{-5} X_8 + 3.520 * 10^{-4}$	$Y_{predict} = 3.490 * 10^{-6} {X_9}^2 - 8.080 * 10^{-5} X_9 + 4.278 * 10^{-4}$
Measurement	Integrated motion per cycle	Integrated motion per cycle	Integrated motion per cycle
RMSE	5.788e-04	3.865e-04	2.259e-04

Table 4-9 Results MIR heave motion deep water

Shallow water

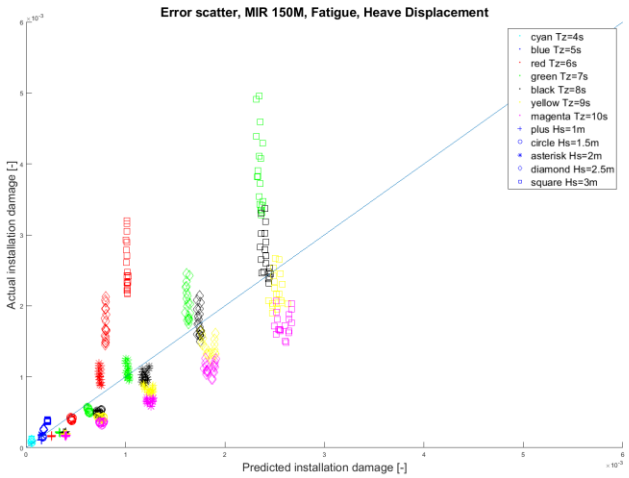

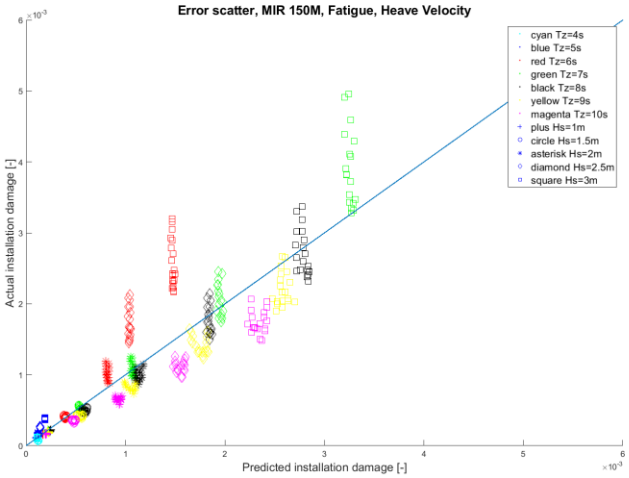

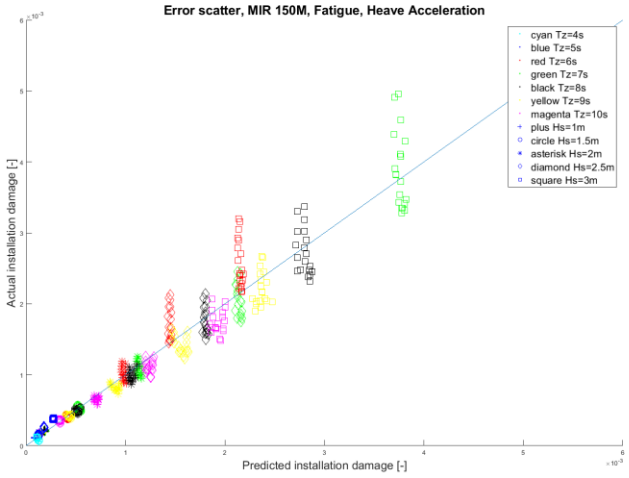

Figure 4-12a-c Error scatters MIR heave motions shallow water

Deep Water

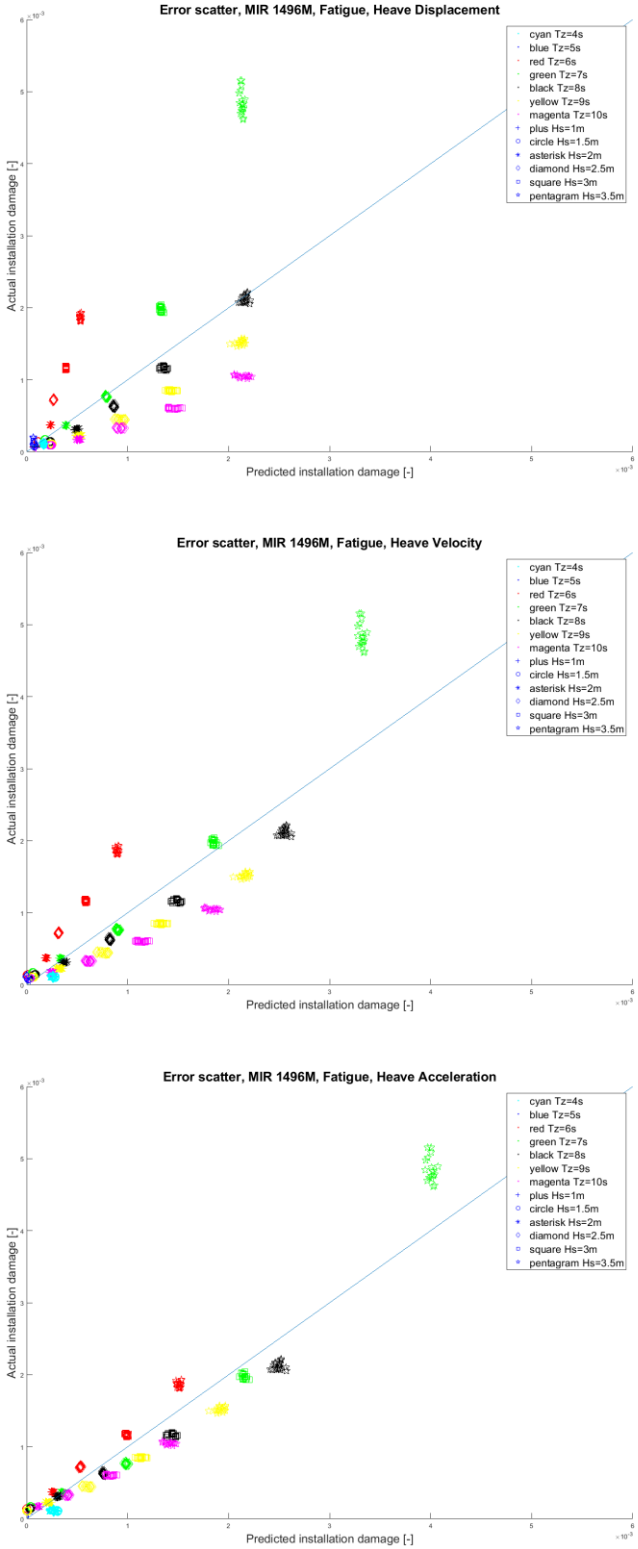

Figure 4-13a-c Error scatters MIR heave motions deep water

The error scatters that result from these regressions is shown in Figures 4-12(a-c) and Figures 4-13(a-c). The second order polynomial regression curve may seem illogical since the output will not converge to zero as the input becomes zero. This is particularly visible in Figure 4-11f. One might suggest an exponential curve based on the scatter plots presented previously. However, using a curve that represents sums of exponentials [Equation 4.1] for a multiple input regression is ill conditioned when the term b_i is unknown and N is larger than two (Kaufmann, 2003).

$$y = \sum_{i=1}^{N} a_i e^{b_i x_i} \tag{4.1}$$

This problem is also described by Acton (1990) in a chapter entitled “What not to compute”. For this reason the regression will be performed by a second order polynomial curve instead of an exponential curve.

A phenomenon that is most apparent when analysing the error scatters using the stinger heave displacement as input [Figure 4-12a and Figure 4-13a], is the fact that the sea states with a wave period (Tz) of four or five seconds, cyan or blue respectively, have little influence on both the stinger tip motions and the fatigue installation damage as they are located at the lower left corner of the error scatters., they will not be analysed for future fatigue predictions.

To account for the fact that the lower strains will negatively influence the fatigue predictions and these sea states have so little influence on the fatigue installation damage for higher installation damages, sea states with a T_z of four and five seconds will be removed from the regression data, coloured cyan and blue respectively.

There are a lot of observations that can be made when comparing the error scatters of the fatigue installation damage prediction for the different motion components of the most influential motion; heave. One thing that stands out immediately when comparing the displacement, velocity and the acceleration of the stinger tip heave, is that the data points are grouped together. This is the case for shallow water and deep water. These groups consist of the 19 different incoming wave angles from 0 up to 180 degrees per wave height (Hs) and wave period (Tz).

For the shallow water case, the different incoming wave angles are grouped in the shape of vertical columns. This is due to the fact that the actual installation damage does change with different incoming wave angles but the predicted installation damage does not. The predictions are based on one input parameter for these error scatters and that is heave displacement, velocity or acceleration. This indicates that the heave motion of the stinger is not significantly influenced by the changing incoming wave angle. This is confirmed by analysing Figure 4-14(a-c). These figures present the average acceleration motion per cycle for different incoming wave angles.

The other wave periods have their own peculiarities as the fatigue installation damage that result from sea states with a six second period are constantly underestimated. Also, the installation damages that result from a ten second wave period are constantly overestimated. This the most apparent for the error scatter with the heave displacement used as input for both shallow and deep [Figure 4-12a and Figure 4-13a]. This phenomenon is much less apparent when considering the heave acceleration of the stinger tip instead of the displacement.

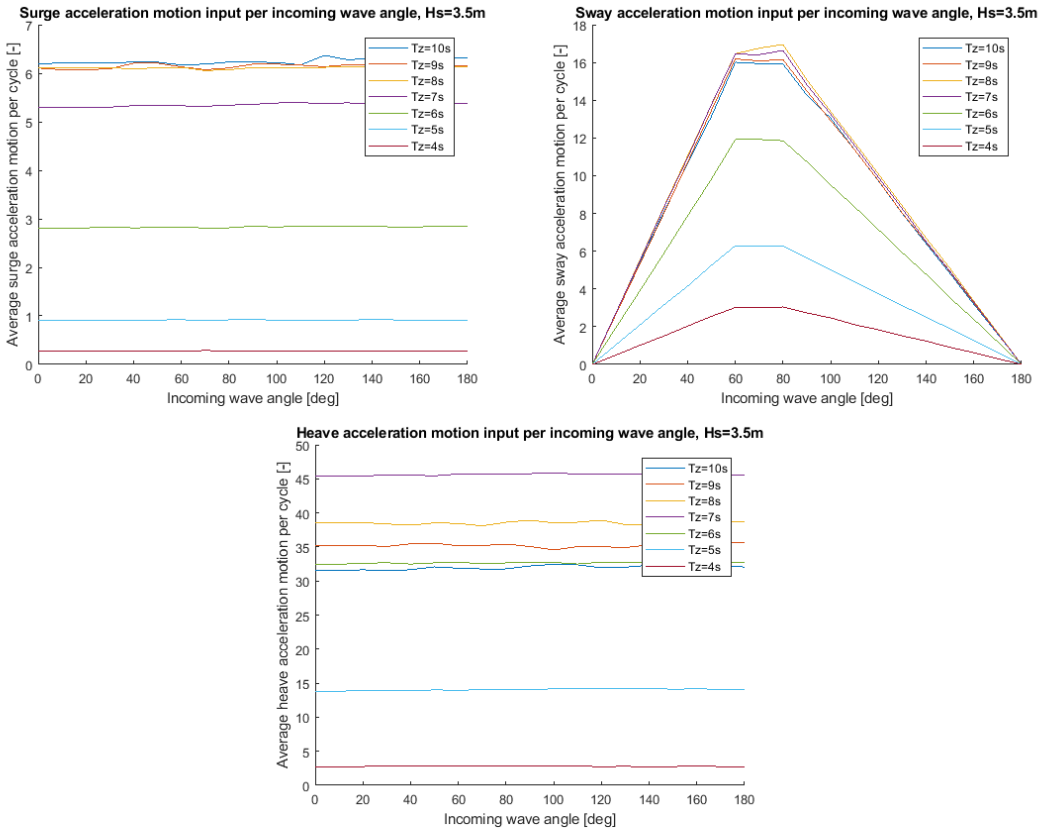

Figure 4-14a-c Average motion values per cycle for different incoming wave angels

This phenomenon suggest that the acceleration is the best input parameter of the considered motions. Displacement shows the information of the total distance that is traversed by the stinger but not at which rate. Acceleration contains the most information regarding 'change of motion'. This rate of 'change of motion' is important when considering the Von Mises stress ranges acting on the pipeline. This is visible in the error scatters figures as the groups of data points using acceleration [Figure 4-12c and Figure 4-13c] are located closer to the "zero error" line.

This is only visible for the data points with a higher fatigue installation damage as the data points located in the lower-left corner of the error scatter are located so close to each other that one can't make any conclusions based on visual inspection of the error scatters. The higher installation damages are the most critical to the integrity of the pipeline. Based on the visual comparison of the error scatters, the acceleration results in the least error for the higher installation damages. Therefore the fatigue installation damage will be predicted with the acceleration of the motions.

For the deep water case, the actual installation damages are almost identical for different incoming wave angles. This means that sway becomes relatively less influential for deeper water depths. The sway motion is the motion that is largely influenced by the changing incoming wave angle, as can be observed in Figure 4-14b. This observation supports the conclusion that the heave motion of the stinger becomes more dominant with regard to fatigue installation damage with increasing water depth and a more vertical lift-off angle. This is already suggested in the dynamic isolated motion analysis discussed in Section 2.6. The aforementioned analysis concluded that the heave motion is more influential in deep water, with regard to strain, due to the orientation and length of the suspended pipeline. It would only stand to reason this is also the case for the fatigue damage,

as the damage is calculated with the Von Mises stress range which in turn is linearly derived from the Von Mises strain.

Last but not least, the heave acceleration seems to have the highest input value for a T_z of seven seconds. The surge acceleration has the highest input value for a T_z of ten seconds, as can be observed in Figure 4-14(a-c). The error scatters clearly indicate that the waves with a period of seven seconds results in the highest installation damage. This indicates that the stinger heave is the most influential stinger motion.

4.2.2. Motion Input Combination

Now that it is determined that the heave acceleration at the stinger tip is the most influential motion for fatigue damage, it is clear that the heave acceleration should be one of the motion inputs for the multiple input regression (MIR). It is essential to determine further which combination of motions is the most relevant to predict the fatigue installation damage. There are three combinations under consideration:

- Heave & surge
- Heave & surge
- Heave, sway & surge

Because the motions are measured at the stinger tip, the rotational motions at the CoG are included in the translational motions at the stinger tip. This means that the input motion combination of heave, sway & surge at the stinger tip includes all vessel motions. The error scatters of the various motion combinations are shown in Figure 4-15(a-c) and Figure 4-16(a-c) for shallow water and deep water and the corresponding parameters are listed in Table 4-10 and Table 4-11.

	Stinger tip motions 150m	Stinger tip motions 150m	Stinger tip motions 150m
Input Variables	Surge acceleration X_3, Heave acceleration X_9	Sway acceleration X_6, Heave acceleration X_9	Surge acceleration X_3, Sway acceleration X_6, Heave acceleration X_9
Regression curve formula	$Y_{predict} = 6.297 * 10^{-5}{X_3}^2 + 7.155 * 10^{-6}{X_9}^2 - 2.957 * 10^{-6}X_3X_9 + 8.314 * 10^{-5}X_3 - 5.460 * 10^{-5}X_9 + 1.736 * 10^{-4}$	$Y_{predict} = 3.451 * 10^{-6}{X_6}^2 + 4.903 * 10^{-6}{X_9}^2 - 5.217 * 10^{-6}X_6X_9 + 3.530 * 10^{-5}X_6 - 4.505 * 10^{-5}X_9 + 1.481 * 10^{-4}$	$Y_{predict} = 5.867 * 10^{-5}{X_3}^2 + 3.970 * 10^{-6}{X_6}^2 + 7.842 * 10^{-6}{X_9}^2 + 1.232 * 10^{-5}X_3X_6 - 2.844 * 10^{-5}X_3X_9 - 7.205 * 10^{-6}X_6X_9 + 4.806 * 10^{-5}X_3 + 3.255 * 10^{-5}X_6 - 5.183 * 10^{-5}X_9 + 1.43 * 10^{-4}$
Measurement	Average motion per cycle	Average motion per cycle	Average motion per cycle
RMSE	1.839-04	1.138e-04	5.380e-05

Table 4-10 Results fatigue MIR shallow water

	Stinger Tip Motions 1496m	Stinger tip motions 1496m	Stinger tip motions 1496m
Input Variables	Surge acceleration X_3, Heave acceleration X_9	Sway acceleration X_6, Heave acceleration X_9	Surge acceleration X_3, Sway acceleration X_6, Heave acceleration X_9
Regression curve formula	$Y_{predict} = 2.406 * 10^{-5}{X_3}^2 + 5.871 * 10^{-6}{X_9}^2 - 2.235 * 10^{-5}X_3X_9 + 2.268 * 10^{-4}X_3 - 1.028 * 10^{-4}X_9 + 3.846 * 10^{-4}$	$Y_{predict} = -2.9738 * 10^{-6}{X_6}^2 + 3.529 * 10^{-6}{X_9}^2 + 4.049 * 10^{-7}X_6X_9 + 1.391 * 10^{-5}X_6 - 8.102 * 10^{-5}X_9 + 4.083 * 10^{-4}$	$Y_{predict} = 2.290 * 10^{-5}{X_3}^2 - 3.087 * 10^{-8}{X_6}^2 + 5.958 * 10^{-6}{X_9}^2 + 3.864 * 10^{-6}X_3X_6 - 2.234 * 10^{-5}X_3X_9 - 9.482 * 10^{-7}X_6X_9 + 2.154 * 10^{-4}X_3 + 4.568 * 10^{-6}X_6 - 1.012 * 10^{-4}X_9 + 3.771 * 10^{-4}$
Measurement	Average motion per cycle	Average motion per cycle	Average motion per cycle
RMSE	1.116e-04	2.022e-04	1.042e-04

Table 4-11 Results fatigue MIR deep water

Shallow water

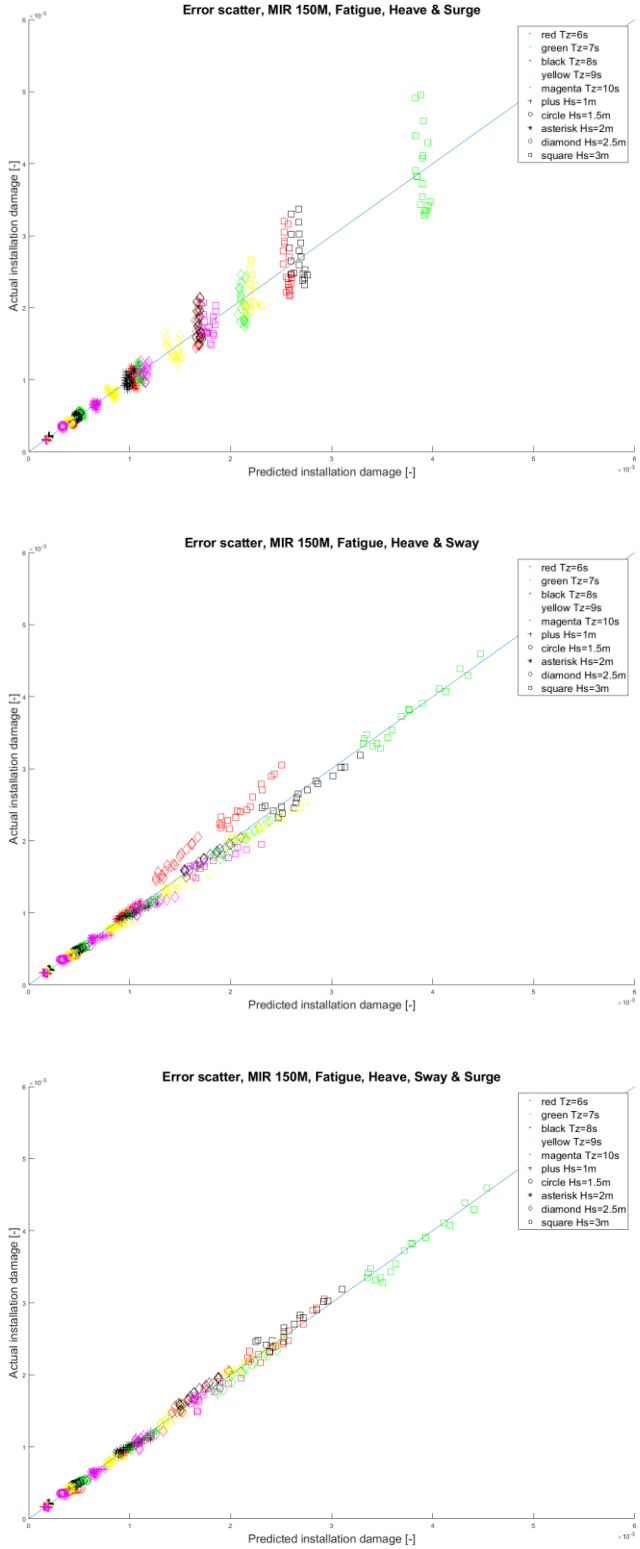

Figure 4-15a-c Error scatter MIR motion input combination shallow water

Deep water

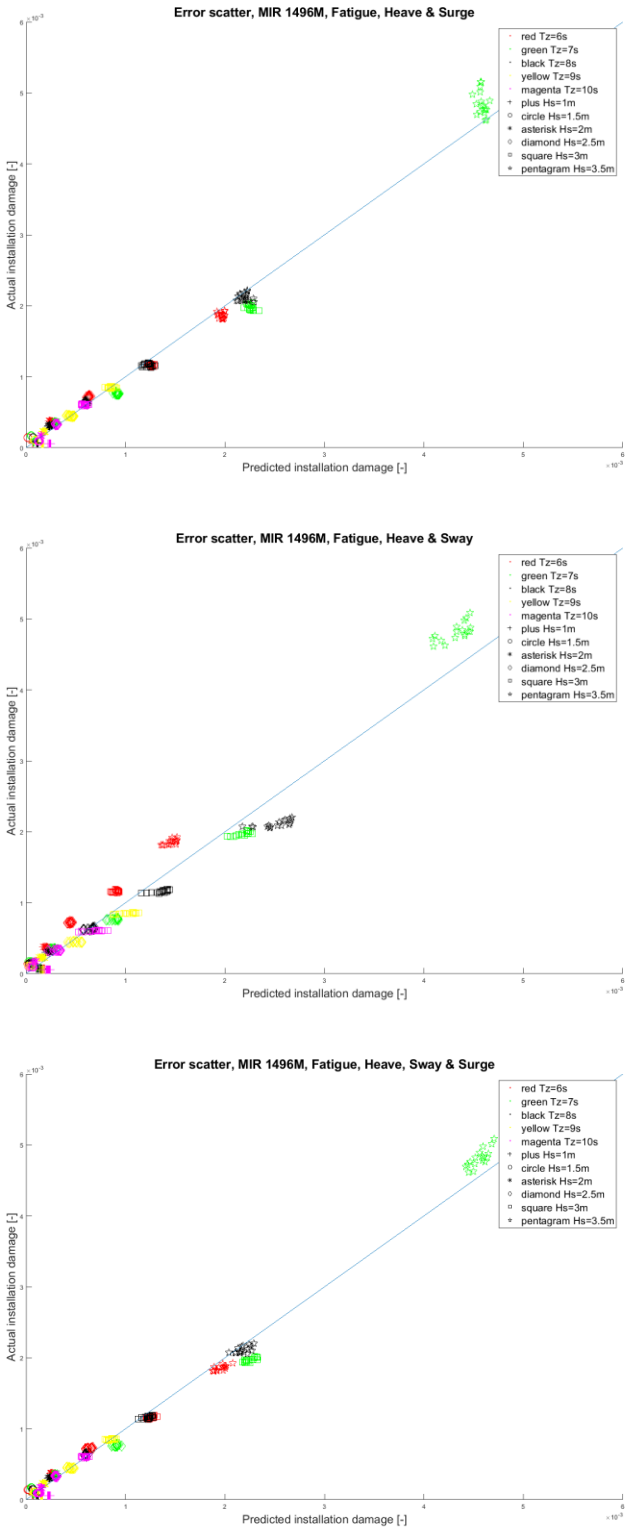

Figure 4-16a-c Error scatter MIR motion input combination deep water

When observing the shallow water case results, it becomes clear that the vertical columns of data points are ‘corrected’ by including the sway motion. This is logical as the sway motion is the only motion that is significantly influenced by the incoming wave angle as depicted in Figure 4-14b. This means the difference in installation damage due to the difference in incoming wave angle can only be predicted using the sway motion. However, the shallow and deep water error scatter with sway and heave as inputs still indicates an underestimation of the data groups that result from a six second wave period (red) and a marginal overestimation of the data groups that result from a ten second wave period (magenta). This over- and underestimation is ‘corrected’ by including the surge motion. Figure 4-14a illustrates why this is the case. The average surge motion per cycle increases for increasing wave periods and is not influenced by the incoming wave angle. Surge is therefore more susceptible to waves with a lower frequency. This means the fatigue installation damage prediction will be the most accurate by including the heave, sway and surge motion at the stinger tip. As mentioned before these motions at the stinger tip effectively represents all vessel motions. This is logical when considering the nature of fatigue damage; significant damage resulting from a large amount of accumulated small damages. As each vessel motion results in a (however small) damage, considering all vessel motions results in the best prediction for fatigue damage.

The deep water error scatters that consider heave & surge and heave, sway & surge as an input [Figure 4-16a and Figure 4-16c], are almost identical. Thereby raising the question if the sway motion is necessary as an input for the deep water case. Although the aforementioned error scatters are very similar, the prediction is different when one considers the group of data points in the top right corner (green pentagrams). The prediction for this group is visually improved by including the sway motion. This is the group of data points with the largest installation damage, so it is also the most crucial in terms of pipeline integrity. That means that the prediction of the fatigue installation damage for both shallow and deep water yields the most relevant results when heave, sway and surge motion at the stinger are all used as an input.

One should keep in mind that surge may have a larger influence on the fatigue prediction than in real life due to the fact that the tensioners are modelled to be ‘on the break’. Thereby no pipe is hauled-in or payed-out which has a surge compensating effect in real life. In reality, the horizontal motions are also compensated by a dynamic positioning system.

5. DISCUSSION & VALIDATION

This chapter starts with a discussion which is divided in two parts; a discussion on optimising the required simulated sea states and a more general discussion based on observations and conclusions made throughout the thesis. Subsequently, the regression methods for strain, buckling check and fatigue are validated with simulations based on the Nordstream II project.

5.1. Relevant sea states

This section will discuss the relevant sea state analysis along with a validation of the optimised sea states.

5.1.1. Reduction of sea states ranges

During this thesis numerous sea states have been simulated using a uni-directional JONSWAP spectrum. These sea states are assumed to excite all probable vessel motions during installation. The sea states that have been simulated are described in (Section 3.3) and consist of the following range of parameters:

- H_s: 1,1.5,2,…3.5 meters
- T_z: 4,5,6,…10 seconds
- θ: 0,10,20,…180 degrees

To increase efficiency during simulation and analysis, it would be preferable if a selection of these sea states could be used to yield similar results instead of the entire range of sea states given above. A shallow water and a deep water case are used to analyse which sea states can be left out whilst still yielding similar results with regard to the prediction.

Significant wave height H_s

The distributions of strain peaks are determined for different ranges of sea states. This analysis will determine if the 'optimised' range of sea states includes sufficient data to represent the entire range of strain peaks.

The sea state parameter that will be optimised first is the significant wave height (H_s). Sea states are simulated for the entire range of T_z and θ as previously described. Six different ranges of H_s are analysed. These will include a range of 3.5 meter, 3.0-3.5 meter, 2.5-3.5 meter, etc., for deep water. For shallow water the H_s range starts at 3.0 meters. These ranges are presented in Table 5-2 and Table 5-3.

The reason why the H_s range will start at a value of 3.5 meters, is because the highest strain peaks are the most crucial with regard to pipeline integrity. The highest strains will result from a sea state with the highest H_s and it is essential these higher strains are well represented.

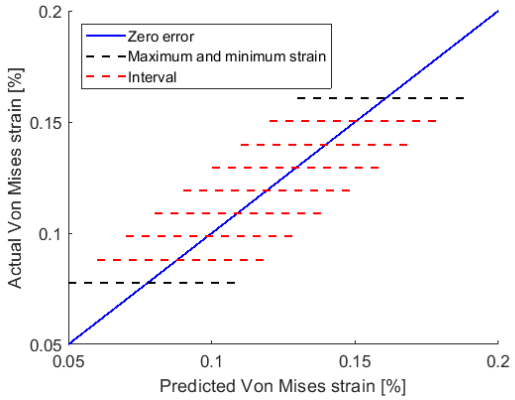

Figure 5-1 Example strain divided in sections

	Maximum strain peak [%]	Minimum strain peak [%]	Interval width [%]
Shallow water	0.1386	0.0858	0.0066
Deep water	0.1607	0.0777	0.0104

Table 5-1 Maximum/minimum strain peaks with interval width for shallow and deep water

The range of strain peaks is divided into eight equally spaced intervals as can be observed in Figure 5-1 and Table 5-1. The percentage of the number of data points that are simulated in these sections are analysed and listed in Table 5-2 and Table 5-3. The number of data points in each section represents the strain peak distributions for different sea states.

Shallow water	**Data points distribution**							
Strain value [%]	~ 0.086 - 0.092	~ 0.092 - 0.099	~ 0.099 - 0.106	~ 0.106 - 0.112	~ 0.112 - 0.118	~ 0.118 - 0.125	~ 0.125 - 0.132	~ 0.132 - 0.139
Total number of data points	2443	2517	3559	2482	2599	1382	245	49
Hs range [m]	**Interval 1**	**Interval 2**	**Interval 3**	**Interval 4**	**Interval 5**	**Interval 6**	**Interval 7**	**Interval 8**
3.0	8.1%	15.5%	12.2%	0.8%	30.2%	71.6%	91.8%	100%
2.5-3.0	29.3%	18.7%	24.8%	13.6%	79.8%	97.8%	100%	100%
2.0-3.0	53.0%	33.4%	27.5%	71.6%	99.3%	100%	100%	100%
1.5-3.0	77.2%	48.8%	65.5%	99.7%	100%	100%	100%	100%
1.0-3.0	100%	100%	100%	100%	100%	100%	100%	100%

Table 5-2 Data distribution over the strain range, shallow water

Deep water	**Data points distribution**							
Strain range [%]	~0.08-0.09	~0.09-0.10	~0.10-0.11	~0.11-0.12	~0.12-0.13	~0.13-0.14	~0.14-0.15	~0.15-0.16
Total number of data points	8127	2352	1424	1885	2112	648	141	21
Hs range [m]	**Interval 1**	**Interval 2**	**Interval 3**	**Interval 4**	**Interval 5**	**Interval 6**	**Interval 7**	**Interval 8**
3.5	7.6%	13.7%	0.0%	17.8%	47.6%	71.3%	79.4%	100%
3.0-3.5	17.7%	18.1%	12.1%	55.4%	87.2%	95.7%	96.5%	100%
2.5-3.5	28.7%	25.4%	65.0%	92.0%	99.5%	100%	100%	100%
2.0-3.5	40.2%	76.4%	98.3%	99.9%	100%	100%	100%	100%
1.5-3.5	66.9%	99.9%	100%	100%	100%	100%	100%	100%
1.0-3.5	100%	100%	100%	100%	100%	100%	100%	100%

Table 5-3 Data distribution over the strain range, deep water

It can be observed from Table 5-2 and Table 5-3 that the sea states with the highest H_s, for both deep and shallow water, results in strain peaks that are mostly located in the sections with the higher strain ranges. The inclusion of the mid H_s ranges adds data points in the middle and lower strain ranges. The inclusion of the lower H_s ranges adds data primarily in the lower strain ranges.
It becomes apparent from these tables that the sea states with a lower H_s can be removed from the prediction curve training data. For deep water, the total number of data points present in the lower strain region is relatively very large. This is the least interesting group in terms of regression, as the higher strain ranges determine the operational limit.
The analysis of the strain peak distribution concludes that limiting the H_s range of the simulated sea states is possible whilst still resulting in a sufficient amount of data distributed over the entire strain range. The range of H_s that is chosen to represent data in the entire strain range, based on the distributions of Table 5-2 and Table 5-3, is 2.5-3.5 meters for deep water and 2.5-3.0 meter for shallow water.

Wave period T_z

The incoming wave angles from 0 up to 180 degrees are simulated since it is assumed that these wave angles excite all probable vessel motions for a given H_s and T_z. An analysis is performed to observe maximum stinger motions used as an input for the MIPR method. This is done for different combinations of wave periods and incoming wave angles. The shallow water case makes use of the highest number of input motions and therefore the analysis is performed for the shallow water case. In Figures 5-2(a-d) and Figures 5-3(a-c), the maximum input and maximum strain values are presented for all incoming wave angles and a T_z ranging from four to ten seconds. H_s ranges from 2.5 to 3.0 meter as is determined in Section 5.1.1.

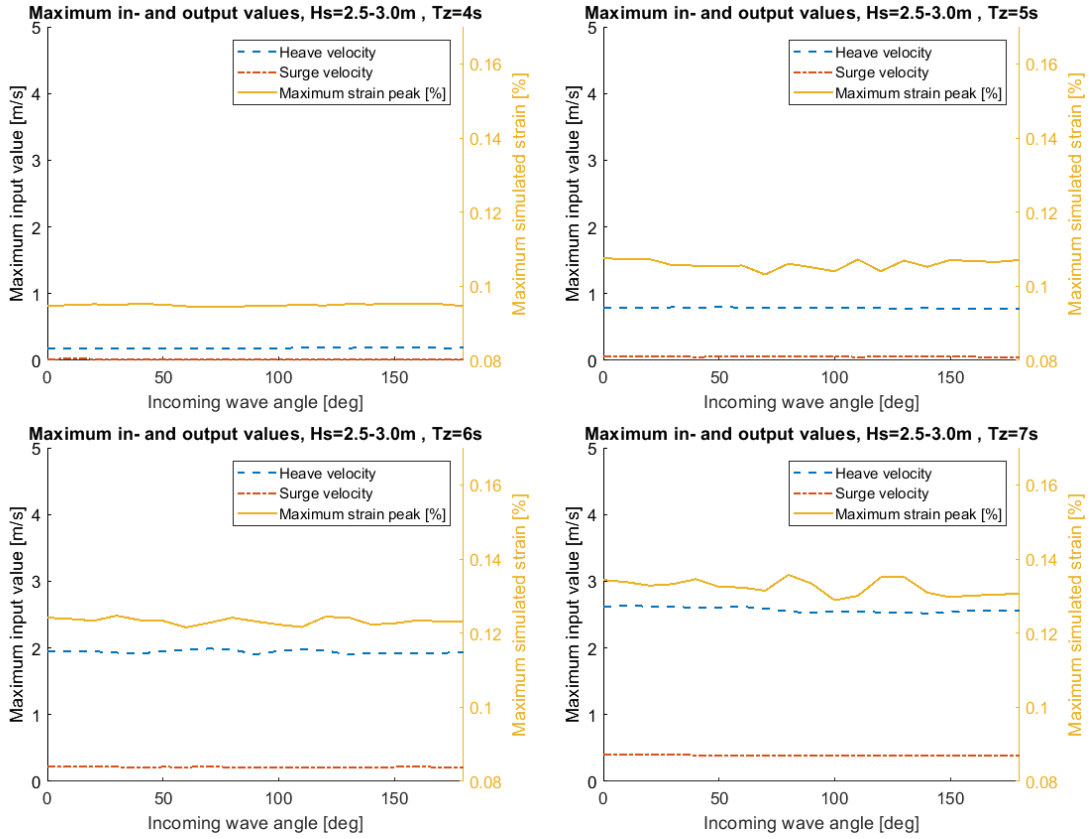

Figures 5-2a-d Maximum input and output values for varying Tz and θ

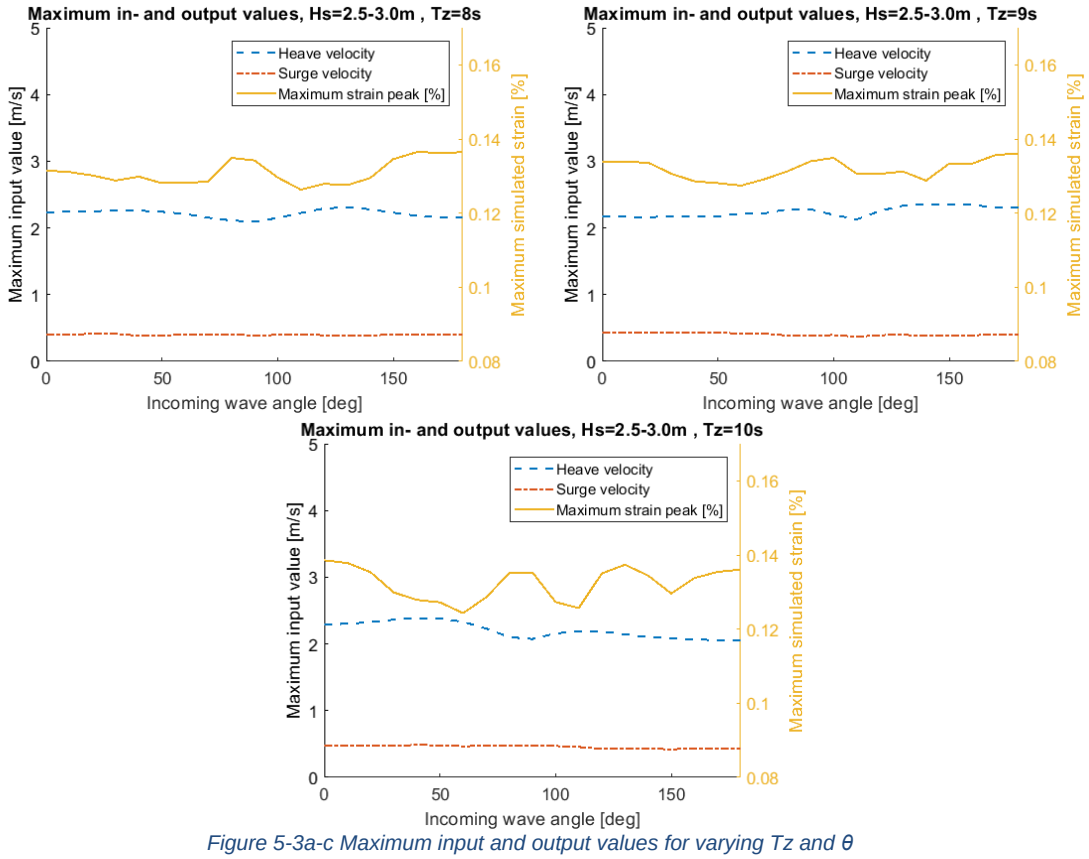

Figure 5-3a-c Maximum input and output values for varying Tz and θ

It can be concluded that the sea states with a wave period of four and five seconds have very low maximum in- and output values. This is why these wave periods can be excluded from the required sea state simulations as they do not result in in- and output values with a high significance. This is in accordance with conclusions made in Section 4.2, where the sea states with a wave period of four and five seconds are removed due to their insignificance which actually worsens the regression results.

Fatigue prediction

The selection of sea states determined in Section 5.1.2 has to be verified for the fatigue damage prediction. It is essential that the in- and outputs resulting from the selected sea states represent the required data to construct the fatigue damage predictions. The optimised range of sea states that are determined in Section 5.1.2 are:

Shallow water

- H_s: 2.5 and 3.0 meters
- T_z: 6,…10 seconds
- θ: 0,10,20,…180 degrees

Deep water

- H_s: 2.5, 3.0 and 3.5 meters
- T_z: 6,…10 seconds
- θ: 0,10,20,…180 degrees

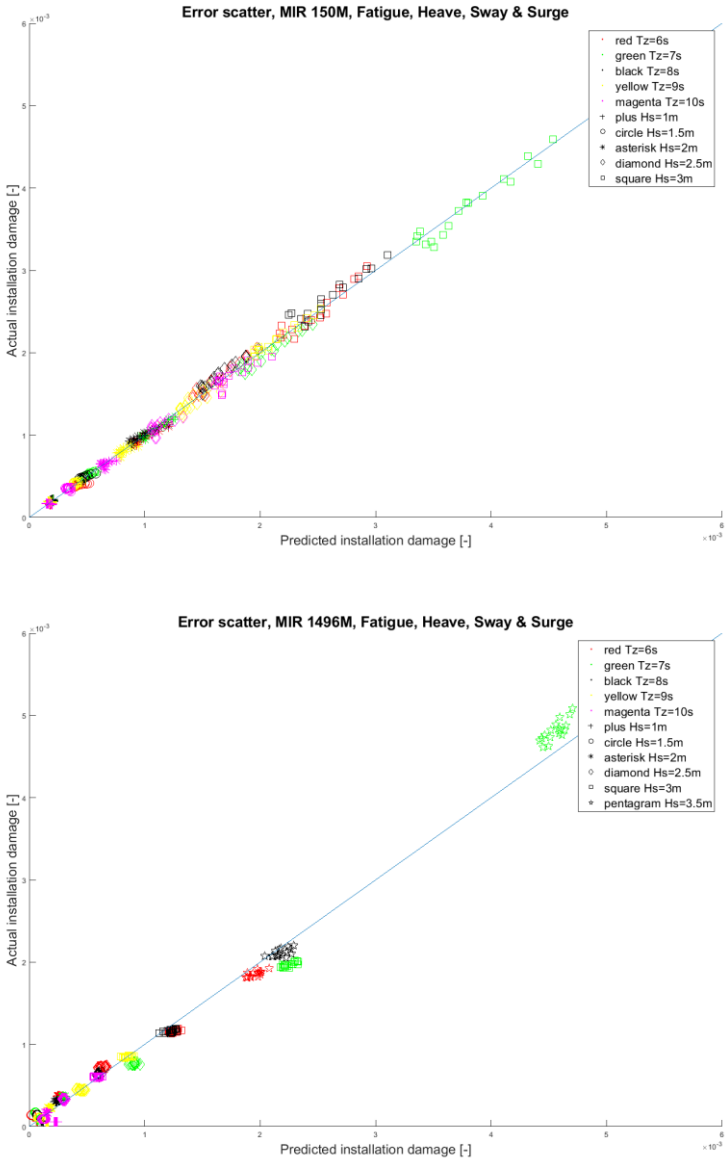

Figure 5-3a-b MIR error scatters fatigue damage, shallow and deep water

In Section 4.2.1 it was already determined that the four and five second wave period is irrelevant for constructing the fatigue prediction. By observing these scatters it can be concluded that fatigue damage resulting from a sea state with a Hs of one up to two meters can be removed as well as the error scatter plots for shallow and deep water [Figures 5-3a-b] is dominated by the data points resulting from sea states with a Hs that exceed the 2 meters. This is due to the fact that the data points, indicated with a plus, circle or asterisk symbol are located in the lower left corner which indicates these points result in a very low fatigue damage. This reduces the required number of simulations from 798 to 285 for deep water and from 665 to 160 simulations for shallow water.

5.1.2. Validation of reduced sea states

The validation presented could be described as a quality analysis of the constructed prediction curves. There is no empirical data available on the strains acting inside of an actual pipeline during installation. That is why the validation of the prediction curves is done with several different validation simulations. A uni-directional JONSWAP spectrum is simulated to validate the shallow water and the deep water optimised sea states for the buckling check and fatigue.

Two sets of prediction curves are constructed:

- Prediction curves constructed with all sea states
- Prediction curves constructed with the optimised sea states presented in Section 5.1

The sea states that are simulated to validate the optimised sea states, are using a uni-directional JONSWAP spectrum and do not belong to the simulations which are used to construct the buckling check and fatigue predictions. Therefore, these simulations can be used to test the constructed prediction curves for shallow and deep water. The sea states that are simulated for deep and shallow water are the following:

- H_s: 2.5,…3.5 meters (for deep water)
- H_s: 2.5,…3 meters (for shallow water)
- T_z: 6, 7,… 10 seconds
- θ: 35, 55, 85, 115, 145 degrees

The range of H_s and T_z are chosen based on the sea state optimisation described in Section 5.1. The incoming wave angles are chosen as samples to represent the different incoming wave angle range from 0-180 degrees.

The highest 5% of strain peaks are chosen for the strain and buckling check prediction validation.

The error between the simulated 'actual' buckling check and fatigue damage and the predicted output is quantified by an error percentage. The error percentage is determined with the following formula:

$$Error\ percentage = \left(\frac{Y_{actual} - Y_{predicted}}{Y_{actual}}\right) * 100 \qquad (5.1)$$

The results for the validation with uni-directional JONSWAP spectrum simulation are presented in Table 5-4 – Table 5-7 and Figure 5-4 – Figure 5-7.

DNV-OS-F101 buckling check prediction, Shallow water

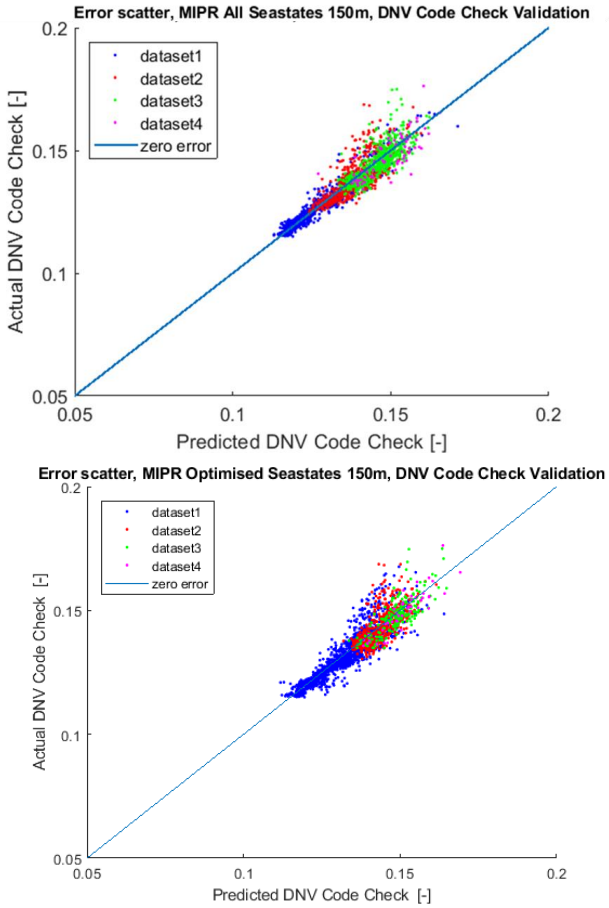

Figure 5-4 Validation data applied to buckling check prediction curves resulting from all and reduced sea states, shallow water

General parameters		**Shallow water DNV Code Check All sea states**				**Shallow water DNV Code Check Optimised sea states**			
Water Depth [m]		150							
Pipeline section [-]		A							
Regression parameters									
Input Variables		Surge velocity X_2 Surge acceleration X_3 Heave velocity X_8 Heave acceleration X_9							
Error type		**Data points**	**Mean error [%]**	**Maximum error [%]**	**Minimum error [%]**	**Data points**	**Mean error [%]**	**Maximum error [%]**	**Minimum error [%]**
Dataset 1	Sub-dataset 1	685	1.5690	9.9792	-7.0936	1199	2.1838	11.7478	-11.1023
	Sub-dataset 2	49	1.4759	3.9967	-2.9156	77	4.1214	8.4356	-10.6940
Dataset 2	Sub-dataset 1	715	2.4925	16.1162	-8.2783	482	2.3859	15.0983	-7.7748
	Sub-dataset 2	14	2.1415	5.6370	-3.8160	56	3.4025	11.8061	-6.7958
Dataset 3	Sub-dataset 1	438	2.3816	13.9142	-7.8312	167	2.4376	12.5240	-7.4651
	Sub-dataset 2	76	1.6292	5.3733	-5.1480	23	2.0801	4.5528	-4.2978
Dataset 4	Sub-dataset 1	47	3.3271	8.9917	-11.5094	37	2.4089	7.1288	-6.6174
	Sub-dataset 2	22	2.6306	9.5842	-5.3110	5	1.2233	0.0057	-2.1345
Total		2046	2.1214	16.1162	-11.5094	2046	2.3007	15.0983	-11.1023

Table 5-4 Results validation DNV buckling check prediction, shallow water

DNV-OS-F101 buckling check prediction, Deep water

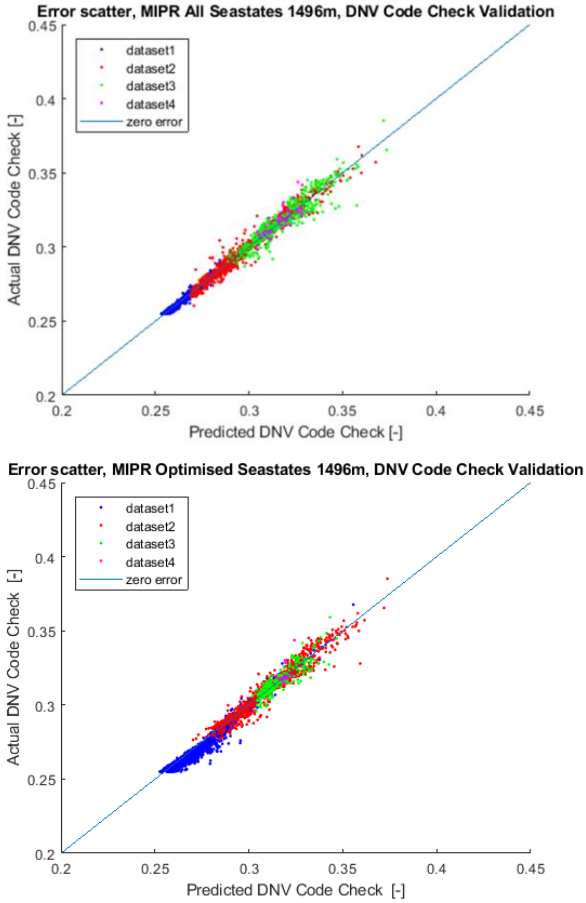

Figure 5-5 Validation data applied to buckling check prediction curves resulting from all and reduced sea states, deep water

General parameters		**Deep water DNV Code Check All sea states**				**Deep water DNV Code Check Optimised sea states**			
Water Depth [m]		1496							
Pipeline section [-]		B							
Regression parameters									
Input Variables		Heave velocity X_8 Heave acceleration X_9							
Error type		**Data points**	**Mean error [%]**	**Maximum error [%]**	**Minimum error [%]**	**Data points**	**Mean error [%]**	**Maximum error [%]**	**Minimum error [%]**
Dataset 1	Sub-dataset 1	452	0.4289	2.2846	-2.3167	777	0.7548	3.2783	-2.9770
	Sub-dataset 2	456	0.3304	1.8798	-2.4307	580	1.7200	2.7673	-7.6793
Dataset 2	Sub-dataset 1	708	0.7032	3.0370	-4.1946	701	0.8302	3.8485	-9.5547
	Sub-dataset 2	240	1.2046	6.6062	-4.6879	233	1.4580	4.8954	-6.0562
Dataset 3	Sub-dataset 1	445	0.9646	4.0191	-9.0351	168	1.0865	4.4390	-4.6938
	Sub-dataset 2	166	1.2887	2.9908	-7.0950	58	1.0637	2.4801	-3.4940
Dataset 4	Sub-dataset 1	58	1.1539	5.1271	-2.4339	14	1.1775	5.6771	-1.4444
	Sub-dataset 2	9	0.9485	1.8576	-1.9062	3	1.0238	2.4865	-0.8274
Total		2534	0.7301	6.6062	-9.0351	2534	1.1673	5.6771	-9.5547

Table 5-5 Results validation DNV buckling check prediction, deep water

Fatigue Damage prediction, Shallow water

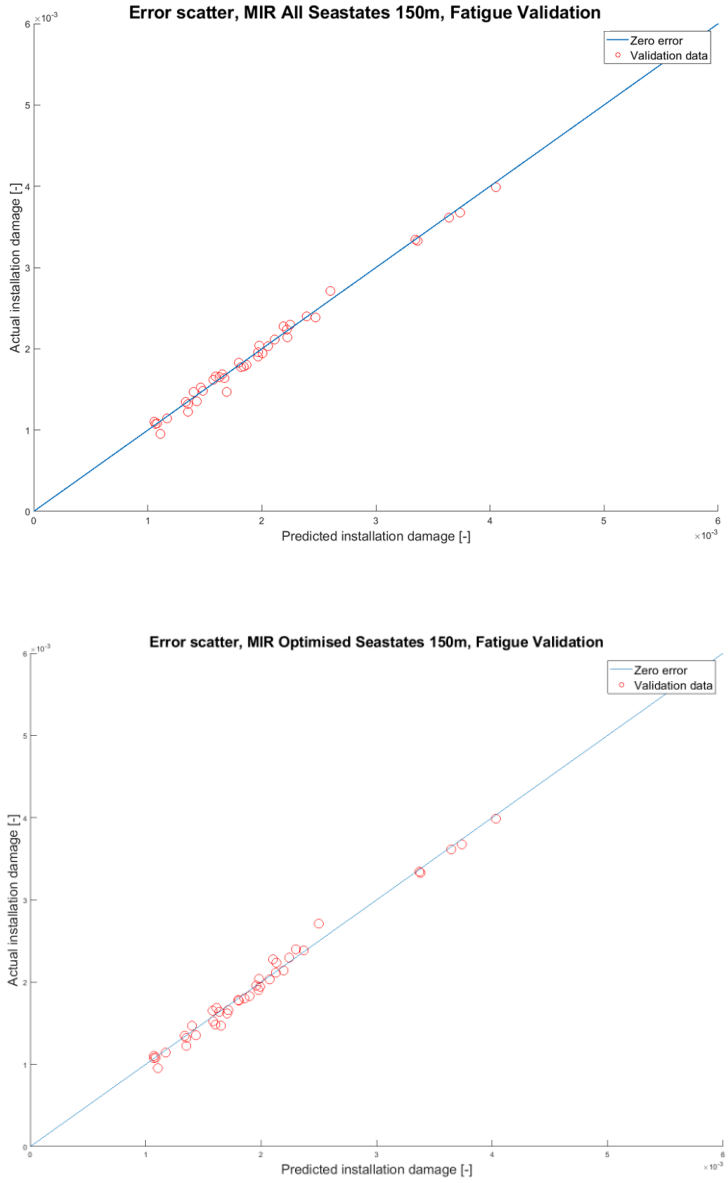

Figure 5-6 Validation data applied to fatigue prediction curves resulting from all and reduced sea states, shallow water

General parameters		**Shallow water Fatigue All sea states**			**Shallow water Fatigue Optimised sea states**			
Water Depth	[m]	150						
Pipeline section	[-]	A						
Regression parameters								
Input Variables		Surge acceleration X_3, Sway acceleration X_6, Heave acceleration X_9						
Error type		**Data points**	**Mean error [%]**	**Maximum error [%]**	**Minimum error [%]**	**Data points**	**Mean error [%]**	**Maximum error [%]**	**Minimum error [%]**
Total		50	3.1315	4.7449	-16.3237	50	3.6491	7.8185	-16.0941

Table 5-6 Results validation fatigue predictions, shallow water

Fatigue Damage prediction, Deep water

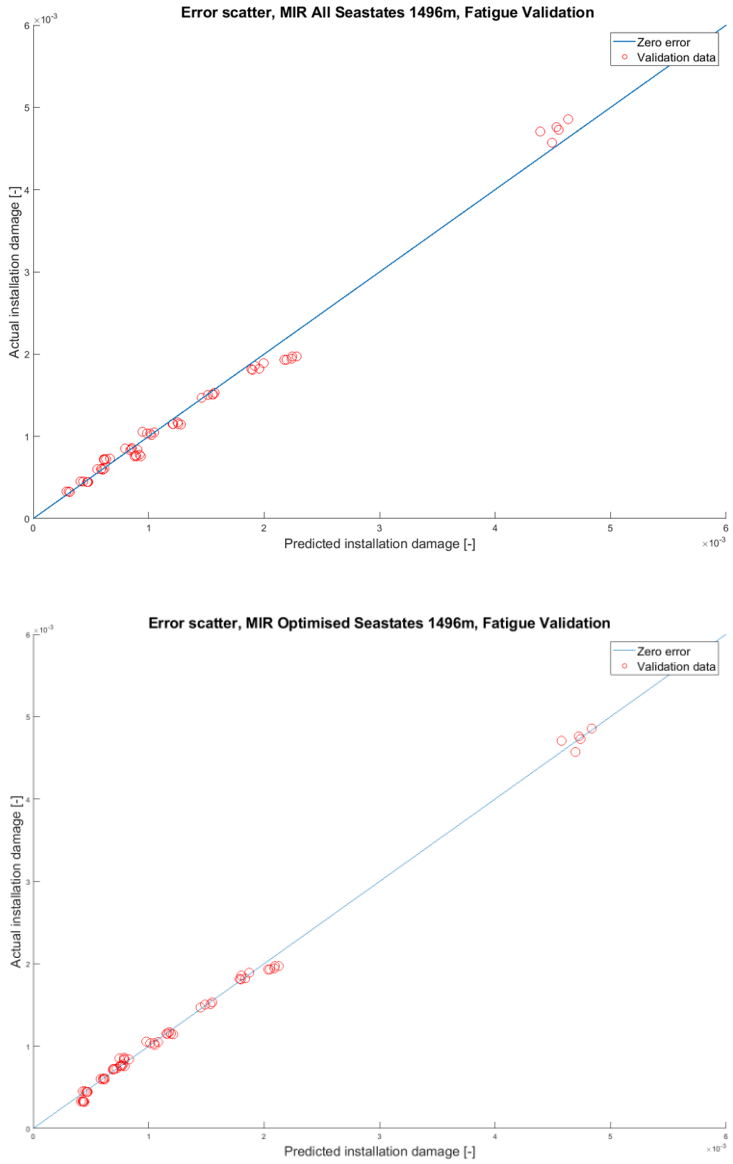

Figure 5-7 Validation data applied to fatigue prediction curves resulting from all and reduced sea states, deep water

General parameters		**Deep water Fatigue All sea states**				**Deep water Fatigue Optimised sea states**			
Water Depth	[m]	1496							
Pipeline section	[-]	B							
Regression parameters									
Input Variables		Surge acceleration X_3, Sway acceleration X_6, Heave acceleration X_9							
Error type		**Data points**	**Mean error [%]**	**Maximum error [%]**	**Minimum error [%]**	**Data points**	**Mean error [%]**	**Maximum error [%]**	**Minimum error [%]**
Total		75	7.3508	15.1933	-23.2638	75	5.5032	12.0563	-35.7312

Table 5-7 Results validation fatigue predictions, deep water

In Table 5-4 – Table 5-7, the mean error is the mean of the absolute values of the error percentages of all data points. The maximum error is the error percentage with the highest positive error value and the minimum error is the error percentage with the highest negative error value.

It can be observed in Figure 5-4 and Figure 5-5 that the overall shape of the error scatters is very similar if prediction curves are used based on all sea state simulations or based the optimised sea states simulations. However, the lowest dataset (coloured blue) increases in size and the three other datasets decrease in size. This is due to the increase of the mean heave acceleration for the optimised sea state selection, which is used to divide the data into groups.

The optimised sea state selection removes the lower sea states. This means the regression will more accurately predict the higher buckling check values since the regression will include relative more data points with higher output values. This is visible in Table 5-4 and Table 5-5 as the highest error shift to lower datasets.

Figure 5-6 and Figure 5-7 illustrate the error scatters of the optimised sea state validation regarding the fatigue prediction. Like buckling check, the results using all sea states are very similar to the results using the optimised sea state selection. These observations support the optimised selection of sea state ranges.

5.2. Discussion

This section will discuss observations and conclusions made throughout the entire thesis study.

5.2.1. Influence of motions

During this thesis, a particular emphasis is placed on investigating the influence of the vessel motions on the pipeline integrity. Three parameters are analysed to assess the integrity of the pipeline. These are the Von Mises strain, the DNV buckling check and the accumulated installation fatigue damage. Observations made during the isolated vessel motion analysis in Section 2.6 and the results of the proposed prediction methods in Chapter 4 lead to the same conclusion. The vertical motion at the stinger tip is the most influential motion for all three aforementioned parameters and therefore for the pipeline integrity during installation procedures. Although this may be true for both deep and shallow water installation cases, both have their distinct differences.

5.2.2. Deep & shallow water

During deep water pipeline installations, the vertical motion at the stinger tip is by far the most influential motion. This is mainly due to the vertical orientation and departure angle of the suspended pipeline. The orientation of the suspended pipeline shifts to a more horizontal position and the departure angle decreases as the water depth decreases.

The stinger tip motion in the direction of the departure angle seems to have the most influence on the pipeline integrity. The motion that is perpendicular to the departure angle seems to have the least influence, relatively speaking. This has to do with the displacement of the suspended pipeline in the sagbend area. The displacement in the sagbend area of the pipeline is largest when the stinger tip motion is in the direction of the departure angle. This is due to the length and circular shape of the pipeline catenary.

Figure 5-8 and Figure 5-9 illustrate the effect the water depth and departure angle ($\theta_{departure}$) have on the relation between the vertical stinger tip motion (y) and the pipeline catenary length (L).

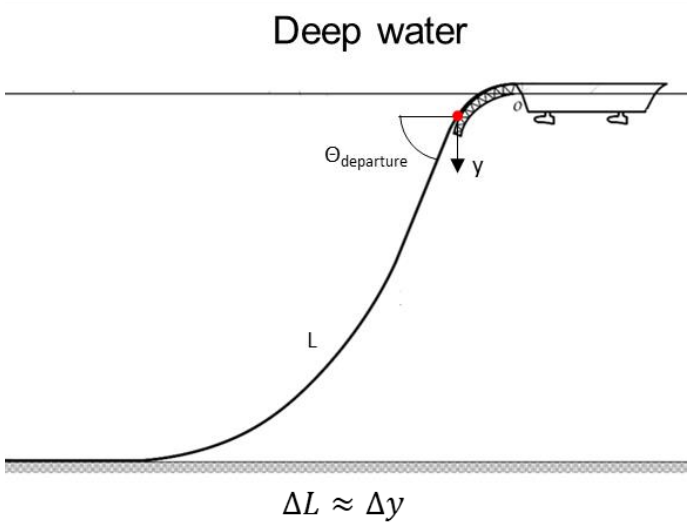

Figure 5-8 Catenary length as a result of vertical stinger tip motion, deep water

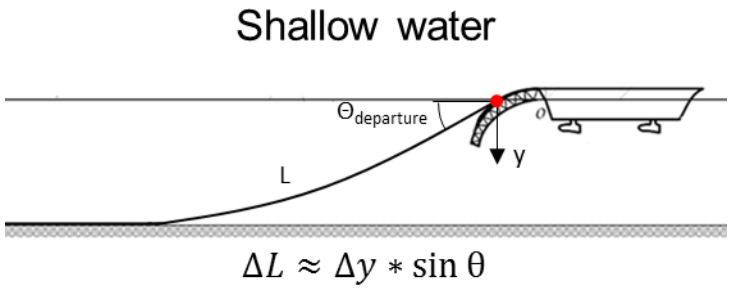

Figure 5-9 Catenary length as a result of vertical stinger tip motion, shallow water

As can be observed from the figures, the vertical stinger tip motion has less influence on the pipeline catenary length for a shallow water installation due to the smaller departure angle. In turn, the length of the catenary influences the weight of the pipeline and the required tension to maintain the stinger tip clearance. Therefore, the dynamic behaviour of the pipeline is influenced by the length of the pipeline catenary. So as the departure angle decreases, the difference in catenary length becomes less dependent on the vertical stinger tip motion

Hence, it can be concluded that as the water depth decreases, the relative influence of the vertical stinger tip motion decreases as well due to the departure angle and pipeline orientationThis shift in relative influence of the vessel motions is the main difference between shallow and deep water installation cases.

5.2.3. Motion components as input

The choice of using the acceleration and the velocity components as inputs for the strain and buckling check predictions is based on the isolated analysis of these components. If only one motion component is used as an input, the displacement component turned out to be the worst in terms of prediction error (Section 4.1.1). However, two components are used as an input for the strain and buckling check regression. This is determined to account for the rate of change of the vessel motions. Theoretically, there should be no difference in prediction if the combination of displacement and velocity or the combination of velocity and acceleration are chosen as input components.

The fatigue prediction curves are constructed with three similar motion components, namely, acceleration. It may seem odd that the acceleration component of the stinger tip motion correlates better to the fatigue damage then the other motion components. The inputs are measured as integrated motions per cycle and the velocity and acceleration components are time derivatives of the displacement component. The difference in prediction error could be explained with the relative position of the input/output data points to one another as can be observed in Figures 4-11(a-d). Using the acceleration component as an input results in a scatter cloud that fits best to a second order polynomial curve.

5.2.4. Polynomial curve

The drawback of using a second order polynomial curve with the MIR method, is the fact that the output may not converge to zero as the input decreases to zero. However, using an exponential function for a multiple input regression may be very impractical as is discussed in Section 4.2.1. It is difficult to visualise the data on which a multiple input regression should be performed as the number of inputs also indicates the number of dimension. The second order polynomial function may cause some slight errors at low in- and output values due to its quadratic shape. This can be alleviated by removing the lower sea states.These sea states are causing the low in- and output values, which in turn distort the entire prediction curve. The main interest of the thesis is to accurately predict higher output values which are crucial to the pipeline integrity. According to Box (1979), when discussing statistical regression models:

“All models are wrong, but some are useful.”

This is applicable to the second order polynomial curve; the properties of a second order polynomial curve may be wrong to describe the dynamic behaviour of a pipeline. Nonetheless, it has proven to be useful in terms of predicting the pipeline integrity.

5.2.5. Piecewise regression method

The piecewise regression method (MIPR) divides the in- and outputs into groups with more comparable behaviour. During this thesis, the decision is made to divide these groups according to the direction of motion as is described in Section 3.2. However, that does not mean that this division is the only method to group the data. Other data division methods may improve the accuracy of the prediction as well. The considered methods include the direction of the stinger tip motions and the velocity/displacement ratio of the stinger tip motions. The latter method has been considered due to the fact that a different amount of energy is transferred with different velocity/displacement ratios of the stinger tip motion. The ratio is solely dependent on the frequency of the stinger tip motion.

Figure 5-10 illustrates the strain peak distribution of the aforementioned ratios for deep and shallow water. The probability density function in Figure 5-11 clearly indicates a double peak distribution.

This shape of the scatter figure indicates that different ratio's correspond to different strain peaks. This means the behaviour of the pipeline is different for different ratios as well. The piecewise regression presented in Section 3.2 divides the corresponding in- and output by the direction of motion. This division yielded better results in terms of predicting the pipeline integrity.

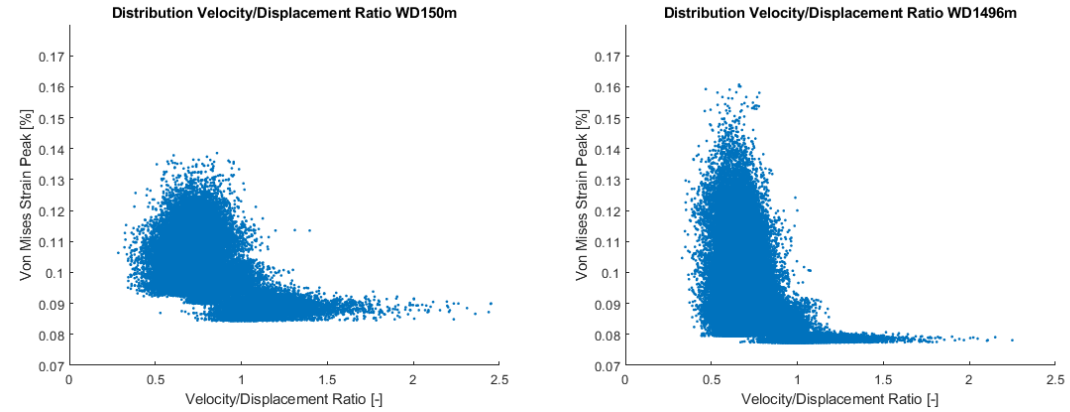

Figure 5-10 Velocity/displacement distribution of strain peaks in shallow and deep water

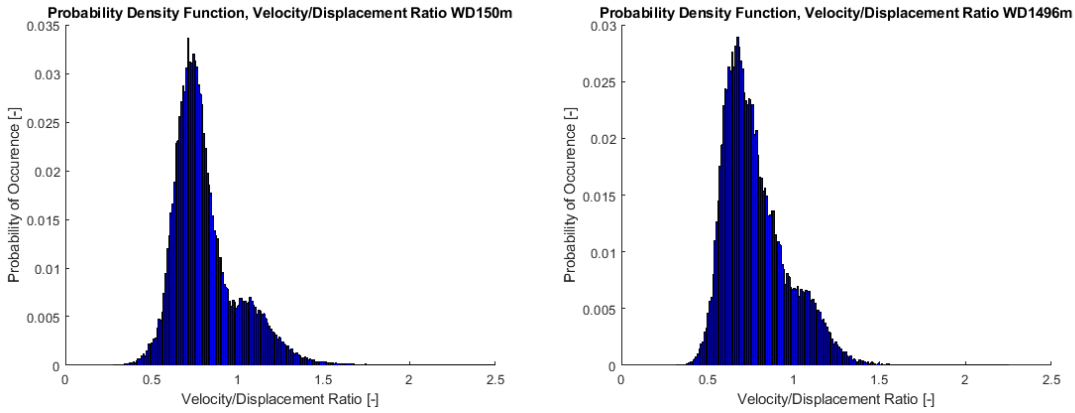

Figure 5-11 PDF velocity/acceleration ratios in shallow and deep water

5.2.6. Prediction confidence

During the simulations, the pipeline integrity is observed in the sagbend area of the pipeline. This region is assumed to be the most critical for the pipeline integrity due to the influence of vessel motions. A polynomial regression is implemented to acquire a 'best fit' prediction curve. It is needed to construct an upper bound or a safety factor to ensure the pipeline integrity predictions are not underestimated.

An upper bound can be constructed with any confidence level. This confidence level specifies the percentage of certainty that the actual output value (strain, code check or fatigue) has the same or smaller value than the predicted output value. The interval width between the upper bound and the zero error line is determined with Equation 5.1.

$$C = t^{-1} * \sigma_{error} \quad (5.1)$$

Where:

C	is interval width between the best fit and upper bound curve
t^{-1}	is the inverse of the t distribution, see Table 5.8
σ_{error}	is standard deviation of the error scatter, see Equation 5.2

The inverse t distribution is given in Table for a range of confidence levels. These are the values for a single tail distribution. A single tail distribution is needed as only the upper bound is required.

	Confidence level = 1-α					
α	0.005	0.01	0.025	0.05	0.1	0.25
t^{-1}	2.575	2.327	1.960	1.645	1.282	0.675

Table 5-8 inverse t distribution values for a range of confidence levels

The standard deviation of the error scatter is determined with the following equation:

$$\sigma_{error} = \sqrt{\frac{\sum_{i=1}^{n}(y_{predict} - y_{actual})^2}{n-1}} \quad (5.2)$$

Where:

σ_{error}	is standard deviation of the error scatter
$y_{predict}$	is the predicted output value that results from the prediction curves
y_{actual}	is the actual output value that results Orcaflex simulations
n	is the number of data points

The interval width value (C) is added to the predicted output value to ensure that the predicted output value has a certain confidence level that it has the same value as the actual output, or lower. This upper bound interval has to be determined for each sub-data set. An example is shown in Figure 5-12 and Table 5-9 for the shallow water code check prediction with a confidence of 99%.

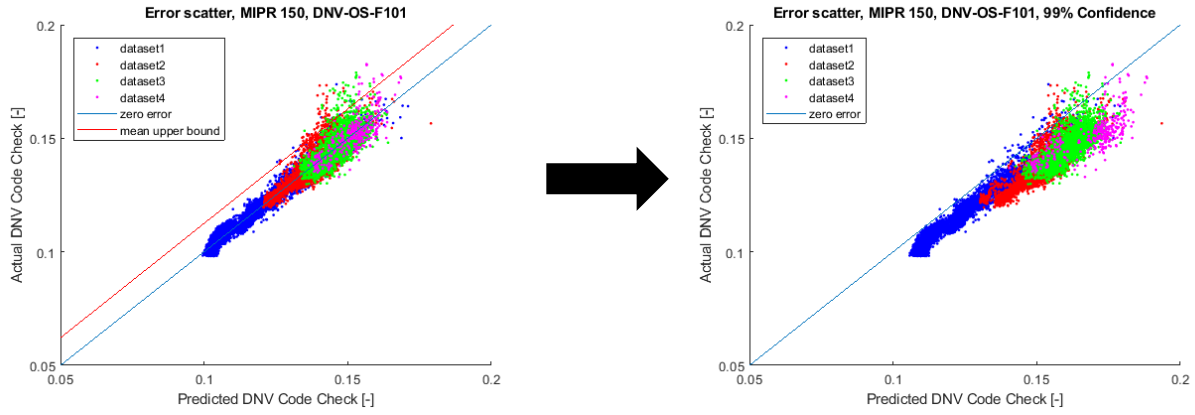

Figure 5-12 Error scatter confidence level implemented, shallow water

	Sub-dataset 1	Sub-dataset 2	Sub-dataset 3	Sub-dataset 4	Sub-dataset 5	Sub-dataset 6	Sub-dataset 7	Sub-dataset 8
C [%]	0.008	0.0062	0.0146	0.0084	0.0152	0.0114	0.0198	0.0100

Table 5-9 Upper bound width for every dataset, shallow water

5.3. Validation regression methods

The method to assess pipeline integrity which is presented in this thesis is developed based on parameters of the ROTA3 project. To evaluate the applicability of the proposed method, the method is applied to pipeline installation parameters of the Nordstream II project. At the time of writing, the Nordstream II project is an ongoing pipeline project that will connect Russia to Germany. The planned route of the pipeline is depicted in Figure 5-13. The Nordstream II pipelay parameters are completely different from the ROTA3 parameters. Therefore, the construced regressions methods are validated by applying them to this project.

A pipelay model has been constructed in Orcaflex with a water depth of 90 meters and using the PSA pipeline properties. The parameters of this pipeline are given in Table 5-9. Uni-directional JONSWAP sea states are used to excite the vessel motions and the parameters of these sea states are based on the relevant sea state analysis presented in Section 5.1:

- H_s: 2.5 and 3.0 meters
- T_z: 6,…10 seconds
- θ: 0,10,20,…180 degrees

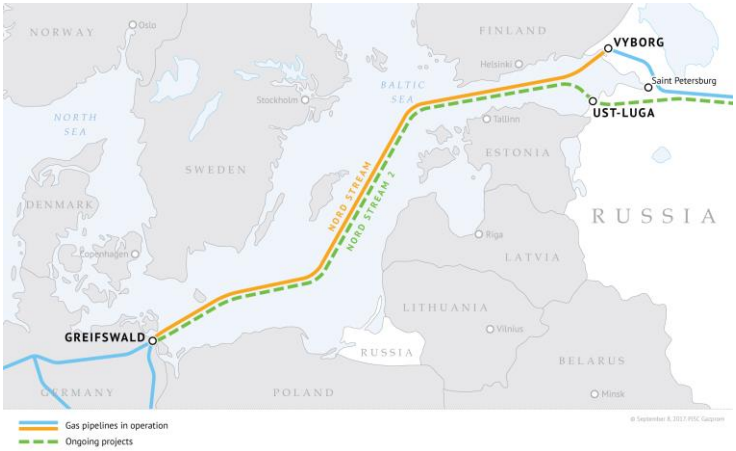

Figure 5-13 Nordstream II pipeline route

Section			PSA
Water depth	Minimum	[m]	25
	Maximum	[m]	91
Outside steel diameter		[mm]	1222.2
Overall outside diameter		[mm]	1390.6
Wall thickness		[mm]	34.6
Internal diameter		[mm]	1153
SMYS		[N/mm2]	485
SMTS		[N/mm2]	570
Anti-corrosion coating	Type	[-]	3LPE
	Thickness	[mm]	4.2
	Density	[kg/m3]	930
	Cutback	[m]	0.240
Concrete coating	Type	[-]	Cement
	Thickness	[mm]	80
	Density	[kg/m3]	3040
	Cutback	[m]	0.385
Dry weight	Empty	[N/m]	19784.7
	Flooded	[N/m]	30283.6
Submerged weight	Empty	[N/m]	4513
	Flooded	[N/m]	15011.9

Table 5-9 PSA pipeline properties

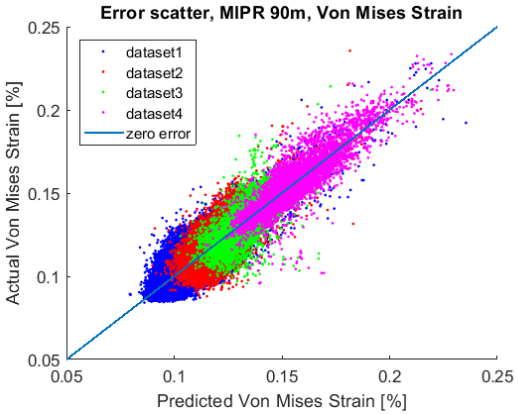

Figure 5-14 Error scatter strain, PSA pipeline

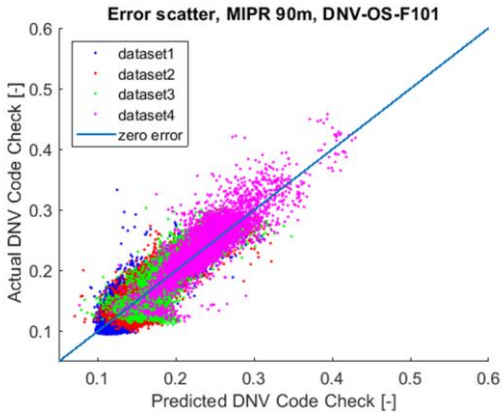

Figure 5-15 Error scatter DNV code check, PSA pipeline

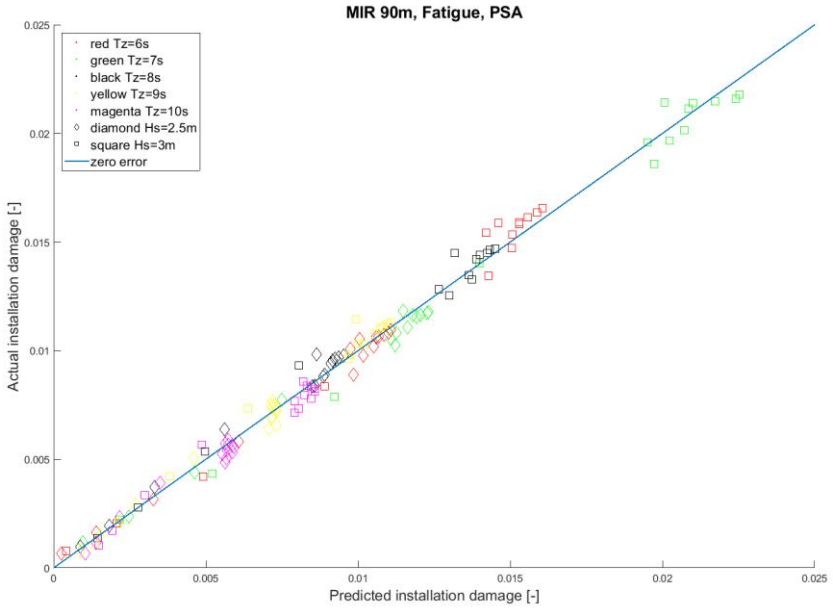

Figure 5-16 Error scatter fatigue, PSA pipeline

General parameters		**Von Mises Strain**	**DNV Code Check**	**Fatigue**
Water Depth	[m]	90		
Pipeline section	[-]	PSA		
Static case parameters				
Top Tension	[kN]	4900		
Von Mises Strain	[%]	0.08308		
Regression parameters				
Method		MIPR		MIR
Input Variables		Surge velocity X_2, Surge acceleration X_3 Heave velocity X_8 Heave acceleration X_9		Surge acceleration X_3 Sway acceleration X_6 Heave acceleration X_9
Measurement		Extreme motion		Integrated motion per cycle
μ heave acceleration	[m/s^2]	0.3355	0.3289	-
σ heave acceleration	[m/s^2]	0.2642	0.2625	-
RMSE	[-]	0.0076	0.0169	5.148*10^{-4}

Table 5-10 Error scatter strain, code check and fatigue results

Figure 5-14 and Figure 5-15 depict the error scatters of the Von Mises strain and DNV code check prediction curves constructed with the MIPR method. Figure 5-16 illustrates the error scatter of the fatigue installation damage. Table 5-10 shows the results of the regressions performed to acquire the aforementioned error scatters. The error scatters look similar to the results presented in Chapter 4 where the method was applied to simulation models based on the ROTA3 project. The Nordstream II pipeline is a very different project in terms of pipelay parameters. The PSA pipe properties have a much higher stiffness than the pipe A and B properties. The water depth at which the pipe is installed is also shallower.

The error scatter of the strain prediction shows a larger error than the ROTA3 strain predictions do. This is visible as the data points are more widely spread along the zero error line. This is probably due to the fact that if the departure angle becomes smaller (which is the case with decreasing water depths), the relative influence of the vertical stinger tip motion decreases. In turn, the relative influence of the horizontal stinger tip motions will increase. The sway motion is not used as an input for the strain and buckling check prediction, which may be a reason for the larger errors.

The overall shape of the clouds of points of the buckling check error scatter in Figure 5-10 is very similar to the ROTA3 error scatters as well. However, the range of the buckling check values is much larger for the Nordstream II project.

The increased diameter and wall thickness of the PSA pipeline also increases the plastic capacities of the pipeline and decreases the buckling check value. The increased weight of the pipeline also increases the loads acting on the pipeline during installation. The increased weight combined with the increased external pressure acting on the pipeline will in turn increase the buckling check value. This explains the higher buckling check values for the Nordstream II pipeline.

The same observations can be made for the fatigue error scatter as the strain and buckling check error scatters. The overall shape is very similar but the range is larger than for the ROTA3 error scatters. The higher range of the installation damages is due to the fact that the submerged weight value of the PSA pipeline is approximately eight times as large as the ROTA3 pipe. This results in higher stress ranges throughout the pipeline catenary which results in a larger fatigue damage.

These results show that the regression methods which are used to construct prediction curves to assess the pipeline integrity, produce similar results for projects with very different pipelay parameters. This means that the methods are applicable to other projects than the ROTA3 project, which is used to develop the methods.

6. CONCLUSION & RECOMMENDATIONS

6.1. Conclusion

The main focus of the thesis is twofold: firstly, to develop a method that will define a vessel motion based criteria for pipeline *Abandonment & Recovery* operations. Secondly, to investigate the influence of vessel motions on the dynamic pipeline behaviour and pipeline integrity. The two objectives are intertwined with one another as the understanding of the influence of vessel motions helps the method determination. The results that these methods provide, in turn, help developing the understanding of the influence of vessel motions. The first objective is accomplished with two methods that were developed during this thesis, namely:

- Multiple input polynomial regression method
- Multiple input, piecewise, polynomial regression method

These methods require the generation of multiple pipeline installation models during project preparation. Subsequently, the pipeline installation models are used to generate data which in turn is utilized to create ´prediction´ curves to quickly assess the pipeline integrity.

The second objective is accomplished with the help of the isolated vessel motion analysis and by analysing the results which are generated by the aforementioned developed regression methods. This resulted in the determination that stinger tip motion in the vertical direction is the most influential motion with regard to the pipeline integrity for all considered installation cases. However, stinger tip motions in all directions are relevant when fatigue damage is being assessed.

The relative influence of the vertical stinger tip motions decreases if the pipeline departure angle becomes smaller. The pipeline departure angle influences the length, weight and displacement of the suspended pipeline, which in turn determine the pipeline behaviour.

The number of sea-state simulations that is required for these regression methods, is optimised to decrease the required amount of simulation time. Lastly, the regression methods are validated with applicability analysis with Nordstream II pipelay parameters. This validation yielded similar results as for the ROTA3 project which means the method is validated and applicable to different projects.

6.2. Recommendations

The recommendations discussed in this section, are aimed at future development of the research presented in this thesis.

6.2.1. Workability

The methods in this thesis have been developed to ultimately improve the workability during offshore pipelay projects. However, the workability of these developed methods have not been assessed. Originally, it was planned that the workability would be assessed by applying the developed methods to recorded vessel motions of the Solitaire vessel. Whenever an abandonment decision had been made during the ROTA3 project, the vessel would change its heading to the most favourable position. Therefore, the vessel motions during abandonment are not representable for vessel motions that would occur during extreme weather. An abandonment criteria based on vessel motions would theoretically have a better workability than an abandonment criteria based on a worst case uni-directional sea state. It is advisable for future research to analyse and quantify the workability for the developed methods for a better comparison with the current methods.

6.2.2. Result analysis

The RMSE of the resulting error scatter presented in Chapter 4 are the RMSEs of the entire group of corresponding in- and outputs. For future research, it is advisable to analyse the RMSE of the different sub-groups of in- and outputs as well. This may give more insight to the change in error of specific sub-groups and may lead to different conclusions than the analyses of RMSEs of the entire scatter clouds do.

6.2.3. Variation limit of pipelay parameters

Pipeline behaviour is very sensitive to pipelay parameters such as water depth, set tension, departure angle etc. This means that a lot of different statistical models should be constructed during project preparation. However, no analysis has been done to quantify the required amount of different models. It is advisable to test to what extent a parameter may change before a new model is required to assess pipeline integrity. For future implementation, the required amount of statistical models should be quantified as well.

REFERENCES

Palmer, A.C. & King, R.A. (2008). *Subsea Pipeline Engineering* (2nd ed.). Tulsa: Penwell.

Allseas, (n.d.). *Allseas Introduction File* (rev. 4).

Holthuijsen, L.H. (2007). *Waves in oceanic and coastal waters*. Cambridge: Cambridge University Press.

Journee, J.M.J. & Massie, W.W. (2008). *Offshore Hydromechanics* (2nd ed.). Delft: TU Delft.

Det Norske Veritas AS (2013). *DNV Submarine Pipeline Systems*.

Det Norske Veritas AS (2013). *DNV Fatigue Design of Offshore Steel Structures*.

Schijve, J. (2009). *Fatigue of Structures and Materials* (2nd ed.). Delft: Springer.

Dekking, F.M. (2005). *A Modern Introduction to Probability and Statistics*. London: Springer.

Ryan, T.P. (2009). *Modern Regression Methods.* New Jersey: John Wiley & Sons.

Miller, A. (2002). *Subset Selection in Regression.* Florida: Chapman & Hall/CRC.

Kaufmann, B. (2003). *Fitting a Sum of Exponentials to Numerical Data.* Linz: Metallurgical research department.

Acton, F.S. (1990). *Numerical Methods that Work.* Washington: Harper & Row.

Box, G.E.P. (1979). *Robustness in the strategy of scientific model building*. New York: Academic Press.

Simanjuntak, T.A (2017). *Significance of active tension compensation during S-lay pipeline Installation (thesis)*. Delft: TU Delft.

Sri Paravastu, R. (2016). *Vessel motion based criteria for pipeline A&R operations (thesis)*. Delft: TU Delft

Orcina (n.d.), *Orcaflex manual*. Online at https://www.orcina.com/SoftwareProducts/Orcaflex/Documentation/Help/

APPENDIX A

ROTA3 recorded vessel motions

The recorded vessel motions that are used are those of the ROTA 3 project. The vessel Solitaire was performing the pipe lay operations that started on the 18th of October 2016 up until the 31st of May 2017. The entire project has a span of 232 days. The vessel Solitaire has multiple sensors that amongst other things recorded the vessel motions during the entire project.

The selection of data is of paramount importance. The sensors on the vessel Solitaire sample, on average, the vessel motion displacement 5 times a second. That adds up to half a million data points per day and more than a billion data points per sensor for the entire project. This will take an immense amount of unnecessary computing time, because a lot of the data will be similar to each other as the pipelay conditions will be very similar.

The selected data needs to be efficient to compute, but still capture the whole picture. That means that the data must be selected in such a way that the all probable sea states are included in the resulting vessel motions.

Three groups of approximately six consecutive days are chosen in which the vessel motions are collected that represent the vessel motions during operational weather. These consecutive days have been chosen because they included a variation of Hs, Tz and θ, such that all sea states within the range of these parameters are represented. All the groups are from a different time period within the ROTA 3 project to prevent all data originating the small period of time in which pipelay conditions may vary marginally. These groups of consecutive days add up to a total of 18 days. The sea state parameters of the groups of data are listed in Table A-1. These parameters are extracted from Solitaire daily weather reports. An example of the Hs range is shown in Figure A-1.

Date	Hs [m]	Tz [s]	Θ_{wave} [deg]	Range depth [m]
24/11/2016 – 30/11/2016	0.5 – 3.4	4.2 – 8.6	70 – 340	130 – 260
05/12/2016 – 09/12/2016	0.3 – 2.0	4.4 – 8.5	70 – 345	340 – 606
24/03/2017 – 29/03/2017	1.5 – 2.1	5.5 – 7.3	120 – 195	2065 – 2255

Table A-0-1 Sea state parameters recorded data ROTA3

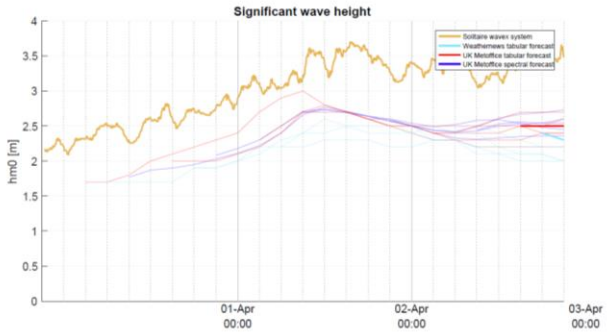

Figure A-0-1 Example of measured and predicted significant wave height

APPENDIX B

Delay distributions

The delay distributions between the strain peak and the motion peaks are presented in Section 4.1.1 are depicted in Figure B a-p.

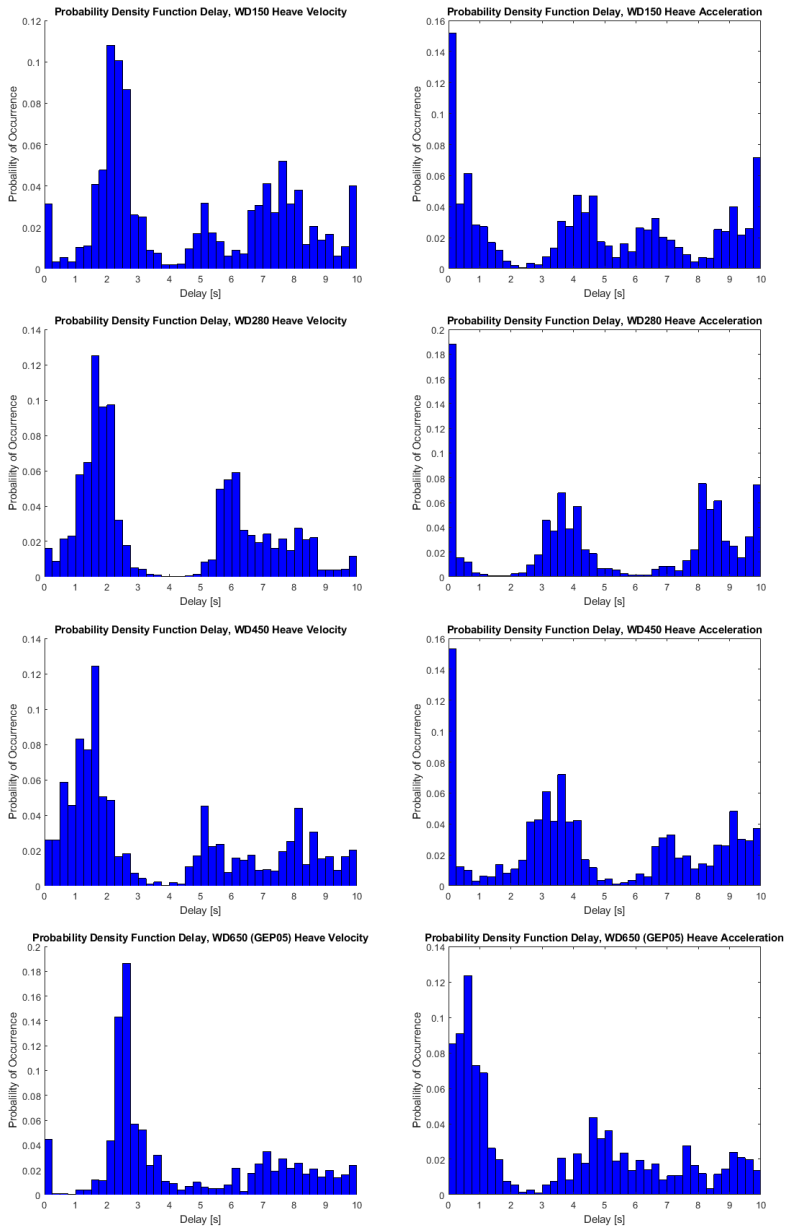

Figure B a-h delay distributions between strain peak and motion peak

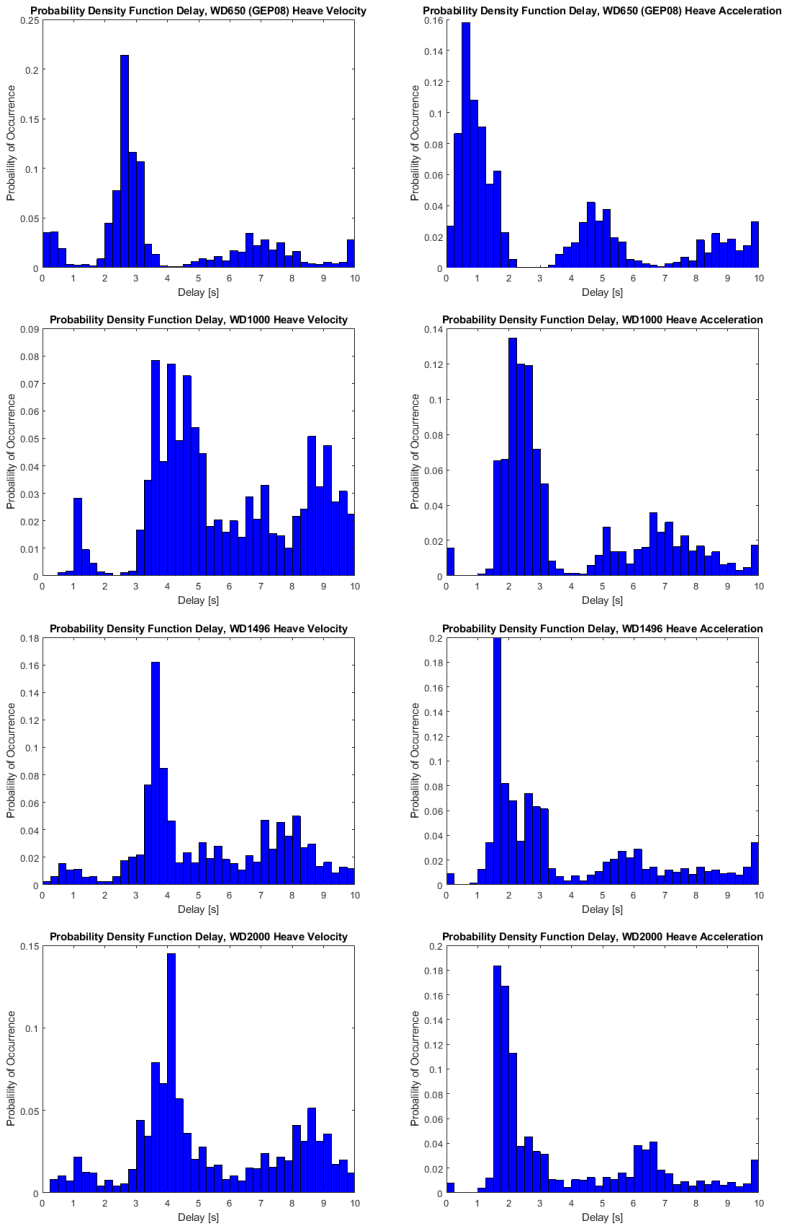

Figure B i-p delay distributions between strain peak and motion peak

APPENDIX C

Strain prediction curve coefficients

Case 1; 150m

The formulas for the 8 different datasets for case 1 have the general form listed in Equation C.1. The coefficients are listed in Table C-1 and the standard deviation coefficients are listed in Table C-2. Lastly, the RMSE for all different datasets are given in Table C-3.

$$Y_{predict} = C_1{X_2}^2 + C_2{X_3}^2 + C_3{X_8}^2 + C_4{X_9}^2 + C_5X_2X_3 + C_6X_2X_8 + C_7X_2X_9 + C_8X_3X_8 + C_9X_3X_9 + C_{10}X_8X_9 + C_{11}X_2 + C_{12}X_3 + C_{13}X_8 + C_{14}X_9 + C_{15} \quad \text{(C.1)}$$

Case 1 coefficients		C_1	C_2	C_3	C_4	C_5	C_6	C_7	C_8	C_9	C_{10}	C_{11}	C_{12}	C_{13}	C_{14}	C_{15}
Dataset 1	Sub-dataset 1	0.998	3.318	0.070	0.064	3.544	0.222	0.067	0.193	0.116	0.131	0.195	0.185	0.012	0.035	0.087
	Sub-dataset 2	2.361	8.345	0.070	0.172	8.663	-0.136	-0.031	0.041	0.174	0.323	0.153	0.170	-0.021	-0.057	0.086
Dataset 2	Sub-dataset 1	0.139	0.659	0.139	0.051	0.576	-0.014	-0.075	-0.026	-0.083	0.081	0.052	0.048	-0.023	0.022	0.077
	Sub-dataset 2	0.014	0.174	0.023	0.048	-0.074	-0.059	-0.019	-0.004	0.083	0.058	0.050	0.076	0.053	-0.024	0.063
Dataset 3	Sub-dataset 1	-0.058	0.215	-0.014	-0.016	-0.113	0.059	-0.008	0.104	0.034	-0.023	0.076	0.096	-0.023	0.009	0.085
	Sub-dataset 2	0.572	1.319	-0.016	0.133	1.636	0.330	0.705	0.374	0.763	0.284	0.334	0.333	-0.029	-0.115	0.062
Dataset 4	Sub-dataset 1	-0.142	-0.348	0.122	0.003	-0.500	0.011	0.011	0.069	0.099	-0.057	-0.054	-0.075	-0.054	-0.133	0.161
	Sub-dataset 2	-3.125	-5.152	-0.032	-0.273	-8.150	0.022	-0.224	-0.227	-0.630	-0.085	-0.509	-0.662	-0.236	-0.670	-0.177

Table C-1 Prediction curve coefficients

Case 1 standard dev		C_1	C_2	C_3	C_4	C_5	C_6	C_7	C_8	C_9	C_{10}	C_{11}	C_{12}	C_{13}	C_{14}	C_{15}
Dataset 1	Sub-dataset 1	0.998	3.318	0.070	0.064	3.544	0.222	0.067	0.193	0.116	0.131	0.195	0.185	0.012	0.035	0.087
	Sub-dataset 2	0.267	0.618	0.012	0.020	0.801	0.094	0.121	0.141	0.178	0.030	0.010	0.012	0.003	0.003	0.000
Dataset 2	Sub-dataset 1	0.052	0.118	0.002	0.007	0.156	0.015	0.025	0.022	0.037	0.007	0.013	0.020	0.003	0.007	0.002
	Sub-dataset 2	0.157	0.308	0.014	0.023	0.447	0.075	0.099	0.095	0.129	0.030	0.060	0.086	0.013	0.028	0.010
Dataset 3	Sub-dataset 1	0.057	0.124	0.002	0.008	0.167	0.012	0.024	0.017	0.034	0.006	0.021	0.030	0.004	0.013	0.007
	Sub-dataset 2	0.218	0.376	0.018	0.042	0.571	0.116	0.142	0.140	0.178	0.048	0.103	0.113	0.028	0.051	0.022
Dataset 4	Sub-dataset 1	0.265	0.532	0.007	0.032	0.744	0.043	0.106	0.058	0.137	0.023	0.148	0.187	0.021	0.062	0.040
	Sub-dataset 2	0.693	1.043	0.071	0.324	1.691	0.355	0.788	0.403	0.899	0.294	0.571	0.657	0.192	0.445	0.163

Table C-2 Prediction curve standard deviation coefficients

Case 1		$RMSE$
Dataset 1	Sub-dataset 1	0.001202
	Sub-dataset 2	0.002100
Dataset 2	Sub-dataset 1	0.002077
	Sub-dataset 2	0.002251
Dataset 3	Sub-dataset 1	0.002367
	Sub-dataset 2	0.002994
Dataset 4	Sub-dataset 1	0.002264
	Sub-dataset 2	0.001202

Table C-3 RMSE for separate datasets

Case 2; 280m

The formulas for the 8 different datasets for case 2 have the general form listed in Equation C.2. The coefficients are listed in Table C-4 and the standard deviation coefficients are listed in Table C-5. Lastly, the RMSE for all different datasets are given in Table C-6.

$$Y_{predict} = C_1 {X_2}^2 + C_2 {X_3}^2 + C_3 {X_8}^2 + C_4 {X_9}^2 + C_5 X_2 X_3 + C_6 X_2 X_8 + C_7 X_2 X_9 + C_8 X_3 X_8 + C_9 X_3 X_9 + C_{10} X_8 X_9 + C_{11} X_2 + C_{12} X_3 + C_{13} X_8 + C_{14} X_9 + C_{15} \quad \text{(C.2)}$$

Case 2 coefficients		C_1	C_2	C_3	C_4	C_5	C_6	C_7	C_8	C_9	C_{10}	C_{11}	C_{12}	C_{13}	C_{14}	C_{15}
Dataset 1	Sub-dataset 1	-0.025	0.592	0.027	0.068	0.141	0.019	0.114	-0.031	0.062	0.094	-0.045	-0.040	-0.029	-0.015	0.079
	Sub-dataset 2	0.108	0.317	0.003	0.005	0.371	0.018	0.027	0.031	0.046	0.007	0.005	0.008	0.001	0.001	0.000
Dataset 2	Sub-dataset 1	0.038	0.077	0.001	0.004	0.107	0.012	0.020	0.016	0.027	0.004	0.012	0.017	0.002	0.005	0.002
	Sub-dataset 2	0.141	0.270	0.007	0.009	0.400	0.040	0.039	0.052	0.052	0.015	0.038	0.049	0.006	0.010	0.005
Dataset 3	Sub-dataset 1	0.037	0.069	0.001	0.005	0.101	0.010	0.019	0.014	0.025	0.004	0.020	0.027	0.003	0.011	0.007
	Sub-dataset 2	0.288	0.511	0.019	0.056	0.733	0.106	0.191	0.112	0.198	0.060	0.139	0.152	0.031	0.070	0.030
Dataset 4	Sub-dataset 1	0.085	0.156	0.003	0.011	0.229	0.020	0.044	0.027	0.057	0.009	0.056	0.071	0.010	0.023	0.015
	Sub-dataset 2	0.428	0.699	0.015	0.051	0.561	0.075	0.123	0.137	0.200	0.052	0.165	0.220	0.034	0.068	0.019

Table C-4 Prediction curve coefficients

Case 2 standard dev		C_1	C_2	C_3	C_4	C_5	C_6	C_7	C_8	C_9	C_{10}	C_{11}	C_{12}	C_{13}	C_{14}	C_{15}
Dataset 1	Sub-dataset 1	-0.025	0.592	0.027	0.068	0.141	0.019	0.114	-0.031	0.062	0.094	-0.045	-0.040	-0.029	-0.015	0.079
	Sub-dataset 2	0.702	3.276	-0.014	0.029	2.763	0.085	0.095	0.058	0.075	0.021	-0.032	-0.024	0.028	0.005	0.078
Dataset 2	Sub-dataset 1	0.123	0.669	0.005	0.049	0.556	0.004	-0.016	0.021	0.009	0.053	0.023	0.029	-0.045	-0.026	0.075
	Sub-dataset 2	1.147	2.415	0.026	0.038	3.403	-0.132	0.100	-0.132	0.151	0.068	0.222	0.264	0.002	-0.022	0.079
Dataset 3	Sub-dataset 1	0.189	0.598	0.007	-0.004	0.662	0.033	-0.025	0.056	-0.019	0.009	0.081	0.115	0.011	0.035	0.081
	Sub-dataset 2	1.093	1.878	-0.022	0.069	2.832	-0.012	0.446	0.099	0.667	0.005	0.538	0.639	0.041	0.118	0.136
Dataset 4	Sub-dataset 1	-0.006	0.167	-0.018	-0.014	0.067	0.029	0.058	0.049	0.093	-0.022	-0.069	-0.087	-0.052	0.004	0.035
	Sub-dataset 2	-0.144	12.38	0.007	0.759	10.27	-1.095	-0.734	-0.827	0.407	0.440	-0.689	0.266	0.603	1.298	0.412

Table C-5 Prediction curve standard deviation coefficients

Case 2		$RMSE$
Dataset 1	Sub-dataset 1	0.00204
	Sub-dataset 2	0.00129
Dataset 2	Sub-dataset 1	0.00200
	Sub-dataset 2	0.00107
Dataset 3	Sub-dataset 1	0.00240
	Sub-dataset 2	0.00109
Dataset 4	Sub-dataset 1	0.00268
	Sub-dataset 2	0.00004

Table C-6 RMSE for separate datasets

Case 3; 450m

The formulas for the 8 different datasets for case 3 have the general form listed in Equation C.3. The coefficients are listed in Table C-7 and the standard deviation coefficients are listed in Table C-8. Lastly, the RMSE for all different datasets are given in Table C-9.

$$Y_{predict} = C_1 {X_8}^2 + C_2 {X_9}^2 + C_3 X_8 X_9 + C_4 X_8 + C_5 X_9 + C_6 \quad \text{(C.3)}$$

Case 3 coefficients		C_1	C_2	C_3	C_4	C_5	C_6
Dataset 1	Sub-dataset 1	0.023	0.022	0.051	-0.014	0.006	0.082
	Sub-dataset 2	-0.007	-0.053	-0.040	-0.004	-0.033	0.081
Dataset 2	Sub-dataset 1	0.003	0.021	0.037	-0.047	0.001	0.065
	Sub-dataset 2	-0.022	-0.097	-0.092	-0.016	-0.068	0.068
Dataset 3	Sub-dataset 1	0.002	0.022	0.027	-0.038	-0.009	0.071
	Sub-dataset 2	-0.061	0.058	0.050	0.284	0.067	-0.098
Dataset 4	Sub-dataset 1	-0.002	0.020	0.012	-0.033	-0.034	0.101
	Sub-dataset 2	0.010	-0.046	-0.006	-0.071	-0.189	0.009

Table C-7 Prediction curve coefficients

Case 3 standard dev		C_1	C_2	C_3	C_4	C_5	C_6
Dataset 1	Sub-dataset 1	0.023	0.022	0.051	-0.014	0.006	0.082
	Sub-dataset 2	0.003	0.007	0.009	0.001	0.002	0.000
Dataset 2	Sub-dataset 1	0.001	0.003	0.003	0.001	0.004	0.002
	Sub-dataset 2	0.003	0.012	0.010	0.004	0.011	0.004
Dataset 3	Sub-dataset 1	0.001	0.006	0.004	0.004	0.013	0.008
	Sub-dataset 2	0.037	0.055	0.081	0.056	0.106	0.070
Dataset 4	Sub-dataset 1	0.003	0.009	0.008	0.007	0.016	0.009
	Sub-dataset 2	0.016	0.046	0.054	0.024	0.045	0.019

Table C-8 Prediction curve standard deviation coefficients

Case 3		$RMSE$
Dataset 1	Sub-dataset 1	0.00182
	Sub-dataset 2	0.00102
Dataset 2	Sub-dataset 1	0.00233
	Sub-dataset 2	0.00122
Dataset 3	Sub-dataset 1	0.00306
	Sub-dataset 2	0.00218
Dataset 4	Sub-dataset 1	0.00265
	Sub-dataset 2	0.00170

Table C-9 RMSE for separate datasets

Case 4; 650m (A)

The formulas for the 8 different datasets for case 4 have the general form listed in Equation C.4. The coefficients are listed in Table C-10 and the standard deviation coefficients are listed in Table C-11. Lastly, the RMSE for all different datasets are given in Table C-12.

$$Y_{predict} = C_1 {X_8}^2 + C_2 {X_9}^2 + C_3 X_8 X_9 + C_4 X_8 + C_5 X_9 + C_6 \quad \text{(C.4)}$$

Case 4 coefficients		C_1	C_2	C_3	C_4	C_5	C_6
Dataset 1	Sub-dataset 1	0.025	0.023	0.044	0.008	0.024	0.064
	Sub-dataset 2	-0.106	-0.150	-0.249	-0.014	-0.037	0.063
Dataset 2	Sub-dataset 1	0.003	0.025	0.021	-0.016	-0.001	0.063
	Sub-dataset 2	-0.003	-0.231	-0.181	-0.138	-0.222	0.045
Dataset 3	Sub-dataset 1	0.001	0.015	0.018	-0.019	0.021	0.044
	Sub-dataset 2	0.037	0.196	0.190	0.140	0.185	0.080
Dataset 4	Sub-dataset 1	-0.015	-0.007	-0.022	-0.035	-0.014	0.061
	Sub-dataset 2	-0.005	-0.013	-0.022	-0.013	-0.015	0.090

Table C-10 Prediction curve coefficients

Case 4 standard dev		C_1	C_2	C_3	C_4	C_5	C_6
Dataset 1	Sub-dataset 1	0.025	0.023	0.044	0.008	0.024	0.064
	Sub-dataset 2	0.019	0.027	0.045	0.002	0.002	0.000
Dataset 2	Sub-dataset 1	0.001	0.003	0.003	0.001	0.004	0.002
	Sub-dataset 2	0.300	0.461	0.626	0.307	0.390	0.148
Dataset 3	Sub-dataset 1	0.001	0.005	0.004	0.003	0.012	0.008
	Sub-dataset 2	0.005	0.027	0.022	0.017	0.052	0.031
Dataset 4	Sub-dataset 1	0.005	0.018	0.018	0.019	0.039	0.033
	Sub-dataset 2	0.006	0.019	0.021	0.014	0.031	0.020

Table C-11 Prediction curve standard deviation coefficients

Case 4		$RMSE$
Dataset 1	Sub-dataset 1	0.00095
	Sub-dataset 2	0.00083
Dataset 2	Sub-dataset 1	0.00184
	Sub-dataset 2	0.00084
Dataset 3	Sub-dataset 1	0.00263
	Sub-dataset 2	0.00262
Dataset 4	Sub-dataset 1	0.00267
	Sub-dataset 2	0.00207

Table C-12 RMSE for separate datasets

Case 5; 650m (B)

The formulas for the 8 different datasets for case 5 have the general form listed in Equation C.5. The coefficients are listed in Table C-13 and the standard deviation coefficients are listed in Table C-14. Lastly the RMSE for all different datasets are given in Table C-15.

$$Y_{predict} = C_1 {X_8}^2 + C_2 {X_9}^2 + C_3 X_8 X_9 + C_4 X_8 + C_5 X_9 + C_6 \quad \text{(C.5)}$$

Case 5 coefficients		C_1	C_2	C_3	C_4	C_5	C_6
Dataset 1	Sub-dataset 1	0.013	-0.025	0.001	-0.008	0.028	0.076
	Sub-dataset 2	-0.055	-0.101	-0.138	0.022	-0.014	0.076
Dataset 2	Sub-dataset 1	0.018	-0.035	0.003	-0.003	0.063	0.059
	Sub-dataset 2	-0.043	-0.188	-0.181	-0.025	-0.120	0.051
Dataset 3	Sub-dataset 1	0.016	0.006	0.066	-0.084	0.081	-0.028
	Sub-dataset 2	-0.056	-0.073	-0.102	0.114	0.003	-0.003
Dataset 4	Sub-dataset 1	0.015	0.080	0.096	-0.134	-0.086	0.055
	Sub-dataset 2	-0.039	-0.039	-0.054	0.113	-0.007	-0.013

Table C-13 Prediction curve coefficients

Case 5 standard dev		C_1	C_2	C_3	C_4	C_5	C_6
Dataset 1	Sub-dataset 1	0.013	-0.025	0.001	-0.008	0.028	0.076
	Sub-dataset 2	0.002	0.004	0.005	0.001	0.002	0.000
Dataset 2	Sub-dataset 1	0.001	0.003	0.003	0.001	0.004	0.002
	Sub-dataset 2	0.004	0.017	0.015	0.005	0.017	0.006
Dataset 3	Sub-dataset 1	0.001	0.006	0.004	0.004	0.012	0.008
	Sub-dataset 2	0.004	0.020	0.015	0.012	0.039	0.024
Dataset 4	Sub-dataset 1	0.005	0.014	0.015	0.017	0.030	0.027
	Sub-dataset 2	0.007	0.023	0.023	0.025	0.050	0.040

Table C-14 Prediction curve standard deviation coefficients

Case 5		$RMSE$
Dataset 1	Sub-dataset 1	0.00119
	Sub-dataset 2	0.00112
Dataset 2	Sub-dataset 1	0.00162
	Sub-dataset 2	0.00367
Dataset 3	Sub-dataset 1	0.00245
	Sub-dataset 2	0.00466
Dataset 4	Sub-dataset 1	0.00334
	Sub-dataset 2	0.00319

Table C-15 RMSE for separate datasets

Case 6; 1000m

The formulas for the 8 different datasets for case 6 have the general form listed in Equation C.6. The coefficients are listed in Table C-16 and the standard deviation coefficients are listed in Table C-17. Lastly, the RMSE for all different datasets are given in Table C-18.

$$Y_{predict} = C_1 {X_8}^2 + C_2 {X_9}^2 + C_3 X_8 X_9 + C_4 X_8 + C_5 X_9 + C_6 \quad \text{(C.6)}$$

Case 6 coefficients		C_1	C_2	C_3	C_4	C_5	C_6
Dataset 1	Sub-dataset 1	0.001	-0.068	-0.066	0.012	0.029	0.068
	Sub-dataset 2	-0.042	-0.137	-0.169	-0.013	-0.034	0.067
Dataset 2	Sub-dataset 1	0.031	0.000	0.041	-0.001	0.057	0.046
	Sub-dataset 2	-0.045	-0.118	-0.145	0.010	-0.046	0.046
Dataset 3	Sub-dataset 1	0.008	0.012	0.054	-0.094	0.028	-0.005
	Sub-dataset 2	-0.031	-0.046	-0.055	0.077	-0.003	0.023
Dataset 4	Sub-dataset 1	0.000	0.082	0.054	-0.125	-0.196	0.149
	Sub-dataset 2	-0.041	-0.021	-0.078	0.091	0.140	0.127

Table C-16 Prediction curve coefficients

Case 6 standard dev		C_1	C_2	C_3	C_4	C_5	C_6
Dataset 1	Sub-dataset 1	0.001	-0.068	-0.066	0.012	0.029	0.068
	Sub-dataset 2	0.002	0.003	0.004	0.001	0.001	0.000
Dataset 2	Sub-dataset 1	0.001	0.003	0.002	0.001	0.004	0.002
	Sub-dataset 2	0.004	0.016	0.015	0.005	0.015	0.005
Dataset 3	Sub-dataset 1	0.001	0.005	0.003	0.003	0.010	0.006
	Sub-dataset 2	0.006	0.024	0.017	0.014	0.045	0.027
Dataset 4	Sub-dataset 1	0.003	0.009	0.010	0.010	0.014	0.010
	Sub-dataset 2	0.013	0.053	0.039	0.042	0.126	0.100

Table C-17 Prediction curve standard deviation coefficients

Case 6		$RMSE$
Dataset 1	Sub-dataset 1	0.00067
	Sub-dataset 2	0.00087
Dataset 2	Sub-dataset 1	0.00153
	Sub-dataset 2	0.00333
Dataset 3	Sub-dataset 1	0.00208
	Sub-dataset 2	0.00481
Dataset 4	Sub-dataset 1	0.00237
	Sub-dataset 2	0.00357

Table C-18 RMSE for separate datasets

Case 7; 1496m

The formulas for the 8 different datasets for case 7 have the general form listed in Equation C.7. The coefficients are listed in Table C-19 and the standard deviation coefficients are listed in Table C-20. Lastly the RMSE for all different datasets are given in Table C-21.

$$Y_{predict} = C_1 {X_8}^2 + C_2 {X_9}^2 + C_3 X_8 X_9 + C_4 X_8 + C_5 X_9 + C_6 \quad \text{(C.7)}$$

Case 7 coefficients		C_1	C_2	C_3	C_4	C_5	C_6
Dataset 1	Sub-dataset 1	0.050	0.067	0.105	0.013	0.023	0.077
	Sub-dataset 2	0.014	0.004	0.017	-0.011	-0.025	0.077
Dataset 2	Sub-dataset 1	0.044	0.007	0.066	0.014	0.076	0.049
	Sub-dataset 2	-0.012	-0.098	-0.122	-0.062	-0.043	0.094
Dataset 3	Sub-dataset 1	0.013	0.079	0.121	-0.143	-0.011	-0.016
	Sub-dataset 2	-0.029	0.031	0.021	0.159	0.048	-0.016
Dataset 4	Sub-dataset 1	-0.004	0.058	0.011	-0.055	-0.189	0.213
	Sub-dataset 2	-0.021	0.027	-0.036	0.045	0.177	0.207

Table C-19 Prediction curve coefficients

Case 7 standard dev		C_1	C_2	C_3	C_4	C_5	C_6
Dataset 1	Sub-dataset 1	0.050	0.067	0.105	0.013	0.023	0.077
	Sub-dataset 2	0.001	0.003	0.003	0.001	0.001	0.000
Dataset 2	Sub-dataset 1	0.001	0.004	0.003	0.001	0.005	0.002
	Sub-dataset 2	0.004	0.016	0.014	0.005	0.017	0.006
Dataset 3	Sub-dataset 1	0.001	0.006	0.004	0.003	0.013	0.008
	Sub-dataset 2	0.005	0.018	0.013	0.013	0.037	0.023
Dataset 4	Sub-dataset 1	0.004	0.008	0.009	0.010	0.015	0.009
	Sub-dataset 2	0.015	0.034	0.042	0.020	0.050	0.033

Table C-20 Prediction curve standard deviation coefficients

Case 7		$RMSE$
Dataset 1	Sub-dataset 1	0.000748
	Sub-dataset 2	0.000671
Dataset 2	Sub-dataset 1	0.001978
	Sub-dataset 2	0.003613
Dataset 3	Sub-dataset 1	0.002399
	Sub-dataset 2	0.003950
Dataset 4	Sub-dataset 1	0.002793
	Sub-dataset 2	0.002184

Table C-21 RMSE for separate datasets

Case 8; 2000m

The formulas for the 8 different datasets for case 8 have the general form listed in Equation C.8. The coefficients are listed in Table C-22 and the standard deviation coefficients are listed in Table C-23. Lastly the RMSE for all different datasets are given in Table C-24.

$$Y_{predict} = C_1 {X_8}^2 + C_2 {X_9}^2 + C_3 X_8 X_9 + C_4 X_8 + C_5 X_9 + C_6 \quad \text{(C.8)}$$

Case 8 coefficients		C_1	C_2	C_3	C_4	C_5	C_6
Dataset 1	Sub-dataset 1	0.025	0.021	0.034	0.016	0.023	0.095
	Sub-dataset 2	-0.012	-0.032	-0.054	-0.011	-0.016	0.095
Dataset 2	Sub-dataset 1	0.042	-0.022	0.087	0.012	0.170	0.025
	Sub-dataset 2	-0.021	-0.086	-0.100	-0.032	-0.046	0.098
Dataset 3	Sub-dataset 1	0.001	0.051	0.053	-0.085	-0.041	0.059
	Sub-dataset 2	-0.023	-0.070	-0.039	0.043	-0.130	-0.021
Dataset 4	Sub-dataset 1	0.003	-0.046	-0.024	0.043	0.133	0.031
	Sub-dataset 2	-0.049	-0.058	-0.142	-0.003	0.142	0.258

Table C-22 Prediction curve coefficients

Case 8 standard dev		C_1	C_2	C_3	C_4	C_5	C_6
Dataset 1	Sub-dataset 1	0.025	0.021	0.034	0.016	0.023	0.095
	Sub-dataset 2	0.001	0.002	0.003	0.001	0.001	0.000
Dataset 2	Sub-dataset 1	0.001	0.004	0.003	0.001	0.005	0.002
	Sub-dataset 2	0.002	0.008	0.007	0.003	0.009	0.003
Dataset 3	Sub-dataset 1	0.001	0.005	0.003	0.004	0.012	0.008
	Sub-dataset 2	0.003	0.015	0.011	0.009	0.032	0.020
Dataset 4	Sub-dataset 1	0.003	0.009	0.009	0.010	0.021	0.017
	Sub-dataset 2	0.024	0.080	0.086	0.049	0.098	0.047

Table C-23 Prediction curve standard deviation coefficients

Case 8		$RMSE$
Dataset 1	Sub-dataset 1	0.000807
	Sub-dataset 2	0.000757
Dataset 2	Sub-dataset 1	0.001969
	Sub-dataset 2	0.002132
Dataset 3	Sub-dataset 1	0.002220
	Sub-dataset 2	0.002965
Dataset 4	Sub-dataset 1	0.002760
	Sub-dataset 2	0.004897

Table C-24 RMSE for separate datasets